University of Ottawa

Masters Thesis

Exploring Optical Nonlinearity in III-V Semiconductors

Author:

Mfon Odungide

Supervisor:

Prof. Ksenia Dolgaleva

A thesis submitted in partial fulfillment of the requirements
for the degree of Masters of Applied Science

uOttawa

Faculté de génie
Faculty of Engineering

Ottawa-Carleton Institute for Electrical and Computer Engineering
University of Ottawa

Declaration of Authorship

I, Mfon ODUNGIDE, declare that this thesis, titled "Exploring Optical Nonlinearity in III-V Semiconductors", and the work presented in it are my own. I confirm that except where specific reference is made to the work of others, the contents of this dissertation are original and have not been submitted in whole or in part for consideration for any other degree or qualification in this, or any other university. This dissertation is my own work and contains nothing which is the outcome of work done in collaboration with others, except as specified in the text and Acknowledgements.

Mfon Odungide
November, 2019
Ottawa, Canada

UNIVERSITY OF OTTAWA

Abstract

School of Electrical Engineering and Computer Science

Ottawa-Carleton Institute for Electrical and Computer Engineering

Masters of Applied Science

Exploring Optical Nonlinearity in III-V Semiconductors

by Mfon ODUNGIDE

This Master's dissertation focuses on exploring optical nonlinearities in III-V semiconductors. This work covers a range of III-V materials and a few devices. To begin with, optical characterization of Aluminium Gallium Arsenide (AlGaAs) waveguides with enhanced nonlinear optical interactions was carried out. We have experimentally demonstrated wide conversion ranges and high conversion efficiencies for four-wave mixing in AlGaAs waveguides with three different geometries. In addition to that, both linear and nonlinear losses in each of these geometries were explored.

AlGaAs represents only one compound of the large group of III-V semiconductors. To explore the potentials of other semiconductors compounds of this group for nonlinear optics, it is imperative to have information about refractive indices of different III-V compounds. This refractive index information is only available for some binary compounds in isolated spectral windows. In this thesis, we developed a model capable of predicting the values of the refractive indices of binary, ternary and quaternary III-V semiconductor compounds from the values of their band-gap energies.

We compared the value predicted by our proposed model with existing experimental data and it was found not only is the predicted values in good agreement with the known values, but also has a lower error margin when compared to previously reported models. Finally, in quest for more suitable material platform for nonlinear photonic integration at different wavelength ranges, a detailed analysis of other potential III-V compounds not previously explored for photonic integration is presented.

Acknowledgements

I would like to express my profound gratitude and deepest appreciation to my supervisor, Prof. Ksenia Dolgaleva for her support, guidance, and wise supervision. Her deep insights and invaluable lessons helped me at many stages of my research and in my overall growth as a researcher. She is a great teacher and an amazing mentor. I feel very fortunate and honored having her as my supervisor and being a part of her research team.

I am particularly thankful to our post doctoral fellow, Daniel H. G. Espinosa for his immense contributions in all the projects outlined here, from the setting up of the Four-Wave Mixing experiment in AlGaAs, as detailed in Chapter 2, to validating results and data for the generalized refractive index model detailed in Chapter 3. Through his vast experience, these projects were completed with less complications and success.

Special thanks to our recently graduated Doctoral student, Kashif Awan, who performed the design and fabrication of AlGaAs waveguide structures detailed in Chapter 2, and provided input in the development of the generalized refractive index model, detailed in Chapter 3. His experience in fabrication was of great importance in the quest for new materials detailed in Chapter 4.

Many thanks to my fellow graduate and undergraduate students from Prof. Dolgaleva's research group and the much larger group, the CERC uOttawa group, who in diverse ways have contributed to these projects and also as a source of inspiration in my journey as a researcher.

Finally, I would like to express my profound gratitude to my mother Patricia, sister Madis, and my brother Etuks for their endless support and encouragement in every steps of my life. This accomplishment would not have been possible without them.

Contents

List of Figures

Dedicated to my mother, brother, sister and her family.

Chapter 1

Introduction

1.1 Motivation

Optical communication and data networks continues to see massive improvements and upgrades in performance as emerging technologies allow for increased data rates. With this increment in high bandwidth processes and applications such as video sharing, data mining systems, there is need for higher processing capabilities in the processing systems as the trend continues to grow.

Cisco forecast predicts that the global mobile traffic amounted to about 7.2 exabytes per month at the end of 2016 up from 4.4 exabytes per month at the end of 2015 is projected to rise up to 49 exabytes per month at compound annual growth rate of 47% in 2021. This translates to annual traffic exceeded by half a zettabyte. In 2018, this trend has already been surpassed, upping an outstanding 52.2% [1]. In 2019, mobile traffic has already reached 28.56 exabytes per month and it is expected to reach 77.49 exabytes per month by 2022. More of this increase is expected in the course subsequent months following the introduction of 5G technology in April 2019 in the US.

Smartphones represented only 45% of the mobile devices and connections in 2016 but now represent 81% of the total mobile traffic, with mobile video accounting for more than 60% of the total mobile data traffic in 2016 and increasing [2].

The projected demand for high-bandwidth services and processes in data networks requires improvement in optical and electronic technologies. However, the current optical networks have speed and functionality limited by their dependence on microelectronics. Although microelectronics continues to improve, further scaling of switching components such as transistors will be limited by the resolution achievable by available fabrication technologies and materials, thereby making the physical fabrication of these devices restricted in scale to no less than a few nanometers. This also greatly increases the underlying problem of heat dissipation in these devices. Overall, this issue largely hinders further improvement in processing speed and in transmission bandwidth.

Optics has been playing a central role at all the stages of optical network development. Wavelength division multiplexing (WDM) and erbium-doped fiber amplifiers (EDFA) introduced to the network in 1990s, gave start to submarine network deployment, while offering a huge economy and capacity burst to all tiers of optical networks. The emergence of optical bypass technology in late 1990s brought about a new generation of optical-bypass-enabled networks where it became possible to significantly alleviate the dependence on expensive electronic signal processing, and to remove a considerable amount of electronics from the networks' nodes, thereby improving the network cost, capacity and reliability.

Integrated photonics, entering the optical communications market in 2000s, allowed for another economical breakthrough and improved network reliability through enabling large-scale photonic integration. Fully integrated transmitters and receivers, capable of handling tens and hundreds of information channels on a single optical chip with the dimensions of only 1×1 cm, have replaced bulk optical components that introduced reliability issues and dramatically increased the network cost with the growth of the number of information channels.

In the existing optical networks, the approaches and techniques used in signal processing require converting the signal from optical domain to be processed in electrical domain. Electronic signal processing of high-data-rate channels requires very expensive electronics. Moreover, the fundamental limitations associated with the speed of electronic processing impose restrictions on the ultimate speed of an information channel. These problems can be alleviated if optical signals can be processed directly in optical domain. This approach is known as all-optical signal processing. To bring all-optical signal processing to the practical level, it is necessary to develop integrated photonic devices capable of efficient nonlinear wavelength conversion. Further sections in this chapter explain all the fundamental ingredients of this approach.

1.2 Integrated Photonics

Nonlinear photonics on-a-chip would benefit from creating low-cost, compact devices combining passive and actives optical components placed on the same photonic chip. Fig. 1.1 shows a schematic example of an integrated photonic circuit. In this example circuit, the light is coming from an integrated on-chip laser source that produces coherent narrow-band radiation. The laser is followed by an input coupler that serves for coupling the laser output to the optical waveguide that channels the light farther on the chip. Optical modulator is comprised of two branches for splitting the light two ways and recombining it to allow it to interfere in minimum or in maximum, thereby performing modulation of optical signals. It is used to imprint information onto certain degrees of freedom associated with light (intensity, polarization, phase). Photonic crystals are dielectric structures with band-gap that forbids propagation of certain light of certain frequency ranges, used here as a filter to optically select the frequency of the light for the photo diode that measures the optical power of the light. The optical ring resonator is essentially a set of waveguides coupled in a closed loop to some input and an output. Based on the concept of constructive interference, the light of certain wavelengths is passed from the input waveguide to the ring. Then it cycles the resonator multiple times and outputs to the output bus. Because only light at a certain resonant frequency will be at resonance within the loop, the ring resonator functions as a filter allowing only a narrow band of the frequency of the light generated by the sources. Typical examples of such integration find application in biomedical surface imaging and in oximetry (analytic sensing) requiring non-invasive approach to bio-recording where light is generated and shone on the skin, then blood volume changes in the

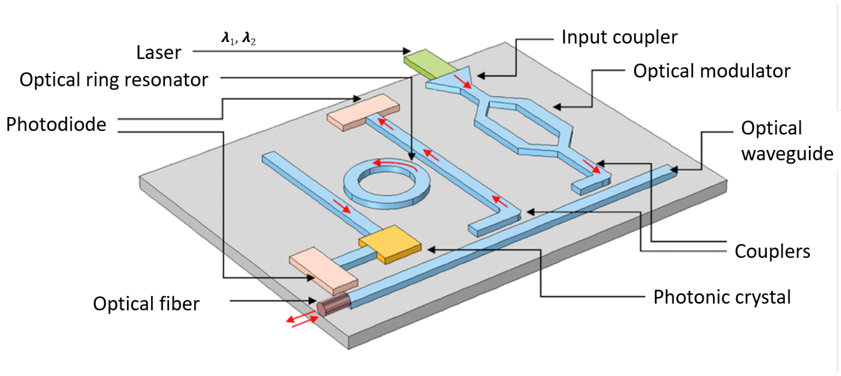

FIGURE 1.1: Schematic of the photonic integrated circuit (not to scale), showcasing different optical components reproduced from B. Saleh *et al.* [3].

microvascular bed of the skin tissue could be detected as in the case of photoplethysmogram. This same unit could be used to record electrocardiogram (ECG) and Electromyography (EMG) which in this case would need filters (photonic crystals and ring resonators) to separate different frequencies of the signal captured.

Various components on an integrated optical chip require different material response properties with respect to the wavelength of interest. For a laser source, the wavelength of interest must match the energy gap (so that it falls within the emission band), for the detectors, it must exceed the energy gap (for the photons to be efficiently absorbed by the semiconductor material). For passive devices such as waveguides and splitters, the wavelength of interest should not exceed the energy gap so that there is no absorption loss. Ideally, it would be practically easier to implement all applicable photonic integration on a suitable material platform capable of accommodating for all kind of integrated devices. This approach is called *monolithic integration*.
With all the benefits of monolithic photonic integration, there exist a fundamental limitation in achieving this goal, this limitation is centered around the complexity of selecting suitable materials. Indeed, an ideal material should have suitable optical properties for both active and passive functionalities (this alone seems controversial to be achieved in a single material platform as these functionalities different design requirements and specifications). For optical signal processing, it is required that the material candidates exhibit the desired nonlinear optical properties: strong useful nonlinear optical effects at the expense of negligible parasitic nonlinear effects, such as nonlinear absorption losses. To combine all these qualities in a way that monolithic integration of all optical components in a single material platform is possible, the material of choice should exhibit superior versatility and tailorability of its optical properties as would be discussed later in this chapter.

1.3 Nonlinear Optics

Nonlinear optics plays a significant role in optical signal processing. It describes interaction of light with matter in response to the application of electromagnetic fields with strengths sufficiently high in order to induce nonlinear material responses. Simply put, nonlinear effects are those effects where twice the optical input intensities do not directly result in twice the output intensities. Hence, nonlinear optical phenomenon is only observed and measurable with high intensity light. At low intensities, the nonlinear effects become very weak and the properties of the material remains independent of the incident light intensity. To understand this, we overview the background of this field and explain how optical nonlinearity can be used in optical signal processing operations.

Since optical nonlinearity results from the interaction of light with matter, the electric field of the incident light polarizes each atom or molecule in the material, where the induced polarization depends largely on the strength of the electric field of the incident light. To precisely describe nonlinear interaction, let's consider a dielectric material placed in an external time-varying electric field $\tilde{E}(t)$, the dielectric response of the medium is determined by the electric polarization $\tilde{P}(t)$ which is defined as the dipole moment per unit volume of a material, or simply put, polarization is the direction of the electric field of an electromagnetic wave. The electric displacement D is related to the electric field $\tilde{E}(t)$ and the polarization $\tilde{P}(t)$ through

$$D = \epsilon_0 \tilde{E}(t) + \tilde{P}(t). \tag{1.1}$$

In an isotropic medium where the microscopic dipoles are aligned along the direction of the applied electric field, equation 1.1 could be re-written as

$$\tilde{P}(t) = \epsilon_0 \chi^{(1)} \tilde{E}(t). \tag{1.2}$$

Eq. 1.2 represents the linear relationship between the strength of the incident electric field $\tilde{E}(t)$ and the induced polarization $\tilde{P}(t)$, where $\chi^{(1)}$ is a constant of proportionality also known as linear susceptibility and ϵ_0 is the permittivity of free space. However, as the electric field strength becomes significant, the relation in eq. 1.2 no longer holds. In this case, the optical response of this material can be written as a power series expansion of the polarization $\tilde{P}(t)$ with the strength of the applied optical field $\tilde{E}(t)$:

$$\tilde{P}(t) = \epsilon_0 [\chi^{(1)} \tilde{E}(t) + \chi^{(2)} \tilde{E}^2(t) + \chi^{(3)} \tilde{E}^3(t) + ...]. \tag{1.3}$$

where $\chi^{(2)}$ and $\chi^{(3)}$ are second and third-order nonlinear optical susceptibilities respectively. Therefore polarization $\tilde{P}(t)$ can be expressed as a sum of the linear and the nonlinear contributions

$$\tilde{P}(t) = \tilde{P}^{(1)} + \tilde{P}^{(2)} + \tilde{P}^{(3)} + ..., \tag{1.4}$$

where $\tilde{P}^{(1)}$ represents the linear polarization and the higher-order terms ($\tilde{P}^{(2)}(t)$, $\tilde{P}^{(3)}(t)$, *etc.*) are all together called nonlinear polarization [4]. Eq. 1.3 is the representation of dependence of the induced higher-order polarization on the strength of the incident electric field and is considered as the foundation for all nonlinear optical phenomena. It is also important to note that all $\chi^{(i)}$s are inherent material parameters describing the material response, hence they are fixed and unique for every material. In a given material, the linear susceptibility of the material is higher than the nonlinear susceptibility. However, even with the relatively small effect of the higher order $\chi^{(i)}$s, they collectively form nonlinear effect higher than the linear susceptibility at high optical field strength, making it possible to only notice nonlinear optical effects at high optical field strengths.

1.3.1 Nonlinear optical phenomena

To observe optical nonlinearity in a material as mentioned above, a light source of very high intensity is needed, in this case, a Laser. The efficiency of the nonlinear phenomenon is largely dependent on the type of material as well as their inherent response to the polarized incident light. A number of nonlinear optical effects can be observed, the most important of which are:

- Parametric nonlinearities: This nonlinear effect is a result of an instantaneous response based on the $\chi^{(2)}$ and $\chi^{(3)}$ nonlinearity of a material. Parametric nonlinearity arising from $\chi^{(2)}$ gives rise to effects such as parametric amplification, oscillation, sum-frequency generation (SFG), difference-frequency generation (DFG), and frequency doubling. In parametric nonlinearity, a phase matching condition would have to be satisfied in order to achieve a highly efficient process. Since parametric processes are polarization-dependent, the resulting nonlinearities are in essence polarization-dependent [5].

  Parametric nonlinearity arising from $\chi^{(3)}$ gives rise to effects such as self-focusing, self-phase modulation (SFM), cross-phase modulation (XPM) and four-wave mixing (FWM). These effects result from the rise in the refractive index of the medium by an amount proportional to the intensity of the incident light, also known as Kerr effect.

- Raman scattering (interaction of light with optical phonons) and Brillouin scattering (interaction of light with acoustic phonons) are related to the non-instantaneous part of the third-order nonlinear optical response.
- Two-photon or multi-photon absorption is another nonlinear effect where two or more photons are simultaneously absorbed by the atoms of the medium as the radiation propagates through the medium, thereby promoting an inter or intra-band transition where a single photon energy would not be sufficient to promote the excitation. Applications such as spectroscopy and fluorescence microscopy relies on this effect. However, multi-photon absorption reduces the efficiency of other nonlinear optical effects such as four-wave mixing and second-harmonic generation hence. For efficient nonlinear interaction in an optical process such as FWM, both linear and nonlinear absorption should be minimized.

1.3.2 Four-wave mixing

Four-wave mixing (FWM) is a parametric nonlinear effect arising from the third-order nonlinear susceptibility $\chi^{(3)}$. It appear as a consequence of an interaction of different frequency components with a nonlinear material and generation of a new frequency component as a consequence of the nonlinear modification of the refractive index of the material. If we assume that we have a nonlinear material interacting with three input optical beams having distinct frequencies ω_1, ω_2 and ω_3, the nonlinear contribution to the refractive index results in the FWM effect that generates a new frequency ω_4 in accordance with the following energy conservation relationship: $\omega_4 = \omega_1 + \omega_2 - \omega_3$.

In the case where all the frequency components are different, this type of FWM is called *non-degenerate four-wave mixing*. Fig. 1.2(b) shows the energy diagram of a non-degenerate FWM process. In this example, two *pump* photons with distinct frequencies ω_{p1} and ω_{p2} and a single *signal* photon of frequency ω_s interact with an optical medium, giving rise to a single *idler* photon with frequency ω_i. Fig. 1.2(a) displays a similar example with the difference that the two *pump* photons have equal frequencies ω_p (known as the *degenerate four-wave mixing*). Fig. 1.2(c) is the spectral representation of the degenerate FWM effect, where the *idler* component situated at the extreme left side of the *pump* component, appears as a consequence of FWM process.

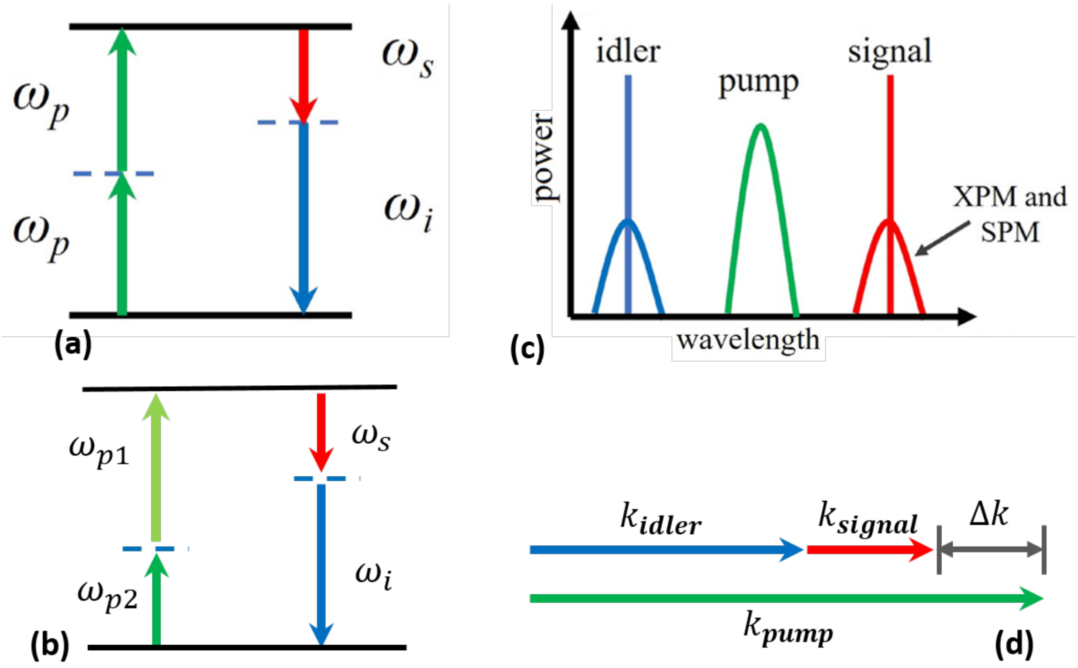

FIGURE 1.2: (a) Energy level diagram for degenerate FWM, (b) generation of new wavelengths via non-degenerate FWM (c) spectral representation of FWM (d) phase matching condition for FWM.

Because FWM is a parametric nonlinear process and the interaction depends on the relative phases of each beam, a phase-matching relationship where

$$\Delta k = 0, \tag{1.5}$$

between these interacting waves needs to be satisfied. In the case of a degenerate FWM, Δk can be defined as

$$\Delta k = 2k_{\text{pump}} - k_{\text{signal}} - k_{\text{idler}}, \tag{1.6}$$

where k_{pump}, k_{signal} and k_{idler} are the wave-vectors of the pump, signal and idler waves, respectively. This is schematically illustrated in Fig. 1.2(d). Technically, Eq. (1.5) requires that Eq. (1.6) be fulfilled, and Δk in Fig. 1.2(d) is zero.

Substituting Eq. (1.5) and the expressions for the wave-vectors in Eq. (1.6) results in the angular frequency representation of the phase matching condition, written as

$$2\frac{n_{\text{pump}}\omega_{\text{pump}}}{c} = \frac{n_{\text{signal}}\omega_{\text{signal}}}{c} + \frac{n_{\text{idler}}\omega_{\text{idler}}}{c}. \tag{1.7}$$

Using the law of conservation of energy, this phase matching condition can also be rewritten as

$$2n_{\text{pump}} = n_{\text{signal}} + n_{\text{idler}}. \tag{1.8}$$

However, because of the material dispersion, it is impossible to achieve perfect phase matching owing to the differences in the refractive indices for the pump n_{pump}, the signal n_{signal} and the idler n_{idler}. Refractive index is an increasing function of frequency under the conditions of normal dispersion. Therefore, in order to achieve an efficient FWM, the interacting frequencies should be either close to each other, and/or the dispersion management needs to be deployed.

All-optical signal processing is achieved by relying on the nonlinear optical interactions such as FWM, SFG, DFG, and XPM [6]. These effects have been shown to enable basic processing functions such as all-optical signal routing, all-optical wavelength conversion - direct frequency conversion with no reliance on microelectronics, switching [7], channel extraction [8], regeneration [9], *etc.* In this work, we focus on degenerate FWM in integrated optical waveguides. Below we provide the description of how this effect can be used for all-optical signal processing.

1.3.3 All-optical wavelength conversion using FWM

All-optical wavelength conversion is a major process in optical signal processing. This effect uses the optical nonlinearity of the material – either second-order nonlinear effects (SFG, DFG) or third-order effects (XFM, FWM). To understand how all-optical wavelength conversion can be realized by FWM, let us consider a laser beam with modulated frequency ω_s, carrying a bit stream of data, as shown in Fig. 1.3(a). This modulated beam (signal) is then synchronized with a non-modulated pulse stream (pump) with frequency ω_p [see part (b) of Fig. 1.3], and the interaction of these two frequencies with a nonlinear optical medium results in a generation of a new beam, the idler, at a frequency ω_i, shown in Fig. 1.3(c).

The interaction between these two beams happen in a manner that, whenever the bit of the modulated beam (ω_s) is "1", a "1" bit at the idler (ω_i) is generated, and whenever the bit of the modulated beam is "0", there is no radiation at ω_i or "0" is generated. This process is synonymous to the "AND" logic gate (Mixing "1" with "0", we get "0", and mixing "1" with "1", we get

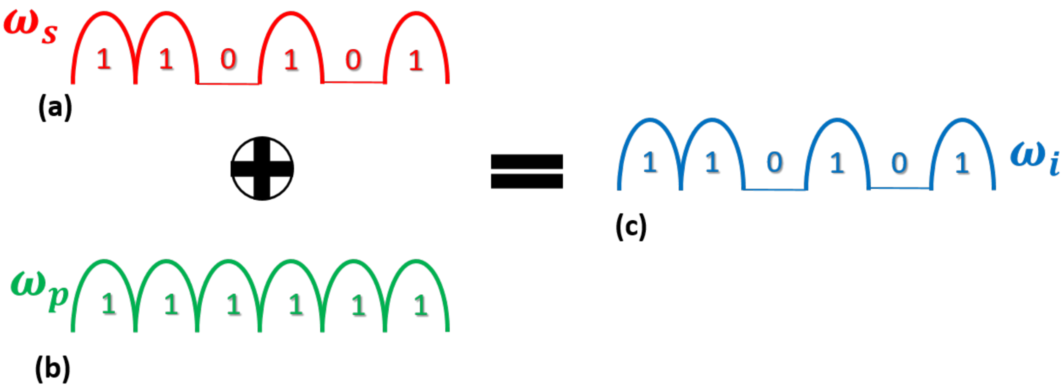

FIGURE 1.3: (a) Modulated signal frequency component, (b) non-modulated pulse stream, (c) generated idler frequency component carrying information imprinted in signal.

"1"). The result of this process is a reproduction of the original bit sequence but at a new frequency ω_i, hence the signal is converted to a new wavelength that can be transmitted through a filter, eliminating the residual pump and signal bit sequences.

1.3.4 Optical Time Division Multiplexing

Optical Time Division Multiplexing (OTDM) allows several optical signals to be combined, transmitted together on the same medium and then separated at different time slots. As with all-optical wavelength conversion, FWM and the logic "AND" gating can be used to achieve OTDM. To demonstrate this, assume three lower-bit channels to be multiplexed into a higher bit-rate steam, as illustrated in Fig. 1.4. To achieve this, we need two extra non-modulated pulse streams. The first stream would be at the same bit-rate as the ultimate bit rate of the multiplexed channels ("empty channel"), and the second pulse would be used to set up a temporal frame. The timing of these pulses would be such that the difference in the two consecutive pulses in the channel would fit a single bit of all three channels. We would also need to synchronize and offset the bits of the three information channels with the non-modulated "empty" channel, and in this case, an optical delay line would be used (*e.g*, optical fiber). The non-modulated framing and the high-bit-rate pulse streams is be mixed with all three channels. The delay lines are used to offset the three channels with respect to each other in the following manner: the first bit of the channel 1 overlaps in time with one of the pulses of the high-bit-rate stream, the first bit of the channel 2 overlaps with the second pulse of the high-bit-rate stream, and the first bit of the channel 3 overlap

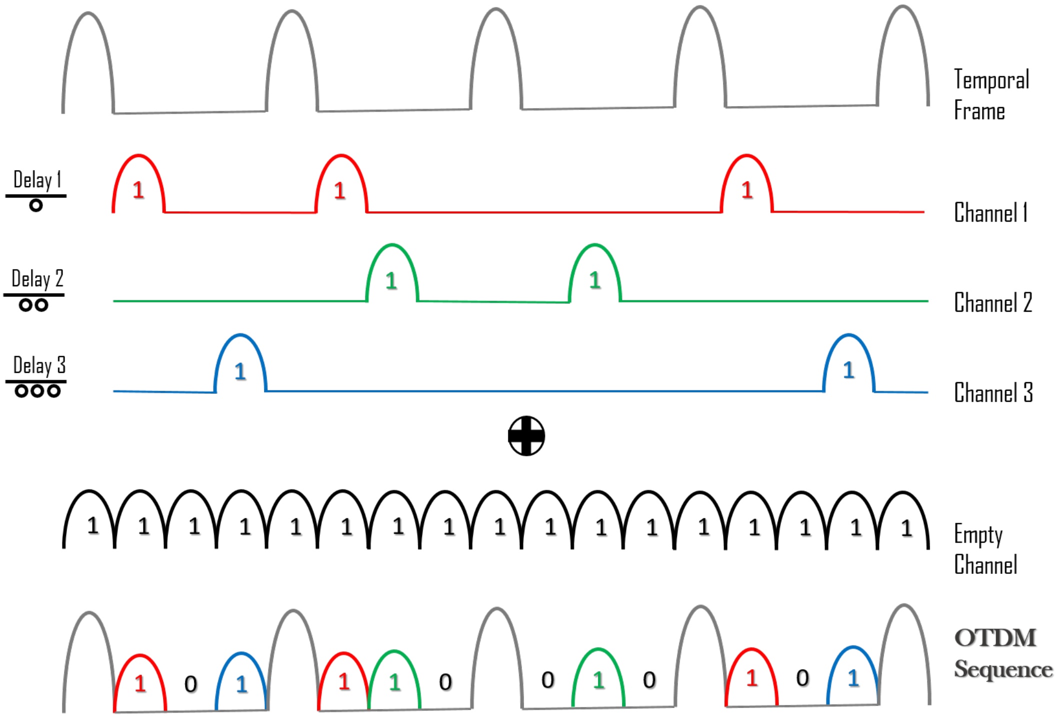

FIGURE 1.4: Four-wave mixing of three channels and two non-modulated pulse streams resulting in the multiplexing of the three channels into a higher-bit-rate stream.

with the third pulse, and the fourth pulse of the “empty channel” overlaps in time with the non-modulated framing pulse, as seen in Fig. 1.4. With efficient FWM between the interacting channels and the two non-modulated beams, an optical “AND” gate is realized. The resulting sequence is a higher-bit-rate multiplexed stream with separate time slots divided by the framing pulses. With this same approach, Optical Time Division Demultiplexing could be achieved.

1.4 Waveguide Optics

In this section, we provide an overview of the fundamentals of waveguide optics which represents the basis for integrated optical waveguides. One can understand wave guiding from the laws of Ray Optics, which represents an approximation where the wave nature of light is neglected. It is, however, not possible to explain the electromagnetic field distribution inside the waveguide structures in the framework of Ray Optics, and it is necessary to resort to Wave Optics. Here, we provide a conceptual explanation of the nature of light guiding on-a-chip using both approaches. We start from the simplest: the Ray Optics approximation.

1.4.1 Ray Optics Representation

Light rays incident on the interface between two transparent optical media, such as, for example, water and glass, or air and glass, could be totally or partially reflected at the interface, and could undergo a refraction and be partially transmitted to the second medium.

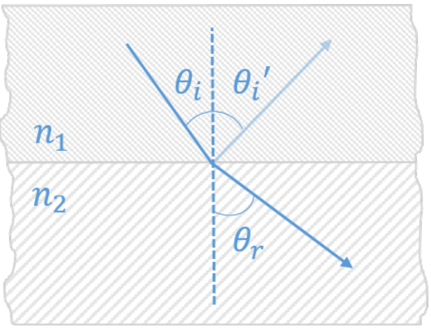

FIGURE 1.5: Reflection and refraction of Light at an interface.

Consider an example illustrated in Fig. 1.5, where light traverses an interface between the media with the refractive indices n_1 and n_2. In this illustration, we show both the reflected and refracted rays. The absorption of the light energy along its path is neglected, though it is an important parameter when designing optical systems. A ray of light is represented by a solid line with an arrow showing the direction of travel, and the dotted line indicates the line perpendicular to the surface (the normal) at the point of incidence. The Law of Reflection states that, when light reflects from a plain surface, as shown in Fig. 1.5, the angle between the reflected ray and the normal is equal to the angle between the incident ray and the normal ($\theta_i = \theta_i'$), and that the incident ray, the reflected ray and the normal all lie in the same plane.

The Law of Refraction states that, just as in reflection, the incident and refracted rays lie in the same plane. The angles of incidence and refraction are, however, different and obey the Snell's Law:

$$n_1 \sin \theta_i = n_2 \sin \theta_r. \tag{1.9}$$

This change of angle is caused by the change in speed of light as it travels the interface. From this relation, the greater the refractive index, the more the light bends in, and the slower is its speed in the medium. For example, moving from a medium with a lower index of refraction to a medium with a higher index of refraction, the light bends towards the normal to the interface, as shown in Fig. 1.5, and *vice versa*.

1.4.2 Critical Angle and Guidance

When light passes from a given material with a higher refractive index through an interface into a material with a lower refractive index, as shown in Fig. 1.6, there can be different scenarios, depending on the angle of incidence of the light ray with respect to the normal to the interface. As seen in the figure, four independence light rays, numbered 1 through 4, originating from O in a material with a higher refractive index and propagating through the interface to the material with a lower refractive index, the following is seen for each ray:

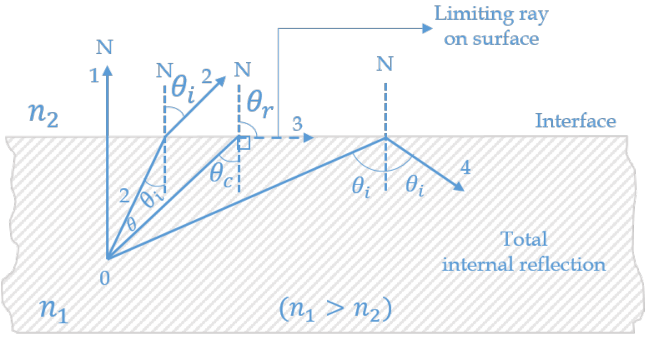

FIGURE 1.6: Critical angle and total internal reflection.

- There is no bending of Ray 1 as it traverses the interface while making an angle of 0^o with respect to the normal, continuing along the same direction in the second medium.
- Ray 2 is incident at an angle θ_i other than 0^o and bends away from the normal, making an angle θ_r in the second medium, as per the Snells's law [Eq. (1.9)].
- Ray 3 is incident at an angle θ_c that corresponds to bending of the refracted ray at an angle 90^o with respect to the normal, causing the ray to be "trapped" at the boundary of the two media and travelling along this boundary. This angle is known as *critical angle*. Using Snell's law, Ray 3 could be described mathematically as

$$n_2 \sin\theta_c = n_1 \sin 90^o = n_1, \tag{1.10}$$

and the critical angle is then defined as

$$\theta_c = \sin^{-1}\left(\frac{n_2}{n_1}\right). \tag{1.11}$$

- Ray 4 is incident at an angle greater than the critical angle, $\theta > \theta_c$, thereby resulting in a complete reflection of the ray into the originating medium. This phenomenon is known as *total internal reflection*.

Total internal reflection (TIR) represents the mechanism behind guidance in optical waveguides. The principle of optical confinement as seen in figure 1.7 is that a material with higher refractive index (n_1) is embedded in a medium of lower refractive index cladding (n_2) and this higher index medium layer acts as "traps" for the light traversing through it thereby making the light rays remain confined by multiple total internal reflections at the boundaries. Hence, this effect is exploited to make conduits that transports light from place to place.

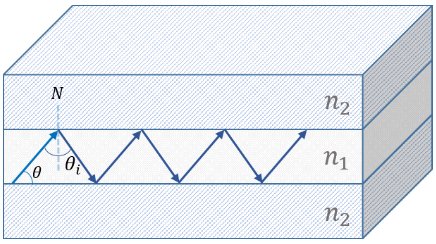

FIGURE 1.7: Optical confinement in waveguide using Total internal reflection.

1.4.3 Wave Optics Representation

As described above, Ray Optics generally explains the mechanism of light guidance in terms of total internal reflection at the interfaces between media with different refractive indices. It is, however, not capable of describing the electric field and intensity patterns formed inside an optical waveguide (its eigenmodes). For that, wave optics and electromagnetic theory of light are necessary. Below we summarize the crucial concepts forming the basis of mode analysis in guided wave structures.

Maxwell's equations forms the heart of electromagnetic theory of light. They describe the evolution of electromagnetic waves as they propagate in vacuum (or free space) and in optical media. From Maxwell's equation, the propagation of transverse electromagnetic waves in free space is given as

$$\nabla \times \mathbf{H} = \epsilon_0 \frac{\partial \mathbf{E}}{\partial t} \tag{1.12}$$

and

$$\nabla \times \mathbf{E} = -\mu_0 \frac{\partial \mathbf{H}}{\partial t}, \tag{1.13}$$

where ***E*** and ***H*** are electric and magnetic fields, respectively.

In free space, there are no free charges, and there are no magnetic charges in general. These fields are reflected in the following two equations,

$$\begin{gathered} \nabla \cdot \boldsymbol{E} = 0, \\ \text{and} \\ \nabla \cdot \boldsymbol{H} = 0. \end{gathered} \tag{1.14}$$

When we consider the propagation of an electromagnetic wave in a medium, Maxwell's equations take form

$$\nabla \times \mathbf{H} = \frac{\partial \mathbf{D}}{\partial t}, \tag{1.15}$$

and

$$\nabla \times \mathbf{E} = -\frac{\partial \mathbf{B}}{\partial t}, \tag{1.16}$$

where ***D*** and ***B*** are electric and magnetic inductions, respectively. These vectors are defined as

$$\boldsymbol{D} = \epsilon_0 \boldsymbol{E} + \boldsymbol{P}, \tag{1.17}$$

and

$$\boldsymbol{B} = \mu_0 \boldsymbol{H} + \mu_0 \boldsymbol{M}. \tag{1.18}$$

with ***P*** and ***M*** being the polarization and magnetization of the electric field, respectively.

Eqs. (1.17) and (1.18) are called *constitutive relationships*. They describe the material response of the medium to the incident electromagnetic wave propagating through it. Specifically, the material response parameters entering the equations are in the polarization and magnetization that get induced in a material medium by the applied field. Typically, in most of the cases of interest, $\mathbf{M} = 0$. The polarization is determined according to Eq. (1.3) and can be linear and nonlinear, depending on the applied field's strength. The coefficients of proportionality, shown in Eq. (1.3) as $\chi^{(i)}$, represent the material response parameters, linear ($i = 1$) and nonlinear ($i > 1$) susceptibilities. These are material characteristics; they are unique for a specific material.

Similar to Eqs. (1.19), we can write

$$\begin{aligned} \nabla \cdot \boldsymbol{D} &= 0, \\ \nabla \cdot \boldsymbol{B} &= 0. \end{aligned} \tag{1.19}$$

for the inductions in case if there are no free charges, which is true for all the situations considered within this thesis.

The set of Maxwell's equations, including Eqs. (1.15) through (1.19), governs the propagation of the electromagnetic field in a medium. As discussed earlier, in waveguide optics, we deal with interfaces between different dielectric materials, and the light can behave differently as it traverses an interface between two media, depending on the refractive indices (or dielectric constants) of the media and the polarization of light. To describe the light's behavior at the interface between two media, there exist *boundary conditions* relating different components of the electric and magnetic fields and inductions at the interface. Specifically, the tangential component of electric and magnetic field and the normal components of the electric and magnetic inductions should be continuous across the interface between the two media, establishing a set of boundary conditions for the propagation in the medium. This is illustrated in Fig. 1.8. A set of Maxwell's equations [Eqs. (1.15)–(1.19)] with the boundary conditions represent the tool to solve for the electric field distribution inside a waveguide structure. In many cases, there exist analytical solutions, while in some cases of more complex structures, numerical methods are necessary in order to solve for the waveguide mores. Below, we consider the simplest structure, a symmetric slab dielectric waveguide,

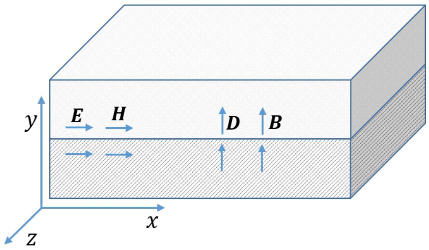

FIGURE 1.8: Boundary condition in a dielectric medium.

where analytical solutions exist. We provide the mode analysis of this structure. All the concepts associated with slab dielectric waveguide apply to more complex waveguides with 2D mode confinement, as discussed later.

1.4.4 Electromagnetic field polarization

Looking at Fig. 1.8, one could see that the electromagnetic fields E and H do not have y-axis dependency, therefore setting $\partial \boldsymbol{E}/\partial y = 0$ and $\partial \boldsymbol{H}/\partial y = 0$, hence, two independent electromagnetic modes are obtained: *transverse electric* (TE) and *transverse magnetic* (TM), respectively. Modes are fields that maintain the same transverse polarization and distribution at all cross-sections of the waveguide along its propagation axis. As seen in Fig. 1.9(a), the electric component along the z-axis is zero ($E_z = 0$) and the electric field lies in the plane perpendicular to the z-axis, the electromagnetic field distribution corresponds to the TE mode.

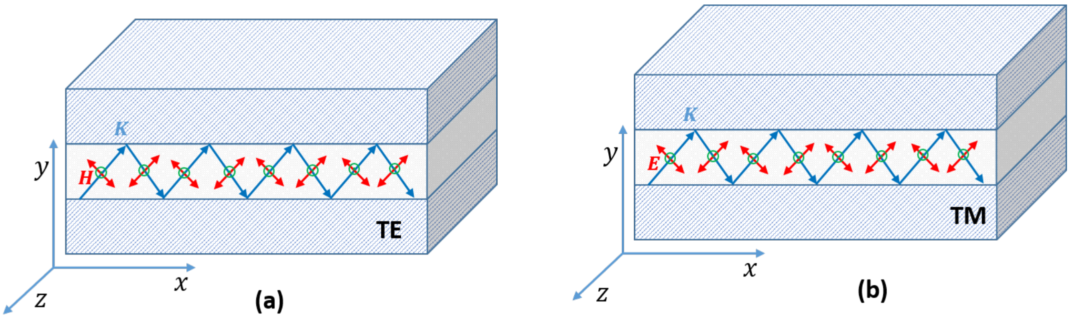

FIGURE 1.9: Schematic representation of (a)Transverse Electric (TE) Mode, (b) Transverse Magnetic (TM) Mode.

Also in figure 1.9(b), the magnetic component along the z-axis is zero ($H_z = 0$) and the electric field lies in the plane perpendicular to the z-axis, the electromagnetic field distribution corresponds to the TM mode.

1.4.5 Waveguide Modes

To better understand waveguide modes, consider a planar dielectric slab waveguide as shown in figure 1.10 with thickness d and refractive index n_1, sandwiched between two semi-infinite regions with refractive index n_2 where n_2 is less than n_1. The region with higher refractive index (n_1) is called the *core* while the region with the lower refractive index (n_2) is called the *cladding*.

Consider a monochromatic TEM plane wave of wavelength $\lambda = \lambda_0/n_1$, the

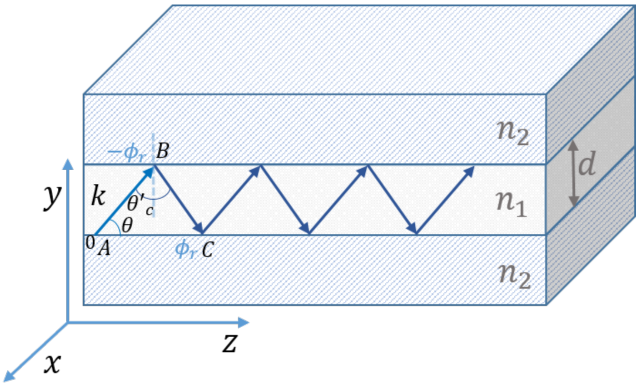

FIGURE 1.10: Schematic representation of a planar dielectric waveguide illuminated at one end by a monochromatic light source.

wave-number $k = n_1 k_o$, travelling with a phase velocity $c_1 = c_o/n_1$, and with wave-vector components $k_x = 0, k_y = n_1 k_0 \ \sin\theta, k_z = n_1 k_0 \ \cos\theta$ where n_1 is the refractive index of the core. The TEM wave is polarized in the x direction, meaning the wave vector lies in the y-z plane, making an angle θ with the z-axis. A light ray can propagate along such waveguide in a zig-zag manner as long as it undergoes total internal reflection at the boundaries, as illustrated previously. Like in ray optics, the wave reflects from the boundary of the top cladding-core interface and reflects from the lower cladding-core boundary, travelling at an angle greater than the complimentary critical angle θ'_c and it continues on. Since these layers are parallel to the electric field, each reflection is accompanied by a phase shift of ϕ_r with no change in the amplitude and the polarization ensuring that the sum of each wave and its own reflection disappears making a zero-level field at the interfaces.

Geometrically, for constructive interference and self-consistency, the phase difference between the waves at the points A and C ($\nabla\phi_{AC}$) must be zero or a multiple of 2π:

$$\nabla\phi_{AC} = k_1(AB + BC) - 2\phi_r = m(2\pi), \tag{1.20}$$

with m = 0, 1, 2, ... as an integer. By geometrically evaluating the first two waves,

$$AB + BC = 2d\cos\theta. \tag{1.21}$$

where

$$\begin{aligned} AB &= BC \ \cos(2\theta), \\ BC &= \frac{d}{\cos\theta}. \end{aligned} \tag{1.22}$$

Hence, to propagate the wave in the waveguide, we need

$$m(2\pi) = k_1(2d\ \cos\theta) - 2\phi_r. \tag{1.23}$$

To determine the modes that can be supported by the waveguide, we now impose a self-consistency condition which requires that the wave reproduces itself as it reflects twice at the boundaries (AB and BC) making only two distinct plane waves. In one round trip, the twice-reflected wave lags behind the original wave by a distance $AC - AB = 2kd\sin\theta$ plus the phase shift ϕ_r at each of the interfaces.
For the TE mode,

$$\begin{aligned} k &= (0, k_y, k_z), \\ &= (0,\ n_1k_0\ \sin\theta,\ n_1k_0\ \cos\theta). \end{aligned} \tag{1.24}$$

This yields self-consistency condition (TE Modes):

$$\begin{aligned} \tan\frac{\phi_r}{2} &= \sqrt{\frac{\sin^2\theta_c'}{\sin^2\theta_c} - 1}, \\ &= \tan(\pi\frac{d}{\lambda}\sin\theta - m\frac{\pi}{2}). \end{aligned} \tag{1.25}$$

Eq. 1.25 is represented graphically by Fig. 1.11 to determine the bouncing angle of the modes θ_m made by the wave as it bounces in the dielectric waveguide. The RHS and the LHS of eq. (1.25) are plotted against $\sin\theta$ with $\sin\theta_m$

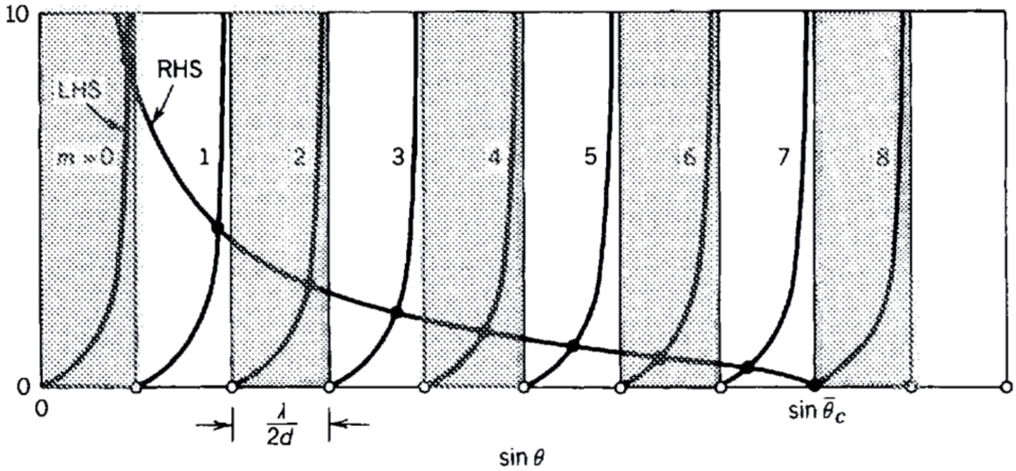

FIGURE 1.11: Graphical solution of the self-consistency condition for TE modes, as provided by Eq. (1.25). Reproduced from E. Saleh *et al.* [3].

determined by the intersecting points and marked with filled circles. Each branch of the tan or cot function in LHS shows the modes, represented by curves, where the curve $\tan(\pi d/\lambda)\sin\theta$ is generated when m is even and $\cot(\pi d/\lambda)\sin\theta$ curve when m is odd.

Fig. 1.11 shows plot for $\sin\ \theta'_c = 8(\lambda/2d)$ with 9 modes [3]. As it can be seen from Fig. 1.12, each of these travelling waves show distinct field patterns and making an angle θ_m with the boundary constituting a *mode of propagation*, with the integer m identifying the mode's order, and is called *mode number*. For each mode m, there will be one allowed angle θ_m and one corresponding phase angle ϕ_m. Dividing Eq. (1.23) by 2, we obtain the *waveguide condition* given by

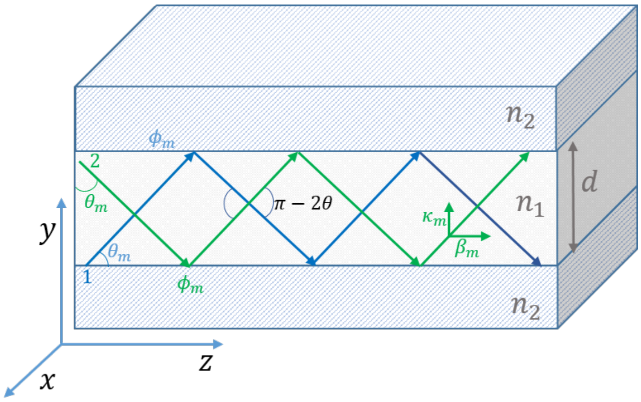

FIGURE 1.12: Schematic representation of a planar dielectric waveguide showing two light rays travelling in the guide constructively interfering with itself to propagate successfully

$$\left[\frac{2\pi n_1(d)}{\lambda}\right]\cos\ \theta_m - \phi_m = m\pi. \tag{1.26}$$

The waveguide condition represents those special waves that can propagate in the medium without being lost due to radiation into the claddings. These so-called special waves have angles of incidence θ_m that must satisfy the waveguide condition as given in Eq. (1.26) in order to propagate.

1.4.6 Mode propagation constants

The bouncing angles θ_m lie between 0 and θ'_c, corresponding to the wave vectors with components $(k = 0,\ k_y = n_1 k_0\ \sin\theta_m,\ k_z = n_1 k_0\ \cos\theta_m)$. The wave vector can thus be represented in terms of its two projections, β and κ, along and perpendicular to the z-axis (see Fig. 1.12). Also, since θ_m satisfies the waveguide condition for a particular instance of m, subscript m is used to differentiate the particular wave vector with β_m and κ_m, corresponding to a particular mode and given by

$$\beta_m = k_1 \sin\theta_m = \left(\frac{2\pi n_1}{\lambda}\right) \sin\,\theta_m, \tag{1.27}$$

and

$$\kappa_m = k_1 \cos\theta_m = \left(\frac{2\pi n_1}{\lambda}\right) \cos\,\theta_m. \tag{1.28}$$

Here β_m is the mode propagation constant along the guide and κ_m is the transverse propagation constant.

Fig. 1.13 shows four modes and their respective bouncing angles. In this figure, the lowest mode, $m = 0$, with $\theta_m = 0$ travels axially. Higher-order modes (larger θ_m) exhibit more reflections and can partially penetrate into the cladding. This is not evident from the ray optics representation, but will become clear once we start discussing mode field distribution later in this section.

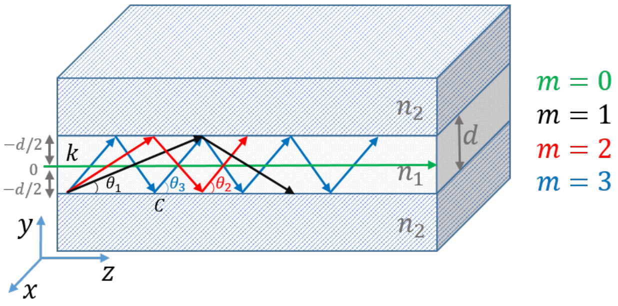

FIGURE 1.13: Schematic representation of a planar dielectric waveguide showing different modes with their bouncing angles.

1.4.7 Number of modes

As discussed above, a dielectric waveguide can support a number of modes. Looking at the mode plot in Fig. 1.11, one can notice that the abscissa has equal intervals with $\lambda/(2d)$, and the supported modes are marked with filled circles. Hence, the number of modes is the smallest integer greater than $\sin\theta_c'/[\lambda/(2d)]$, such that:

$$M \doteq \frac{\sin\theta_c'}{\lambda/(2d)}. \tag{1.29}$$

The symbol "$\doteq$" means that M is increased to the nearest integer. For instance, if $\sin\theta_c'/\frac{\lambda}{2d}$ = 0.7, 1.0 or 2.4, $M = 1, 2$, and 3 respectively. Specifically for the case of symmetric slab dielectric waveguide, there always exists at least one TE mode for all valued of the angles θ. The number of modes increases with an increase in the ratio of core height d to wavelength. When the wavelength is sufficiently long or the dielectric slab is sufficiently thin, a condition exist where $\lambda/(2d) > \sin\theta_c'$, only one mode is allowed. Such waveguide is known as a *single-mode waveguide*. Since the fundamental mode (m = 0) is always allowed, it therefore means that for a dielectric waveguide, there is at least one TE mode, hence each of the modes ($m = 1, 2, ...$) will have its own *cut-off wavelength* or frequency, the longest wavelength (the smallest frequency) that this mode can support.

For the first-order mode, the cut-off wavelength is given as:

$$\nu_c = \frac{\omega_c}{2\pi} = \frac{1}{\sqrt{n_1^2 - n_2^2}}\frac{c_0}{2d}. \tag{1.30}$$

For m^{th}-order mode, the cut-off frequency becomes $m\nu_c$.

1.4.8 Mode field distribution

The electric field of guided modes is concentrated inside the waveguide's core. On the other hand, it penetrates with its evanescent tails to the claddings (see Fig. 1.15). Therefore, there are internal and external field distributions associated with any waveguide mode. As discussed earlier, the internal field is comprised of two distinct TEM plane waves with the same amplitude and phase shift ($m\phi_r$) at half round trip at the center of the core and making an angle of ϕ_r and $-\phi_r$ with the z-axis and having wave vector components ($k = 0$, $k_y = n_1k_0 \sin\theta_m$, $k_z = n_1k_0 \cos\theta_m$). One can represent the complex amplitude of the electric field as $E_x(y, z) = a_m u_m(y)\exp(-j\beta_m z)$. Here the a_m is a constant, $\beta_m = n_1k_0 \cos\theta_m$ is the propagation constant, $\lambda = \lambda_0/n_1$ and

$$u_m(y) \propto \begin{cases} \cos\left(2\pi\frac{\sin\theta_m}{\lambda}y\right), \; m = 0,2,4,... \\ \\ \cos\left(2\pi\frac{\cos\,\theta_m}{\lambda}y\right) \; m = 1,3,5,.... \end{cases} \qquad -\frac{d}{2} \leq y \leq \frac{d}{2} \tag{1.31}$$

Here the field is harmonic, so, it does not vanish at the core-cladding boundary. Also, as m increases, $\sim \theta_m$ increases making the higher-order modes to vary increasingly with y.

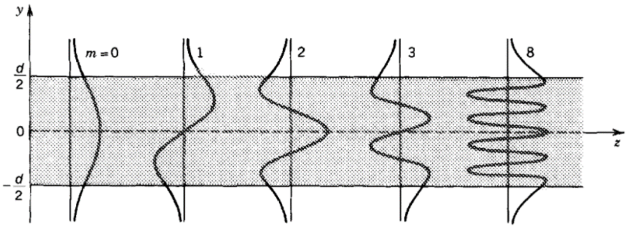

FIGURE 1.14: Field distribution for TE guided modes in a dielectric waveguide. Reproduced from [3]

The external field must to match with the internal field at all boundary points at $y = \pm d/2$, as shown in the field distribution graph in Fig. 1.15. This external field must vary with z as $\exp(-j\beta_m z)$. Since $\beta_m > n_2 k_0$ for guided modes, and the field must decay away from the boundary in the cladding media, we select the field depenfence to be $\exp(-\gamma_m y)$ in the upper cladding and $\exp(\gamma_m y)$ in the lower cladding, yielding

$$u_m(y) \propto \begin{cases} \exp(-\gamma_m y),\ y > \frac{d}{2} \\ \\ \exp(\gamma_m y),\ y < -\frac{d}{2}. \end{cases} \tag{1.32}$$

The field decay parameter γ_m is known as the *extinction coefficient*, and it is defined as

$$\gamma_m = n_2 k_0 \sqrt{\frac{\cos^2 \theta_m}{\cos^2 \theta_c'} - 1}. \tag{1.33}$$

As it is clear from the notation, each mode has its unique value of γ_m. As the mode index increases, θ_m decreases, and the extinction coefficient γ_m decreases resulting in a deeper penetration of the higher-order modes into the claddings.

To determine the constant of proportionality in Eqs. (1.31) and (1.32), the fields are matched at $y = \pm d/2$ and normalized as $\int_{-\infty}^{\infty} u_m^2(y)\, dy = 1$. This yields an expression for $u_m(y)$ valid for all y.

1.4.9 Superposition of Modes

Not all the waves guided by the waveguide have a field and intensity distribution matching one of the eigenmodes. If the wave satisfies the boundary conditions but its bouncing angle does not match one of the angles θ_m, it can

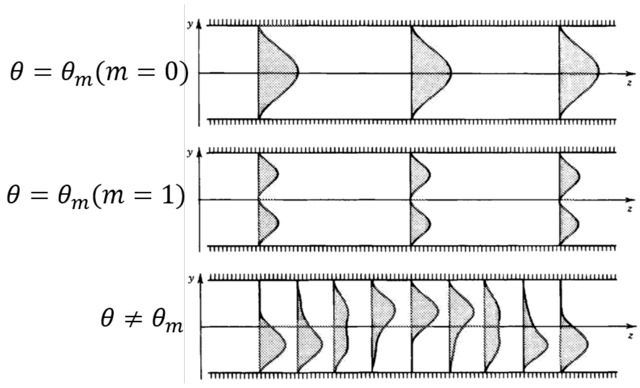

FIGURE 1.15: Variation of the intensity distributions in a waveguide core in the transverse direction y at different axial distances z. Reproduced from ref[3].

still be supported by the waveguide. However, the optical power is divided among all the modes. As different modes travel with different velocities and propagation constants, the field distribution changes as the wave propagates through the waveguide. As illustrated in Fig. 1.15, for a specific mode, the transverse distribution of the intensity is invariant with the propagation, but it varies with z for a superposition of modes. Hence, an arbitrary TE field in a dielectric waveguide polarized in the$x$ direction and satisfying the boundary conditions can be defined as a superposition of all the nodes, and can be written as

$$E_x(y,z) = \sum_m a_m u_m(y) \exp(-j\beta_m z), \tag{1.34}$$

where a_m is the amplitude of mode m.

1.4.10 Waveguides with 2D Confinement

Optical waveguides can be broadly classified based on their geometries into planar and channel waveguides. So far, we have been discussing planer waveguides, also known as slab waveguides, and used them for their simplicity to demonstrate principles of guided-wave optics. Such waveguides exhibit a 1D light confinement (they confine light in y-dimension). Channel waveguides have an additional restriction imposed on the spread of light in the lateral dimension (in addition to the vertical confinement). This restriction is typically defined by a ridge, rib or strip defined on top of the guiding layer. Based on the specific geometry, channel waveguides can be subdivided into rib, strip, strip-loaded, or embedded-strip waveguides, *etc* (see Fig. 1.16). An embedded-strip waveguide is designed with a high-index core buried in a low-index surrounding medium. A strip waveguide has a

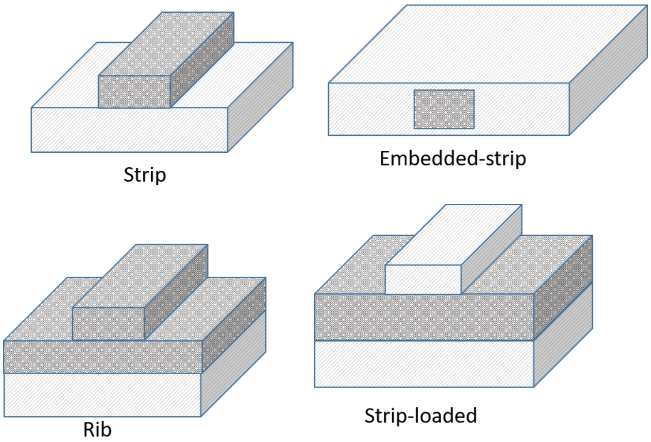

FIGURE 1.16: Schematic of commonly used channel waveguides[3].

strip of higher-refractive-index material on top of the lower-index substrate waveguide. A rib waveguide has a similar structure to that of a strip waveguide, but the strip has the same index as the high index planar layer beneath it and is part of the core. The strip-loaded waveguide is formed by loading a planar waveguide, which already provides optical confinement in the x-direction, with a dielectric strip of index $n_2 < n_1$ or a metal strip to facilitate optical confinement in the lateral direction. The mode concentrated in the core layer senses with its evanescent tails, penetrating to the upper cladding, the ridge, and the lateral confinement is realized as such. All these waveguide geometries are used to produce waveguides with two-dimensional confinement. The specific geometry is selected based on the material platform used. There are several options in terms of platforms, including Silica glass, Silicon, Polymers, Chalcogenide glasses, Lithium Niobate $LiNb_2O_3$, and III-V semiconductors. Below we review different materials used for photonic integration.

The Chalchogenide glasses are promising materials for photonic integration due to their high refractive index and low linear and nonlinear loss coefficients. However, they require sophisticated purification and fabrication processes and are, therefore, a very expensive technology. In addition, they cannot be used as a material platform for active devices such as lasers and detectors [10], [11].
Silicon is one of the most preferred candidates for all-optical networks, with its mature low-cost fabrication technology and capability to accommodate for both optical and electronic devices on the same chip. However, silicon has an indirect band-gap structure, hence, it is not an efficient light emitter.

A hybrid integration with other materials, for example, III-V semiconductors, would be needed. This approach, however, comes with compatibility issues between these platforms, adding cost to the integrated optical circuit, as well as limiting its capabilities [11]–[13]. Although silicon-based materials are not efficient light sources because it has indirect band gap structure, they however have very strong nonlinearity. It also suffers from significant nonlinear losses at telecommunication wavelength (1400 nm to 1600 nm) due to its very strong two-photon absorption which can limit the efficiency and speed of an all-optical device. In addition, there is a significant free-carrier absorption accompanying the two-photon absorption in silicon. As a result of all these drawbacks, silicon is not a very efficient material for all-optical signal processing at the telecommunications frequency range.

Lithium Niobate has very interesting and rich optical properties. It has very strong optical nonlinearity, birefringence, ferroelectricity, very high chemical stability, valuable electro-optic, acousto-optic and piezo-electric effects, and very high transparency. It also has a well-developed fabrication technology. These features makes it attractive for the design and manufacturing of of low-loss waveguides and integrated optical components, such as electro-optic modulators [14]. However, Lithium Niobate devices are often bulky and large in size, limiting the functionality to areas mainly in quantum communication [14], [15]. Moreover, Lithium Niobate is not an efficient light emitter and cannot be used for on-chip light sources.AlGaAs has a direct band-gap structure for Aluminium compositions less than 45%, which allows the combination of integrated laser sources, detectors and low-loss waveguides on the same chip without need for hybrid integration as in the case with Silicon. AlGaAs has a high refractive index, which results in waveguides with superior confinement. Moreover, it has the highest Kerr nonlinearity among the candidates for all-optical signal processing [11], [16], [17]. AlGaAs is a member of the group of III-V semiconductors which are the focus of the present master thesis research. The following section is devoted to the description of the characteristics of this group of materials.

1.5 III-V Semiconductors

III-V semiconductors are comprised of chemical elements from columns III and V in the periodic table of chemical elements. They have been the spotlight of attention due to their unique optical and electronic properties. In real world application of photonic systems, optical communications, sensing and interconnects, III-V compound semiconductors would be considered to be indispensable. Alongside the development of low-loss optical fibers, the first application of III-V semiconductors in optical telecommunication systems are serving as material platforms for light sources and photodetectors. InP and GaAs–based material systems have been playing crucial role in the development of high-speed electronic and high-reliability photonic devices. Transmission systems with up to tens of Tb/s have been successfully developed by continuous improvements in performance, reliability, cost and functionality using these material systems as laser and detector platforms, as well as integrated optical platforms for large-scale photonic integration. Also, the bandwidth achieved by such development has seen increment in rates exceeding 150% per year [6].

Indium Gallium Arsenide Phosphide (InGaAsP) allow for monolithic integration of both passive and active devices on the chip because it is a direct band-gap semiconductor. Furthermore, because it is a quaternary compound, it offers an additional advantage of being able to change the material composition from layer to layer to further tune its optical properties as will be shown in the next subsection. Adjusting the composition of individual elemental and binary compounds results in compounds with a wide range of unique optical properties. These properties could be tuned by adjusting the refractive index contrast, band-gap wavelength and material composition – the luxury that none of other material candidates for nonlinear photonic devices could offer.

Such parameter adjustment is only possible in ternary and quaternary III-V semiconductor compounds, comprised of three and four elements of the group III-V, respectively.

1.5.1 Ternary and Quaternary III-V Semiconductors

Ternary and quaternary compounds can be obtained by intermixing binary compounds of the group of III-V semiconductors. With the use of Ternary and Quaternary III-V semiconductors comes the flexibility of changing the band-gap wavelength, and this ability to tune the band-gap enabled several present-day commercial devices such as attenuators, multiplexers and demultiplexers, detectors, lasers, modulators and amplifiers. Ternary and quaternary compound semiconductors are schematically represented as $A_xB_{1-x}C$ and $A_xB_{1-x}C_yD_{1-y}$, respectively. They are schematically shown in Fig. 1.17, where A, B, C and D are individual constituent elements of the compound,

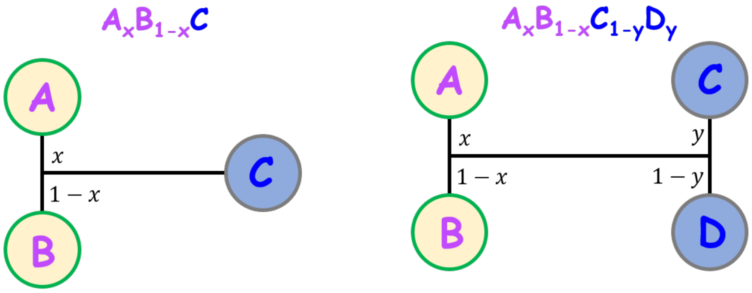

(a) (b)

FIGURE 1.17: Schematic diagram showing how (a) ternary and (b) quaternary semiconductors are formed

and the parameters x and y are the mole fractions of the elements with values ranging from 0 to 1 inclusive. Conventionally, for III-V semiconductor compounds, A and B are elements from column III, while C and D are elements from column V of the periodic table. The adjustment of the concentration is such that the sum of the pairs of molar fraction of the elements is equal to 1 ($i.e., x = 0.3, 1 - x = 0.7$ summing up to 1 and same for y). By changing the mole fractions of pairs of elements, one can change the properties of the overall compound such as its refractive index and nonlinear susceptibilities, as well as the absorption wavelength (as the band-gap wavelength equivalent changes).

Fig. 1.17(a) shows a schematic representation of a ternary III-V semiconductor compound, represented mathematically as $A_xB_{1-x}C$, where A, B, and C are individual constituent element or binary composition of the compound. Ternary semiconductor have one degree of freedom x. By varying$x$ the bang-gap energy as well as the refractive index of the material is adjusted.

Similarly, A quaternary compound has two mole fraction variables: x and y as seen in Fig. 1.17(b). They can be adjusted for both pairs A, B and C, D independently. Therefore, quaternary compounds typically have two degrees of freedom, while ternary compounds only have one degree of freedom owing the presence of a single variable x. For quaternary compounds, the adjustment of the energy gap can occur independently from the adjustment of the lattice constant of the material within some limits. This feature adds flexibility in designing integrated optical components.

1.5.2 Energy Gap and Lattice Constant

The dependence of the energy gap and the lattice constant on the compositions of the material is found from Vegard's law [18]. If the lattice constant or band-gap energy of a binary compound is known, Vegard's law allows one to find the corresponding unknown parameter (band-gap energy or lattice constant) for ternary or quaternary compounds. For a ternary compound, the unknown parameter (T_{ABC}) can be interpolated based on the existing knowledge of its constituent binary parameters T_{AC} and T_{BC} as follows

$$T_{ABC}(x) = xT_{AC} + (1-x)T_{BC}. \tag{1.35}$$

Similarly, for quaternary compounds, the the unknown parameter (T_{ABCD}) can be interpolated based on the existing knowledge of its constituent binary parameters T_{AC} , T_{AD} , T_{BC} and T_{BD} as follows

$$T_{ABCD}(x) = xyT_{AC} + x(1-y)T_{AD} + y(1-x)T_{BC} + (1-x)(1-y)T_{BD}. \tag{1.36}$$

In the design of integrated photonic devices based on ternary and quaternary III-V semiconductors, it is important to define the compositions of each individual layer (the substrate, the upper and lower cladding and the guiding layer). These layers should have equal or nearly equal lattice constants in order to grow the layer stack epitaxially on top of the substrate in a defect-free manner. If the layers are mismatched, then the material is subject to growth and lattice-mismatched defects, which degrades the optical quality of the material. More details about lattice matching are provided in sections 2.2 and 4.2.2. Lattice matched compounds lie on vertical line of the lattice constant plot, as seen in Fig. 1.18. Examples being AlSb and GaSb or GaAs and AlAs.

1.5.3 Direct Band-Gap and Indirect Band-Gap III-V Semiconductors

Semiconductor materials used for integrated photonic applications can be classified broadly into either direct band-gap or indirect band-gap semiconductors. The global minimum (lowest energy state) of the conduction band and the global maximum (highest energy state) in the valence band are described by a certain degree of crystal momentum in the Brillouin zone known as the "**k**-vector". If the highest energy state in the valence band and the lowest energy state in the conduction band have the same wave vector **k** in the

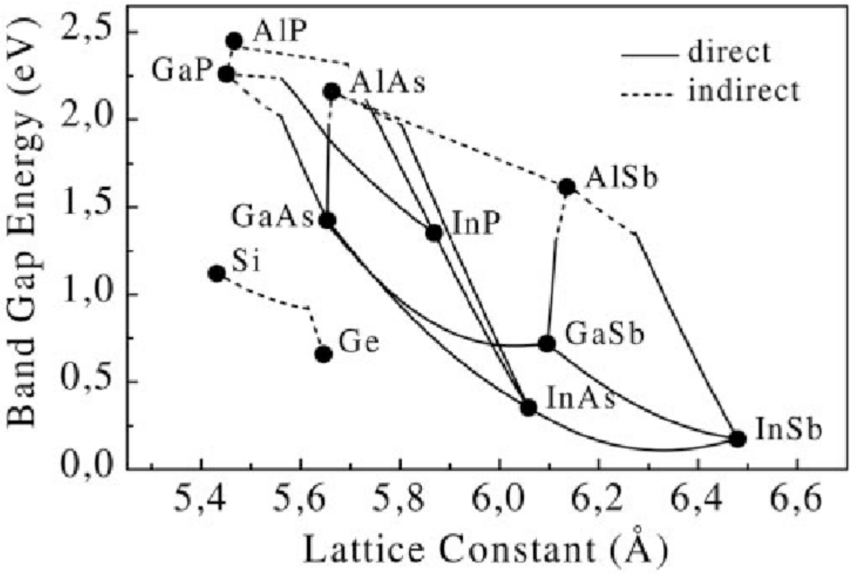

FIGURE 1.18: Plot of crystal lattice constant as a function of band-gap energy for commonly used binary III-V semiconductors, reproduced from Bett, *et al.* [3].

momentum space, then it is called a direct band-gap semiconductor. Otherwise, it is called an indirect band-gap semiconductor, where the band-gap of the material is the energy difference between the bottom of the conduction band and the top of the valence band, as shown in Fig. 1.19. When the electron in the conduction band recombines with the hole in the valence band, an emission of light (photon) with a certain energy equal to the difference between the energies of the excited state (in the conduction band) and the ground state (in the valence band) is possible. This process is called radiative recombination.

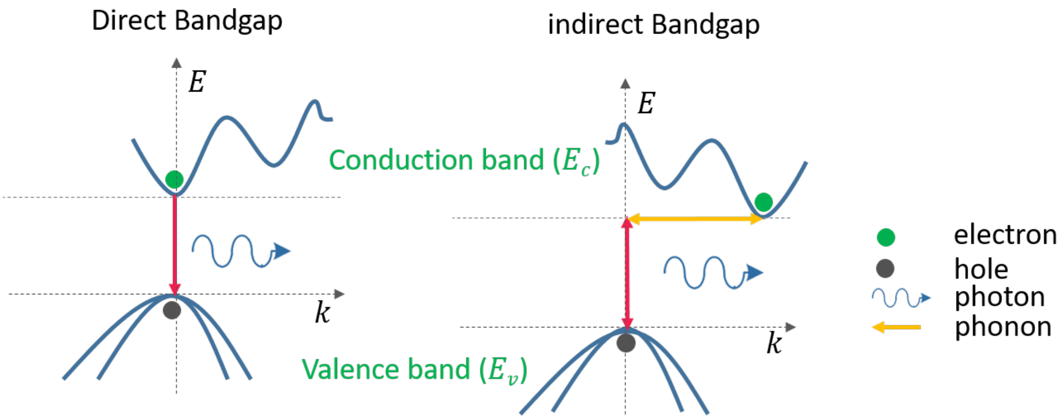

FIGURE 1.19: Schematic diagram showing radiative recombination in direct and indirect band-gap semiconductors

In direct band-gap semiconductors, since the positions of the valence band maximum and the conduction band minimum occur at the same value of the momentum, the energy and momentum conservation laws for radiative transitions are satisfied. Therefore, a photon with the energy equal to the energy difference between the excited and ground states (which is very similar to the band-gap energy) can be produced.

The radiative recombination of an electron-hole pair is a relatively efficient process in direct band-gap semiconductors because the momentum of an electron in this case does not change. However, in the case of indirect band-gap semiconductors, an electron at the bottom of the conduction band cannot easily recombine with the hole at the top of the valence band. Because of the momentum conservation low, such a recombination is only possible with an assistance of a phonon, a quantum of vibration of crystal lattice. Because it is highly improbable to time the photon emission and interaction with lattice vibration, radiative processes in indirect band-gap semiconductors have a very low probability of occurrence. Moreover, the electron undergoes a significant change in momentum as a result of these interactions thereby causing most of the energy in indirect band-gap materials to be lost in the form of phonons. As the result, the rate of the radiative recombination in indirect band-gap semiconductors is much slower compared to that in direct band-gap semiconductors, which makes indirect band-gap semiconductors not suitable for light emission. Applications such as LEDs (light emitting diodes) and Laser diodes require rapid radiative recombination, hence, direct-gap semiconductors can serve as efficient light sources while indirect band-gap semiconductors cannot.

1.5.4 Operation Wavelengths of Different Devices

Light of different frequencies can interact differently with a semiconductor material. The way the light interacts with the semiconductor depends on the value of its photon energy (or wavelength) in comparisson to the value of the band-gap energy (or band-gap wavelength equivalent). Let us introduce the conversion between the band-gap energy and the corresponding band-gap wavelength as it is convenient to compare light of certain color with a specific value of wavelength to the band-gap wavelength equivalent. The band-gap wavelength λ_g in the units of micrometers [μm] can be related to the corresponding band-gap energy E_g in the units of electronvolts [eV] in accordance with the following equation:

$$\lambda_{\mathrm{g}}\,[\mu\mathrm{m}] \approx \frac{1.24}{E_{\mathrm{g}}\,[\mathrm{eV}]}. \tag{1.37}$$

If the wavelength of light λ satisfies the condition $\lambda < \lambda_{\mathrm{g}}$, such light can be efficiently absorbed by the semiconductor material (as the energy of a single photon is sufficient to traverse the band-gap), and its propagation through the semiconductor will be very lossy. On the other hand, this situation is beneficial for building a detector made of the semiconductor material for the specific wavelength for which efficient absorption can occur.

A different situation arises when the energy of the photon or wavelength of light is comparable to the band-gap wavelength: $\lambda \sim \lambda_{\mathrm{g}}$. In this case, the light with such wavelength can experience some absorption as it propagates through the semiconductor material. On the other hand, if the semiconductor is prepared in an excited state (with more electrons at the bottom of the conduction band than at the top of the valence band), it can serve as an amplifying medium to the light with the wavelength comparable to that of the band-gap.

Yet another case corresponds to the wavelength of light satisfying the condition $\lambda > \lambda_{\mathrm{g}}$. In this case, the energy of the light's photons is insufficient for the electrons in the semiconductor material to be able to absorb the photons and get excited to the conduction band. In this situation, the semiconductor material appears as a transparent medium as the light with such wavelength propagates through it, as long as the intensity of the light is not high. Finally, for intensive light with $2\lambda_{\mathrm{g}} > \lambda > \lambda_{\mathrm{g}}$, it is possible to observe the absorption of two photons simultaneously by a nonlinear optical process called "two-photon absorption" (TPA). This process is only efficient when the intensity of light is sufficiently high. In integrated optical devices, at a very moderate level of optical power, we are still dealing with a very tight confinement of light in channel waveguides. Such strong confinement leads to high intensities even at relatively small values of optical power. As the result, two-photon absorption is readily observable in optical waveguides. Since it represents another mechanism of loss of useful optical power, it is highly desirable to work in the wavelength range below half-band-gap, *i.e.*, with the wavelengths satisfying $\lambda > 2\lambda_{\mathrm{g}}$, if the goal is low-loss light propagation, not detection, not photon emission. This wavelength range is perfect for passive nonlinear optical devices based on low-loss semiconductor waveguides, which is the primary topic of this thesis.

As earlier mentioned, one of the benefit of using ternary and quaternary III-V semiconductors is the capability of band-gap adjustment that these platforms offer. The band-gap wavelength can be shifted (within some limited range of values) in such a way that, for a specific wavelength of interest, one can find a material composition that doesn't exhibit linear and TPA losses. This freedom is not available in silicon and other materials competing with III-V semiconductors for the best platform for all-optical signal processing.

To summarize, different integrated optical devices have different restrictions imposed on the values of the light wavelength and band-gap wavelength equivalent. For passive nonlinear devices, the energy of the photon propagating through the semiconductor should be smaller than one-half of the band-gap energy of the material, or the band-gap equivalent wavelength should be less than twice the wavelength of the light interacting with the material ($\lambda_{\mathrm{g}} < 2\lambda$). For passive devices operating at lower levels of intensity, this requirement is more relaxed, and the wavelength of light should be greater than the band-gap equivalent wavelength of the material ($\lambda > \lambda_{\mathrm{g}}$). For laser sources, the band-gap equivalent wavelength should be approximately equal to the wavelength of the light interacting in the material ($\lambda \approx \lambda_g$). For detectors, the band-gap equivalent wavelength should be greater than the wavelength of light: $\lambda_{\mathrm{g}} > \lambda$. These constraints determines the operation wavelength range of the material, and/or the operation wavelength range of interest determines what material composition to use in the design of an optical devices.

1.5.5 Integrated Photonics in III-V Semiconductors

Integrated optical devices require refractive index contrast for light confinement. To achieve this requirement in III-V semiconductor platforms, a typical procedure is to grow a heterostructure comprised of layers with different material compositions. These layers have to be latticed-matched with the substrate and with respect to each other to minimize epitaxial stress or strain defects which could otherwise become one of the major sources of losses.

As discussed earlier, the group of III-V semiconductor materials constitutes a great variety of materials with different band-gap energies and different transparency windows, as schematically shown on the diagram in Fig. 1.20. It can be see from the diagram that III-V semiconductors cover the entire window from ultraviolet (UV) to infra-red (IR) with their band-gap energies.

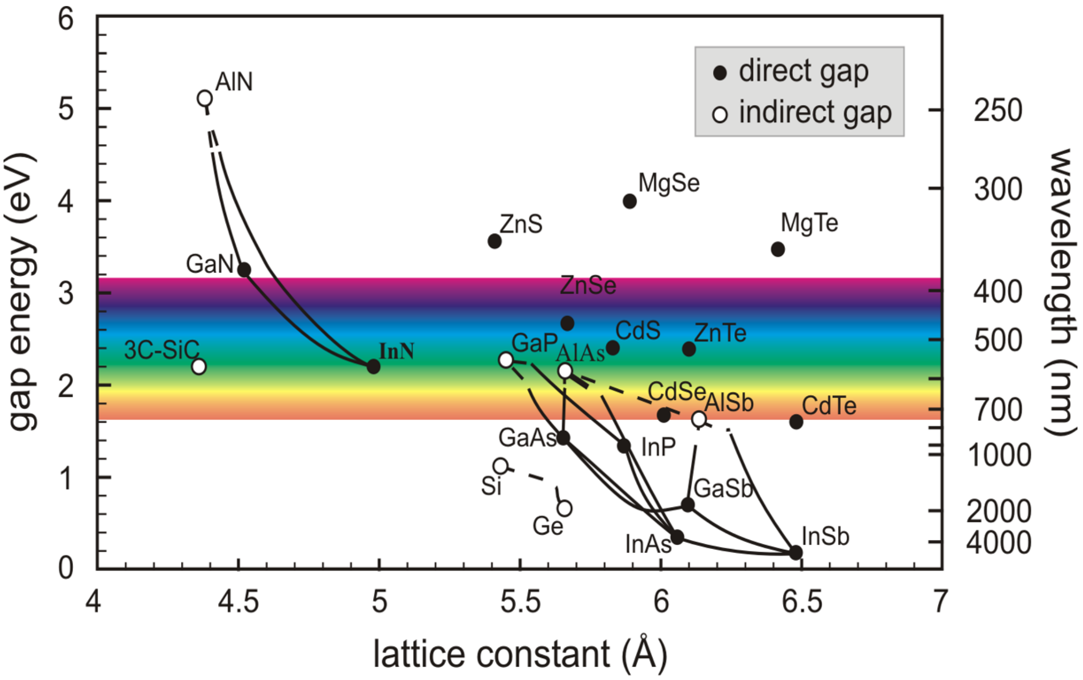

FIGURE 1.20: Band-gaps of the most important elemental and binary III-V semiconductors against their lattice constant at 300°K. The right-hand scale gives the light wavelength λ, of the corresponding band-gap energy. Reproduced from Ibachi *et al.*[19].

Moreover, most of III-V semiconductors are direct-band-gap semiconductors, which makes them suitable for light sources. Ternary and quaternary III-V semiconductors further allow for multiple degrees of freedom in the design of III-V integrated devices. This is seen in demonstration in a number of photonic components such as detectors, modulators, interferometers, resonators, filters, couplers and nonlinear optical devices [20], [21]. With this freedom, one can shift the edge of the absorption spectrum as well as wavelength range that is likely to experience multi-photon absorption, essentially reducing the losses due to linear and nonlinear absorption.

Several representatives of the group of III-V semiconductors, for example, Aluminum Gallium Arsenide (AlGaAs) and indium phosphite (InP), have been studied and have shown great potential for photonic integration. Overall, the benefits of this group of materials over other material platforms that have been considered for nonlinear photonic integration are indisputable, however, there is still a major challenge of insufficient data with respect to other materials and compounds in the group regarding their linear and nonlinear optical properties. This is the grand effort of this study – to assess nonlinear and linear optical properties of selected III-V semiconductors, as will be discussed in detail in subsequent chapters.

1.6 Thesis Layout

The introductory chapter includes the motivation of this work, followed by concepts of Photonic Integration, then by a general overview of nonlinear optics and nonlinear optical phenomena. We then motivate our work by explaining the benefits of the material platforms we chose to work with for photonic integration.

In Chapter 2, we present our experiment on linear and nonlinear characterization of AlGaAs waveguides, four-wave mixing of three different geometries in an attempt to answer the question which geometry gives the best results.

Chapter 3 focuses on one of the most important design parameters for waveguides, the refractive index. Specifically, we propose a generalized model for empirically determining the refractive indices of various III-V semiconductors based on the values of their energy gaps.

Chapter 4 focuses on the new material candidates with promising properties for integrated photonics, with specific emphasis on the selection criteria from within the entire group of III-V semiconductors.

The last part of the thesis, Chapter 5, is the summary of this work detailing the conclusions and future outlook for the various projects performed within this Master's work.

Chapter 2

Experimental Demonstration of Four-Wave Mixing in AlGaAs Waveguide

2.1 Introduction

In quest for new and promising material candidates for all-optical devices and integrated optics, AlGaAs (Aluminium Gallium Arsenide) semiconductor, a ternary compound from the III-V group of materials, has received lots of attention in the past two decades. It is one of the most widely studied material compounds for integrated optics, often termed “silicon of nonlinear optics” due to its remarkable nonlinear performance [16], [17], [22]–[24]. Among the material candidates for integrated optics, AlGaAs is singled out by its unique optical properties including, but not limited to, the highest known intensity-dependent refractive index n_2 (Kerr nonlinearity) among other platforms for integrated optics and also very high refractive index thus allowing for tighter mode confinement and more efficient nonlinear interactions. Moreover, some material compositions of $\mathrm{Al}_x\mathrm{Ga}_{1-x}\mathrm{As}$, with $x < 0.45$, have a direct band-gap structure, and thus can allow for a monolithic integration of integrated laser sources, low-loss waveguides and a detector on the same chip without resorting to a hybrid integration with other compounds/elements as in the case of Silicon. Being a ternary compound, AlGaAs has a degree of freedom, the mutual concentrations of Al and Ga in accordance with $\mathrm{Al}_x\mathrm{Ga}_{1-x}\mathrm{As}$, allowing the refractive index and the band-gap energy to be varied and ultimately changing the edge of absorption around the wavelength of interest by changing Al molar concentration x during the epitaxial growth. For example, GaAs has a composition corresponding to

$x = 0$ with the concentration of Aluminium 0%. Setting the concentration of Aluminium to 40%, the concentration of Gallium becomes 60%, making a total of 100% in AlGaAs represented as $Al_{04}Ga_{0.6}As$. Different material compositions of AlGaAs have slightly different optical properties (absorption wavelength edge, refractive index, nonlinear susceptibilities). One can confine light in the layers of AlGaAs with higher refractive index, which is in the basis of waveguide building using this material platform.

2.2 AlGaAs waveguide design

The first step in designing a waveguide based on a ternary or quaternary III-V semiconductor is to identify the composition of the layer stack on the substrate. We define the Al concentration to be 18% ($Al_{0.18}Ga_{0.82}$) for the core for waveguides because it corresponds to minimum two-photon absorption at the wavelength 1550 nm [16].

Keeping in mind that the cladding layer must have a lower refractive index than the core layer, and it must be lattice-matched for low-defect epitaxial growth of the stack, the composition of the cladding layer can be selected as follows. The refractive index of AlGaAs becomes lower as the concentration of Al in the compound goes up [25]. As the result, the claddings should have the concentration of Al greater than 18%. On the other hand, Aluminium is known to oxidize quickly when its concentration exceeds 70% and hence, the choice of the concentration of the cladding is then limited to values greater than 18% but less than 70% of Aluminium.

As stated earlier, another important consideration is to ensure that the layered arrangement is lattice-matched so that the layers of AlGaAs can be epitaxially grown on top of each other without significant defects. The beauty of using AlGaAs for integrated photonics is that AlAs and GaAs have very similar lattice constants, 5.66139 Å and 5.65330 Å, respectively [26], [27].

The lattice is well-matched if the independent constituent binary compounds lie on a nearly vertical line in the bang-dap energy against lattice constant plot, as seen in Fig. 1.18. As could be seen from the graph, AlAs and GaAs lie on a nearly vertical line, hence we have a good matching for all values of x from 0 to 1 inclusive. Also, on this basis, the substrate is selected, which, in this case, the semiconductor industry standard substrate GaAs. With these selections, a 2D waveguide structure could be designed.

2.2.1 Designing Waveguide Geometry

The waveguide structure is a three-layered structure formed by two cladding layers and the guiding layer (core) in the middle, all grown on a GaAs substrate. This arrangement has been shown to provide 1D light confinement in the guiding layer. In order to define a channel where light can be confined in two dimensions, vertical and lateral, it is necessary to implement nanofabrication to make ridges where the light can get confined. In this section, a detailed overview of the geometrical design considerations is presented.

Figs. 2.1(a), 2.2(a) 2.3(a) shows the parameters to be optimized for all three studied geometries, the strip-loaded, nanowire and the half-core. This work was done by K. Awan, a Doctoral student in our research group as part of his doctoral studies. A more complete simulation result and design description is given in his doctoral dissertation [28]. The effect of these variables were understood by performing simulations, sweeping one variable at a time and keeping the other parameters constant. The simulations were done using a commercial mode solver *Lumerical MODE Solutions*.

Using the dispersion model by Gehrsitz *et al.* [25], it is seen that AlAs will give the highest refractive index contrast between the code and the cladding layers for best mode confinement, but also to be on the safe side, the maximum aluminium concentration in the designs were limited to 65% to avoid rapid oxidation as mentioned earlier. The next step in the design process is to examine the changes in the effective mode area A_{eff} with respect to the changes in the thickness of the upper cladding, core layer, lower cladding, the width and the depth of the etching depth, as shown in Figs. 2.1(a), 2.2(a), while still maintaining a single-mode operation for the wavelength range of interest. The effective mode area A_{eff} is defined as

$$A_{\text{eff}} = \frac{\left[\int_{-\infty}^{\infty}\int_{-\infty}^{\infty} \mid E(x,y) \mid^2 \mathrm{d}x\mathrm{d}y\right]^2}{\int_{-\infty}^{\infty}\int_{-\infty}^{\infty} \mid E(x,y) \mid^4 \mathrm{d}x\mathrm{d}y}, \tag{2.1}$$

where $E(x,y)$ is the electric field amplitude. As these waveguides are heterostructures, the next sections deals with details of the parameters considered during the design phase of the waveguides.

For strip waveguides, there have been two previously studied waveguide geometries, the strip-loaded and the nanowire [11], [29]. The strip-loaded geometry has the advantage of very low propagation loss resulting from fully burying the core region underneath the upper cladding. However, it also has high material dispersion as the mode is fully confined within the material [11].

Nanowires have ultra compact mode confinement and dispersion management due to high waveguide dispersion capable of overcompensating for the material dispersion. However, one drawback with this geometry is that is has high propagation losses as the guided mode is largely exposed to sidewall roughness induced during fabrication [11], [28], [29].

A new type of AlGaAs waveguide geometry is proposed, the half-core-etched geometry as a compromise between the two limiting cases, where we have a relatively compact mode, but low propagation loss. The concept of this geometry was tailored to exhibit better potential for nonlinear optics, which we confirm by our studies, in part, at least.
The next subsections detail the design parameterization as performed by K. Awan [28].

Strip-loaded optimization

To start, using Fig. 2.1(a), the effect of the thickness of the upper cladding that will not be etched away (*lip*) is examined. It was seen that the mode area decreased with decrease in the *lip* size. However, if the upper cladding is completely etched away, there will be an increase in the propagation loss in the waveguide. Hence, a practically achievable *lip* size of 100 nm was chosen. Next, the core thickness was examined. Intuitively, it is known that the smaller the waveguide core is, the more confined the mode is (lower A_{eff}). But if the core thickness is too small, it results in loss of guidance. Therefore, to achieve a minimum possible core thickness without losing guidance, the refractive index contrast between the core and the cladding has to be maximized. Here the thickness was restricted to 400 nm because going beyond that thickness results in a mode cut-off for a 2 μm wavelength. For the thickness of the lower cladding, it was observed that, while it had no effect on the mode area, the concentration of the Al in the layer affected the mode area drastically. Also, if the layer is too thin, then the guided mode may leak into the substrate which has a higher refractive index than the core as it is GaAs material. Hence, 3 μm was selected for the core thickness to ensure the guided modes are not leaking into the substrate, and the highest safe concentration of 65% of Aluminium was selected.
For the upper cladding, it is not only important to select the thickness of the

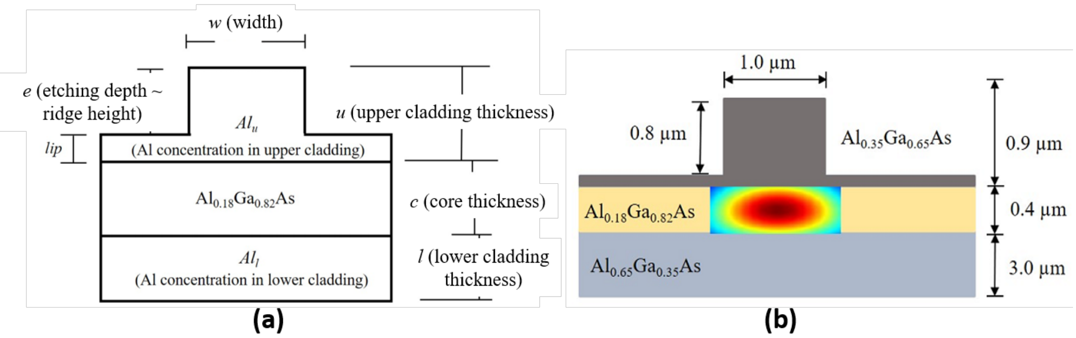

FIGURE 2.1: Schematic diagram showing (a) waveguide variables to be optimized and (b) optimized parameter for AlGaAs strip-loaded waveguide, reproduced from K. Awan [28].

layer, but also the concentration of Aluminium. Lowering the Al concentration of the upper cladding and making it closer to the concentration of the core shifts the mode into the upper cladding. Hence, to achieve smallest mode area, the concentration would have to be adjusted to be more than that of the core and also providing a sufficient refractive index contrast between the upper cladding and the core layer. Simulation results showed that the mode stayed confined in the guiding layer for Aluminium concentrations higher than 30%. An optimized Al concentration of 35% for a cladding thickness of 400 nm was selected. Finally, the effect of the waveguide width for both fundamental TM and TE mode is examined and simulation results showed that the effective mode area is at minimum for the width around 1 μm. The ultimately designed waveguide has an effective mode area of around 1.1 μm^2 for both the fundamental TE and TM modes at the wavelength of 1.55 μm.

Nanowire optimization

As with the strip-loaded waveguide, the aluminium concentration in the core and in both the upper and lower claddings were set to 18% and 65%, respectively, to realise a practically achievable maximum refractive index contrast for stronger modal confinement. As seen in Fig. 2.2(a), the nanowire waveguides have ultra-compact dimensions. These dimension are achievable by etching the core deep into the lower cladding, thereby exposing the core sidewalls to the surrounding medium with a lower refractive index, in this case, air. As with the strip-loaded waveguide, we start parameterization by determining the thickness of the core as it relates to the effective mode area. Simulation results showed best confinement for thickness between 500 nm and 700 nm.

Similarly, the effect of the thickness of the upper cladding was examined, and just as expected as in the case of the strip-loaded waveguide, reducing the thickness of the upper cladding reduced the effective mode area. In the case of no upper cladding, we have a higher refractive index contrast since the top cladding is exposed to air, but for ease of coupling and achieving mode symmetry. Hence, 0.4 μm is chosen as it provides the mode symmetry and also reduced complications in the fabrication process. The effect of the etch depth into the lower cladding was examined and was observed that as we etch deeper into the lower cladding, the effective mode area is reduced, but this effect becomes saturated around 0.8 μm. Etching deeper into the lower cladding becomes practically more difficult from the fabrication standpoint with an increase in the etch depth. The simulation sweep showed good modal confinement at 0.4 μm making an overall etching depth from the top of the wafer to the point where the etching stops to be 1.4 μm. The waveguide of the width 0.5 μm has an effective mode area of around 0.5 μm^2 for both the fundamental TE and TM modes at the wavelength of 1.55 μm.

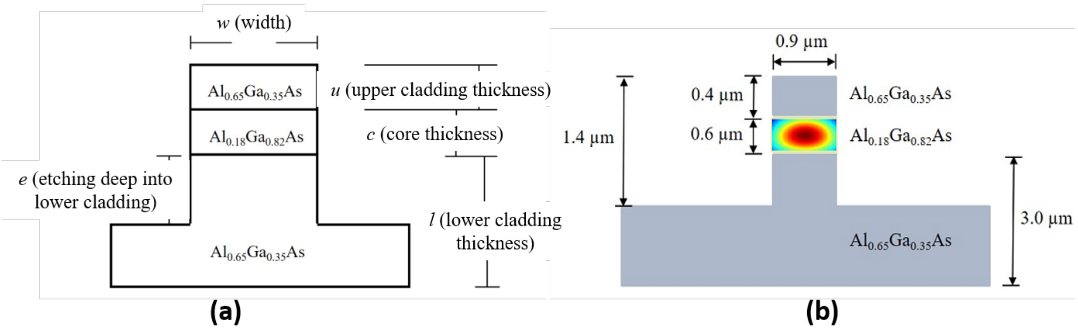

FIGURE 2.2: Schematic diagram showing the (a) waveguide variables to be optimized (b) optimized parameter for AlGaAs nanowire waveguide, reproduced from K. Awan [28].

Half-core optimization

The half-core waveguide, as seen in Fig. 2.3(a), is designed to combine the advantages of both the strip-loaded and the nanowire waveguides. It provides a good confinement, relatively small effective mode area while exhibiting reasonably low propagation losses. The structure is designed by etching half of the core layer (hence the name half-core) which improves the the modal confinement as compared to the strip-loaded waveguide, and the area which is exposed to the roughness due to fabrication is smaller than that of the nanowire waveguide. Again, as with the strip-loaded waveguide, the Aluminium concentration in the core and in both upper and lower claddings were set to 18% and 65%, respectively, to realise a practically achievable maximum refractive index contrast. The thickness of the top cladding was set to

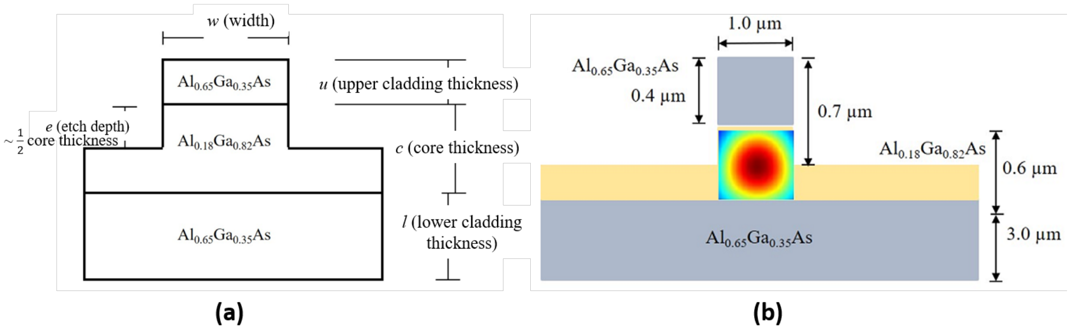

FIGURE 2.3: Schematic diagram showing the (a) waveguide variables to be optimized (b) optimized parameter for AlGaAs Half-core waveguide, reproduced from K. Awan [28].

0.4 μm for same reason as in the nanowire. The thickness of the core was set to 0.6 μm as thickness smaller than this would result in loss of guidance for wavelengths up to 2 μm, and larger than this would result in rapid expansion of the effective mode area. The etch depth was set to half the thickness of the core as per geometric design requirement to reduce the sidewall roughness. Finally, the width was fixed to 1.0 μm, which provides lowest effective mode area while still maintaining guidance for wavelength up to 2 μm. The waveguide has an effective mode area of around 0.75 μm^2 for both the fundamental TE and TM modes at the wavelength of 1.55 μm.

Clearly, the dimensions of this geometry are smaller than that of the strip-loaded ($A_{eff} = 1.1\mu m^2$) and slightly larger than that of the nanowire ($A_{eff} = 0.5\mu m^2$).

2.2.2 AlGaAs Waveguide layout

All three waveguide geometries had the sample layout as described below. This layout is represented schematically in Fig. 2.4. To simplify the coupling process in and out of the waveguide, the 2-μm-wide multimode coupling waveguides were defined at the input and output of the devices. The coupling waveguides were tapered down to the width of the actual waveguide, as designed and described in the previous subsections. The tapers are shown in Fig. 2.4 as waveguide sections with varying widths. The width of the nanosection ranges from 0.9 μm to 1.2 μm, 0.6 μm to 1.1 μm, and 0.8 μm to

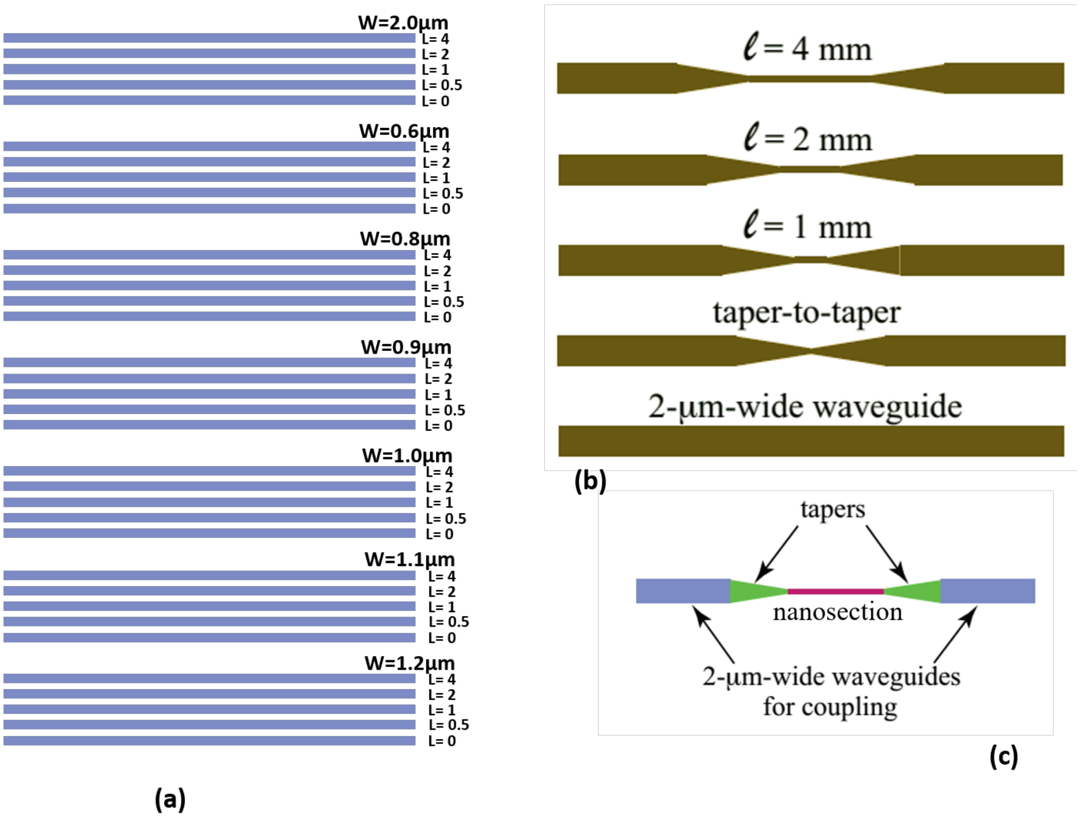

FIGURE 2.4: Schematic showing the waveguide layout for each geometry, reproduced from K. Dolgaleva *et al.* [11].

1.1 μm for the strip-loaded, nanowire and half-core respectively with a 100 nm step and the nanosection lengths were 4 mm, 2 mm, 1 mm, 0.5 mm and 0 mm which was the taper-to-taper, as seen in Figs. 2.4(a), (b). The entire sample containing all the devices was 5.26 mm for the strip-loaded, 5.33 mm for the nanowire and 5.87 mm for the Half-core, as measured with a micrometer screw gauge. The "taper-to-taper" and the reference (2 μm) waveguide were, first of all, used for the propagation loss measurement to estimate the linear propagation losses of the narrow waveguide sections. They were also used to experimentally determine the contribution of the coupling waveguides sections to the FWM signal to find out how much did the actual narrow waveguides contribute to the overall FWM signal.

2.3 Linear Characterization

Here we describe the measurement of the linear propagation losses of the waveguides. The waveguides can be viewed as a Fabry-Parot cavity for the light that is propagating back and forth and then getting reflected at each waveguide facet interface with air, hence, the Fabry-Parot method of loss calculation was used. In this method, the total loss in the waveguide is computed as a sum of the propagation loss Λ_{prop}, the coupling loss resulting from the mode size and shape mismatch between the focused laser beam in free space and the waveguide mode, Λ_{coupl}, and, lastly, the Fresnel reflection loss Λ_{ref},

$$\Lambda_{\text{total}} = \Lambda_{\text{coupl}} + 2\Lambda_{\text{ref}} + \Lambda_{\text{prop}} \times l, \tag{2.2}$$

where l is the overall length of the waveguide.
As mentioned earlier, the length of the waveguide was measured to be 5.25 mm for the strip-loaded, 5.87 mm for the nanowires, and 5.87 mm for the half-core geometries.

2.3.1 Linear Characterization Experimental Setup

A tunable cw semiconductor laser, Santec TSL 710, was used as the light source for the Fabry-Perot loss measurement within the wavelength range around 1550 nm. The light from the laser source was coupled into a single-mode SMF28 fiber, and then was collimated for free-space coupling into the waveguides. The collimated beam was then polarized horizontally or vertically (TE or TM polarizations) using a half-wave plate and a polarizing beam splitter cube. After this, the polarized light was butt-coupled into the waveguide using a 40× microscopic objective mounted on a 3-axis micrometer coupling stage. The light was then coupled out of the waveguide with a 20× microscopic objective. An IR photodetector was used to measure the optical power at the output of the waveguide. The measurement was performed as a function of wavelength. Lastly, the Fabry-Perot loss analysis was performed for each studied waveguide of each geometry.

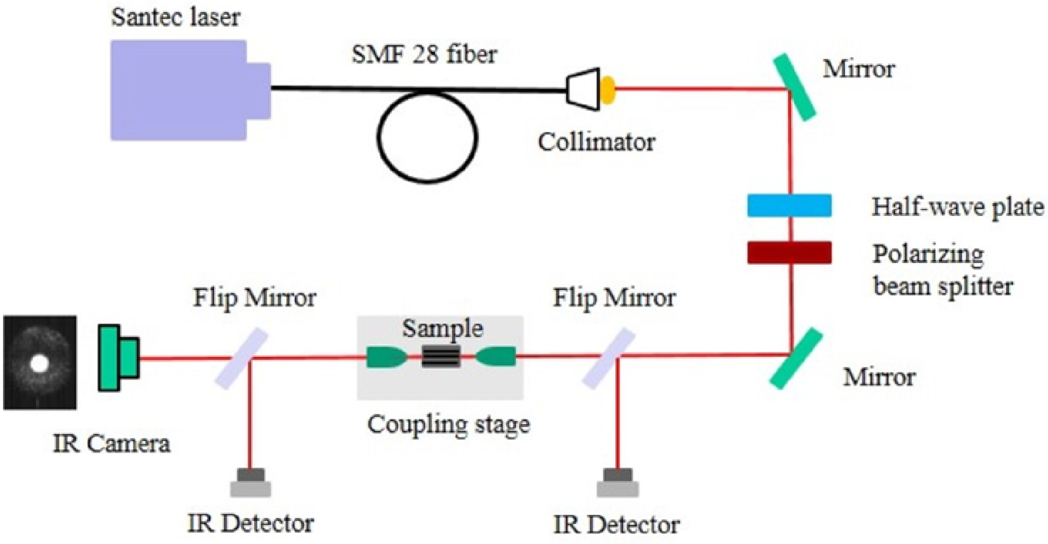

FIGURE 2.5: Schematic of the setup for linear optical characterization using Fabry-Perot Method, Adapted from K. Awan [28].

2.3.2 Propagation Losses

The first step in the loss measurement is to estimate the total loss (Λ_{Tot}) of the waveguide. To determine this, the power at the input of the waveguide (P_{in}) is compared to the power at the output to the waveguide ($\mathrm{P}_{\mathrm{out}}$),

$$\Lambda_{\mathrm{tot}} = 10\log_{10}\frac{P_{\mathrm{out}}}{P_{\mathrm{in}}}. \tag{2.3}$$

To compute the propagation loss coefficient of the 2 μm-wide coupling waveguide (α), we used a 2 μm-wide reference waveguide [see Fig. 2.4 (b)] with length l. For waveguides of constant width, the propagation loss coefficient is related to the waveguide length by the following equation:

$$\alpha = \frac{1}{l}\ln\left(\frac{1-\sqrt{1-K^2}}{RK}\right). \tag{2.4}$$

It is also possible to calculate the propagation loss in dB/cm as

$$\alpha\,[\mathrm{dB/cm}] \approx 4.34\alpha[\mathrm{cm}^{-1}], \tag{2.5}$$

where R is the facet reflectivity (R) defined as

$$R = \left(\frac{n_{\mathrm{eff}} - 1}{n_{\mathrm{eff}} + 1}\right)^2, \tag{2.6}$$

and K is the ratio of the minimum-to-maximum transmission power (peak-to-peak transmission coefficient), given by

$$K = \frac{T_{\mathrm{max}} - T_{\mathrm{min}}}{T_{\mathrm{max}} + T_{\mathrm{min}}}. \tag{2.7}$$

From those, one can find the effective refractive index of the guided mode using the relationship for the Fresnel coefficient in the form

$$\Delta\lambda = \frac{\lambda^2}{2n_{\mathrm{eff}}l}. \tag{2.8}$$

The maximum (T_{max} and minimum (T_{min} transmissions were experimentally determined using the setup in Fig. 2.5 and then substituted into eq. (2.4) to obtain α. Then we considered that the propagation loss coefficients of the 2 μm-wide coupling part and the 2 μm-wide reference (straight) waveguide are the same.

2.3.3 Coupling Losses

The next step is to measure the losses resulting from coupling the light beam into the waveguide (Λ_{coupl}). This loss is expressed as

$$\Lambda_{\mathrm{coupl}} = \Lambda_{\mathrm{tot}} - l \times \alpha[\mathrm{dB/cm}] \tag{2.9}$$

where l is the length of the sample and Λ_{tot} is the total loss.

2.3.4 Taper Loss

The waveguides with nanosection part requires also the calculation of the taper loss and the nanosection propagation loss. To estimate the losses produced by the tapers (Λ_{tap}, we used the taper-to-taper waveguide [see Fig. 2.4(b)]. The taper length is l_{tap} = 0.2 mm per taper for all waveguides. The taper loss is obtained for waveguides of different nanosection widths using the following expression:

$$\Lambda_{\text{tap}} = \Lambda_{\text{tot}} - \left(l - 2l_{\text{tap}}\right) \times \alpha[\text{dB/cm}] - \Lambda_{\text{coupl}}, \tag{2.10}$$

where l is the total length.

2.3.5 Nanosection Loss

Now, the actual losses in the nanosections can be calculated once all these values are obtained. The loss in the narrow section of the waveguides are determined using the following expression:

$$\Lambda_{\text{NS}} = \Lambda_{\text{tot}} - (l - 2l_{\text{tap}} - l_{\text{NS}}) \times \alpha[\text{dB/cm}] - \Lambda_{\text{coupl}} - \Lambda_{\text{tap}}, \tag{2.11}$$

where l_{NS} is the length of the nanosection part only. The nanosection loss in dB/cm is achieved by $\Lambda_{\text{NS}}/l_{\text{NS}}$.

TABLE 2.1: Table showing the linear losses for Nanowire, Strip-loaded and Half-core waveguide.

	Strip Loaded		**Nanowire**		**Half-Core**	
	TM (dB)	**TE (dB)**	**TM (dB)**	**TE (dB)**	**TM (dB)**	**TE (dB)**
Coupling Loss	5.5638	4.3059	9.9891 10.5**	8.9959 9.8**	7.0824	6.9329
	TM (dB/cm)	**TE (dB/cm)**	**TM (dB/cm)**	**TE (dB/cm)**	**TM (dB/cm)**	**TE (dB/cm)**
Propagation Loss*	2.6602	3.0616	5.1821 5.7**	3.4684 3.2**	5.21	3.8044
Taper Loss						
NS Width (μm)	**TM (dB)**	**TE (dB)**	**TM (dB)**	**TE (dB)**	**TM (dB)**	**TE (dB)**
0.6	-	-	-		0.9	0.7
0.7	-	-	5.7	0.1	0.2	0.7
0.8	-	-	1.0	0.9	1.0	0.7
0.9	0.1	1.1	0.1 2.4**	1.0 2.2**	1.2	0.5
1	2.5	1.0	0.1	1.0	-	-
1.1	1.5	0.6	-	-	-	-
1.2	0.6	1.8	-	-	-	-
Average (dB)	1.2	1.1	1.7	0.8	0.8	0.7
NanoSection Loss						
NS Width (μm)	**TM (dB/mm)**	**TE (dB/mm)**	**TM (dB/mm)**	**TE (dB/mm)**	**TM (dB/mm)**	**TE (dB/mm)**
0.6	-	-	-	-	0.4	0.5
0.7	-	-	1.1	-	0.5	0.1
0.8	-	-	0.8	0.6	0.7	0.2
0.9	0.5	0.1	1.0 2.5**	1.5 1.8**	0.5	0.2
1	0.1	0.1	1.7	0.7	-	-
1.1	0.6	0.2	-	-	-	-
1.2	0.4	0.6	-	-	-	-
Average (dB/mm)	0.4	0.3	1.1	0.9	0.5	0.2

* Propagation loss of the 2μm wide coupling waveguide
** Remeasured by myself confirming initial measurements

Using eqs. (2.2 – 2.11), the losses were obtained and summarized in table 2.1 for the three waveguide geometries.

Most of the data presented in table 2.1 was already obtained before this thesis work by David Sanchez, a summer student in our research group. I repeated some measurements for the nanowire waveguide to confirm his method and to learn how to perform the linear characterization. The new values (in bold font in the table) are fairly in agreement with the previous one.

2.4 Nonlinear Characterization

2.4.1 Four-wave mixing experimental setup

The schematic of the experimental setup used for the four-wave mixing experiment is shown in Fig. 2.6. In this setup, Coherent optical parametric oscillator (OPO) was used as the FWM pump source. This OPO is pumped by a Ti:Sapphire laser (model Mira, from Coherenc inc.), operating at 800 nm, with an output power up to 600 mW at a wavelength range between 1000 nm and 1600 nm. The optical pulses originating from the OPO had 3-ps FWHM temporal duration and followed at the repetition rate 76.6 MHz. A JDSU tuneable cw laser was used as the FWM signal source, amplified by an Amonics erbium-doped fibre amplifier (EDFA) to the power level up to 2 W. The tunability of signal beam was constrained by the operational range of the EDFA which is capable of amplifying the radiation at wavelengths between 1535 nm and 1565 nm. Both the cw laser and EDFA were fibre-coupled. The

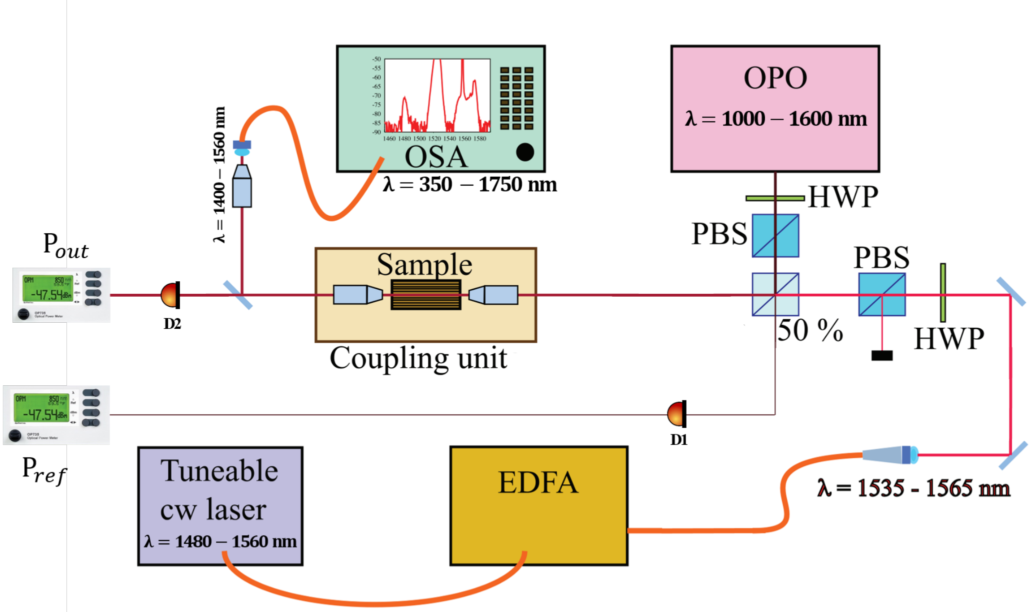

FIGURE 2.6: Schematic diagram showing the four-wave mixing setup, reproduced from K. Dolgaleva *et al.* [29].

radiation coming from EDFA was decoupled from the fibre to free space with a collimator and combined with the pump radiation using a non-polarizing 50% beam splitter (marked "50%" in Fig. 2.6). The polarization of both beams were set independently by a pair of a polarizing beam splitter (PBS) and a half-wave plate (HWP), placed in the corresponding arm. After combining both beams, the pump and signal beams were both coupled simultaneously into the integrated optical devices placed into a micro-positioning coupling stage. This micro-positioning coupling state had two objectives lenses of 6.24 mm focal length which were used for coupling the light into and out from a particular waveguide on the chip. The power at the input was measured with the photodetector in the sample position (without the sample) and was confirmed to be approximately the same of the reference photodetector (labelled as $\mathrm{P}_{\mathrm{ref}}$ in the figure). When the sample was on the stage, the reference power was used to monitor and control the input power. The total output power (integrated in wavelength) was measured by the photodetector labelled as $\mathrm{P}_{\mathrm{out}}$. We controlled the input signal or pump power manually rotating their respective half-wave plate (HWP). The output spectra from the waveguides were measured using an optical spectrum analyzer (OSA) model AQ6315E from Ando Inc.

2.4.2 Four-Wave Mixing Experiment

We first investigated the strip-loaded waveguides sample (as it is a more traditional geometry posing less challenges in handling). The first step in the experiment was to set the polarization of both the beams to either TE or TM by setting the polarizers (labelled "PBS" in Fig. 2.6) and half-wave plates (HWPs) to transmit a beam with either horizontal or vertical polarization for both the beams independently. The strip-loaded waveguide was placed on the mount and we coupled the light into the reference waveguide (see Fig. 2.4). The process of coupling the light into the waveguide involved aligning the pump beam and the signal beam in an attempt to maximally couple them into the selected waveguide on the sample The coupling in at the input to the sample and coupling out at the output of the sample was varied first by using an IR-sensitive CCD camera for observing the waveguide mode profile, and then by maximizing the reading of the output detector (labelled "P_{out}" in Fig. 2.6) until a perfectly aligned beam is obtained with maximum output power. To select the reference waveguide for coupling, we used a CMOS camera (DCC1545M, from Thorlabs) to view the layout of the devices from the top while adjusting the mounting position of the sample on the stage. The output of the waveguides was then fibre-coupled into the optical spectrum analyzer (labelled "OSA" in Fig. 2.6) via a flip mirror allowing to select between the detector and the OSA. Fig. 2.8 shows a typical result obtained with a 0.6-μm-wide nanowire of length 2 mm when the pump wavelength was set at 1510 nm. This figure and all other FWM plots present the best spectra output for simplicity. In this plot, the spectra of the pump, the generated idler and the corresponding signal wavelengths are placed on the same plot and labelled accordingly. The peaks at shorter wavelength region represent the generated idler, at the set pump (middle peak) and the signal (longer wavelength region). The pedestal around the signal peaks indicates the unfiltered amplified spontaneous emission from the EDFA.

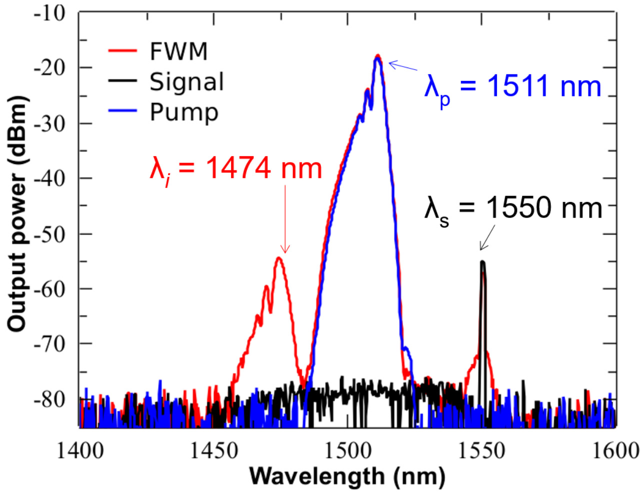

FIGURE 2.7: FWM spectra for a nanowire with 0.6 μm width and length of 2 mm, TE mode

It was observed that the TE-polarized signal and pump FWM spectra exhibited a significantly higher FWM conversion and higher generated idler output power than the TM-polarized signal and pump FWM spectra, as seen in Fig. 2.8. Thus, we chose to perform the rest of our studies for the TE ploarization only.

Another factor in determining optimal experimental conditions was the input power. From the previous study by K. Dolgaleva, *et al.* [29], we know that increasing the pump power above a certain threshold yielded no better results with respect to the generated idler power. By varying the pump power while keeping the signal power constant, we found the optimal input pump power to be around 46 mW. as measured from the reference power meter just before entering the waveguide. Though the input pump power did

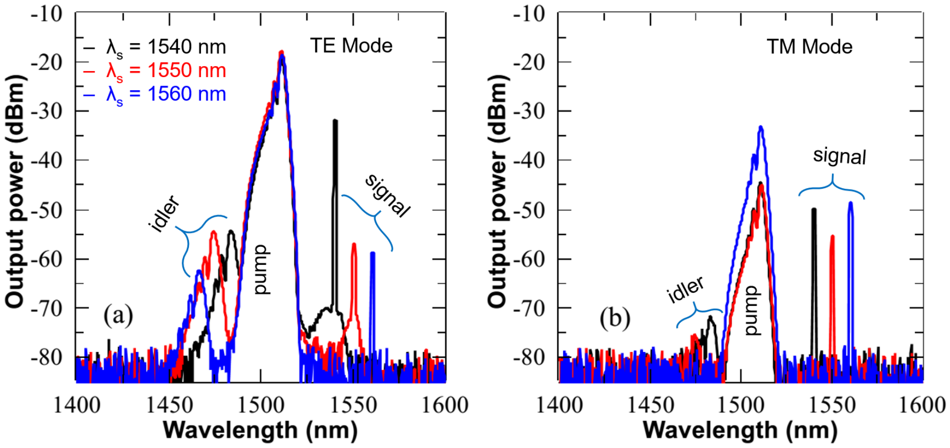

FIGURE 2.8: FWM spectra for nanowire, $w = 0.6\ \mu$m, $l = 2$ mm for TE and TM modes at $\lambda_s = 1540$ nm, 1550 nm and 1560 nm with $\lambda_p = 1510$ nm

not have noticeable effect on the generated idler power, very high pump and signal power would broaden the pump, signal and the idler spectra due to self-phase modulation (SPM) and cross-phase modulation (XPM) nonlinear effects which would in effect degrade the efficiency of the FWM [29]. Aside from the broadening of the waveforms, increased input pump and signal power essentially contributes to the total power input into the waveguide, effectively increasing the generated heat which could damage the waveguide.

In like manner, by varying the signal power while keeping the pump power constant, the optimal signal power was chosen to be 200 mW, measured from the reference power meter.

The pump wavelength was chosen to give relatively long wavelength gaps between the pump, signal, and consequently, the generated idler. This is done to avoid spectral overlap of the adjacent wavelengths. The idler wavelength is determined using the relation

$$\lambda_i = \left(\frac{2}{\lambda_p} - \frac{1}{\lambda_s}\right)^{-1}. \tag{2.12}$$

Fig. 2.8 shows the FWM mixing spectra for the nanowire, the strip-loaded and the half-core waveguides at $\lambda_s = 1540$ nm, 1550 nm and 1560 nm, with the pump wavelength at 1510 nm. From these spectra, we compute the efficiency of the FWM conversion for the nanowire, the strip-loaded and the half-core waveguide geometries. In order to provide a base of comparison with other reported results, we adopted two separate ways of estimating the conversion efficiencies of the FWM process. The first method, given by eq.(2.13) below gives the average conversion efficiency.

$$\eta = \mathrm{P}_{\mathrm{i}}^{\mathrm{dBm}} - \mathrm{P}_{\mathrm{s}}^{\mathrm{dBm}}. \tag{2.13}$$

Here $\mathrm{P}_{\mathrm{i}}^{\mathrm{dBm}}$ is the average idler power and $\mathrm{P}_{\mathrm{s}}^{\mathrm{dBm}}$ is the signal power measured by the reference power meter. The average idler power was the value measured at the output of the waveguide by the OSA, and adding 5.7 dB, to take into account the fibre coupling loss in the OSA.

The second method, described by eq.(2.13) gives the peak conversion efficiency

$$< \eta >=< \mathrm{P}_{\mathrm{i}}^{\mathrm{dBm}} > -\mathrm{P}_{\mathrm{s}}^{\mathrm{dBm}}, \tag{2.14}$$

where $<\mathrm{P}_{\mathrm{i}}^{\mathrm{dBm}}>$ is the peak idler power and $\mathrm{P}_{\mathrm{s}}^{\mathrm{dBm}}$ is the signal power measured by the reference power meter.

The peak idler power was calculated as

$$\begin{gathered} < P_i >= \frac{P_i}{\tau f_p}, \\ \tau = 3\text{ps},\ f_p = 76.6\ \text{MHz}, \end{gathered} \tag{2.15}$$

where τ is the pulse width and f_p pulse repetition rate of the OPO.

The signal power incident on the waveguide was around 200 mW, as measured by the reference power meter. Taking into account the coupling loss of 9.3 dB, the overall signal input power P_{s} (at the entrance to the waveguide) was then estimated to be 23.5 mW.

The average pump power was calculated as follows: pump power incident on the waveguide was $<P_{\mathrm{p}}>$ = 46 mW, as measured with the reference power meter.Considering the coupling loss of 9.3 dB, the pump input power (at the entrance of the waveguide) was estimated to be 5.4 mW The peak pump power at the peak wavelength was therefore $\mathrm{P}_{\mathrm{p}} = < \mathrm{P}_p > / \left(\tau f_p\right) = 3.8$ W.

The next question that we tried to answer was how the width of the waveguide contributed to the overall FWM conversion. To do this, we first chose the pump and signal wavelengths with the highest efficiency from previously collected data. Using the sample length of 1 mm, pump at 1520 nm and signal at 1550 nm, we did a sweep of all waveguide widths in each sample.
Fig. 2.9 shows the FWM conversion efficiency plotted against the waveguide width for the Half-core waveguide. From this graph, one could conclude that

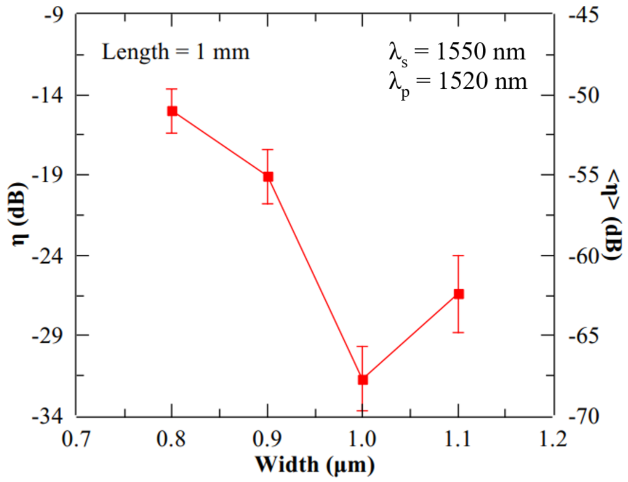

FIGURE 2.9: FWM conversion efficiency as a function of the waveguide width for the half-core waveguide with the length of 1 mm, the pump wavelength at 1520 nm, and signal wavelength at 1550 nm.

the efficiency decreased with increasing the width of the waveguide. This also confirms the role of the width as it relates to the effective modal area; the smaller the effective modal area, the better the mode confinement, and, with the optimal experimental conditions, the efficiency of the FWM is expected to be higher.

However, this graph also shows a v-shaped curve as it moves between widths of 1.0 μm and 1.1 μm. This characteristic is does not confirm with any known phenomenon. Having examined this carefully by repeating the measurement using different waveguides the same width on the same chip, this deep still persists. Therefore, the presence of this deep as we progress in width could only be explained to be as a result of a probable fabrication defect within the waveguide of width 1.1 μm.

The efficiency of the FWM conversion could also be influenced by the length of the waveguide since the propagation loss in many of our devices as measured was very high. Hence, there is also need to experimentally determine how the length of the waveguide contributes to the efficiency of the FWM conversion. It is seen from Fig. 2.9 that the efficiency of the FWM is higher for waveguides with smaller widths. To this effect, we use the waveguide with the smallest width which is 0.8 μm. By fixing the width of the waveguide at 0.8 μm, the effect of the waveguide length (length of the nanosection) with respect to the FWM efficiency was examined.

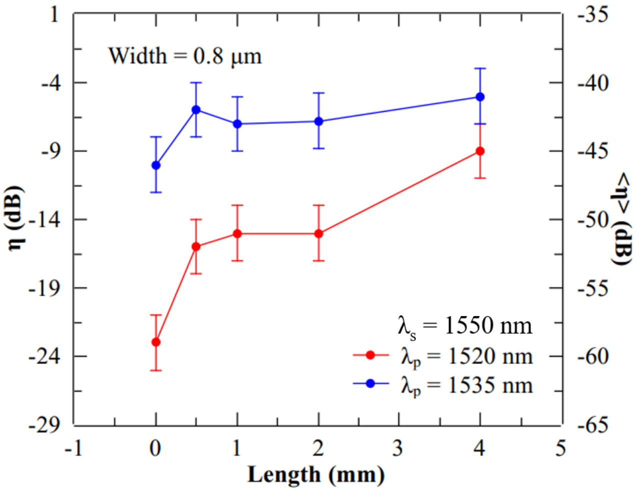

FIGURE 2.10: FWM conversion efficiency as a function of the waveguide length, with the width set to 0.8 μm, the pump wavelength at 1535 nm and 1520 nm, and signal wavelength at 1550 nm for the half-core waveguide

.

Fig. 2.10 shows the FWM conversion efficiency plotted against the waveguide length for a half-core waveguide, using the best width from the sweep, the pump wavelengths at 1535 nm and 1520 nm, and the signal wavelength at 1550 nm. It can be seen that there is an increase in the FWM efficiency as we increase the length of the waveguide. This is expected as the longer the length is, the greater is the nonlinear interaction length. This, however, would incur some undesired effects as increasing the length also means increase the linear propagation loss in the waveguide. The sample with the lengths of 1 mm and 2 mm showed no difference or a negligible difference in the conversion efficiency when taking into account the experimental error, as marked in Fig. 2.10. Also, depending on the geometry, only a few of the lengths of these waveguides were in good condition (not broken or damaged) to guide light. Hence, we chose the 1-mm-long device of the Strip-loaded and Half-core geometries and the 2-mm-long device of the nanowire geometry to perform the next part of the experiment where we compare the three geometries in terms of their FWM performances.

After determining the optimal experimental and sample conditions, a detailed comparative study of the FWM in the waveguides of the three geometries at different pump and signal wavelengths was performed. The tuneability range in this experiment was constrained by the operational range of our instrumentation. The shortest wavelength was 1400 nm which was from the fibre coupling from the output of the sample on the stage to the OSA

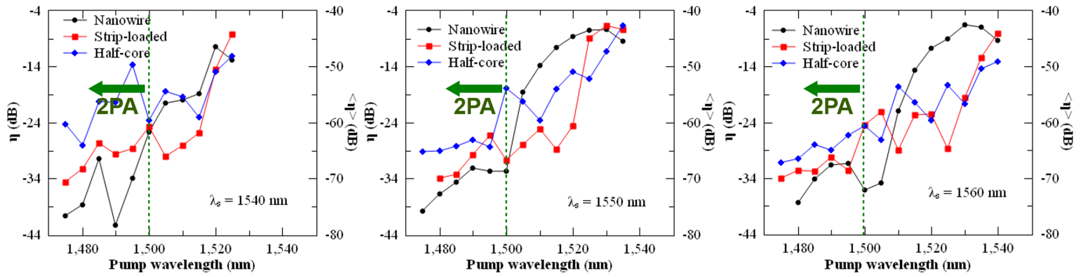

FIGURE 2.11: FWM spectra for the nanowire (w = 0.6 μm, l = 2 mm), strip-loaded (w = 0.9 μm, l = 1 mm) and the half-core waveguide (w = 0.8 μ m, l = 1 mm) in TE mode with the pump wavelengths spanning the range between 1475 nm and 1540 nm with 5-nm step and signal wavelength (a) 1540 nm, (b) 1550 nm and (c) 1560 nm, indicating the nonlinear absorption region around 1500 nm.

and on the longer wavelength range, the EDFA has operation range between 1535 nm and 1565 nm which set the upper limit on our pump source's wavelength.

Fig. 2.11 shows the FWM conversion efficiency as a function of the pump wavelength with the signal wavelength varied between 1540 nm and 1560 nm with a 10 nm step, with each plot showing the FWM conversion efficiency of the nanowire, strip-loaded and the half-core for a single signal wavelength and pump wavelengths varying between 1475 nm to 1540 nm with a 5-nm step. Looking at the graphs, one can see the following trend in the conversion efficiency characteristics. The conversion efficiency is higher at the longer wavelengths for all three kind of geometries, and lower for shorter wavelengths. This trend is especially pronounced in the nanowires. We believe that the reason to this behaviour lies in the onset of the nonlinear absorption, as we describe it below.

Based on the values of the energy gap of AlGaAs of different compositions, available in Gehrsitz *et al.* [25], for our compound with the Aluminium concentration in our guiding layer being 18%, the linear absorption is expected to occur at $\lambda \leq 750$ nm, two-photon absorption is expected to occur fort the wavelength 750 nm $\leq \lambda \leq$ 1500 nm, and the onset of three-photon absorption occurs at the wavelength 1500 nm $\leq \lambda \leq$ 2250 nm. That is why, we can observe in Fig. 2.11 that, in the region were two-photon absorption is not expected, the nanowire geometry shows the best conversion efficiencies, followed by the half-core and then strip-loaded geometries. In the region with 2PA, on the other hand, the half-core waveguide is the most efficient device, followed by the strip-loaded and then nanowire waveguides. The fact that the nanowire exhibits the strongest light confinement due to its higher refractive index contrast and smaller dimensions has a benefit of demonstrating a higher conversion efficiency in FWM. On the other hand, it also has a drawback of enhancing parasitic nonlinear effects such as nonlinear absorption. That is why, the benefits of the higher FWM efficiency are only attainable for the wavelength range where the nonlinear absorption is negligible. To confirm our intuition, we performed a detailed study of the effect of nonlinear absorption on the performance of our devices.

2.4.3 Nonlinear Absorption

Strong nonlinearities (*e.g.,* Kerr effect) are usually accompanied by some undesired parasitic effects such as nonlinear absorption. With Kerr effect, the nonlinear absorption reduced the power available for phase shifting and changes in refractive index. This essentially decreases the effective Kerr coefficient of the material. If the energy of the photon of light propagating through a semiconductor material is large enough, the electron in the valence band absorbs these photons, thereby acquiring enough energy to transition to the conduction band. The predominant nonlinear loss mechanism depends largely on the electronic structure of the material and also the spectral range of interest with respect to intended design applications. In ternary and quaternary III-V semiconductors compounds, one has good control over this characteristic. As mentioned earlier, the band-gap wavelength of these materials could be adjusted within a range of values by changing the composition of constituent elements in the compound. Changing the composition consequently shifts the edge of the absorption spectrum as well as the potential wavelength that is likely to experience two-photon absorption, thereby minimizing the nonlinear absorption losses. To properly characterize these devices, it is important to measure the strength of the nonlinear absorption in these waveguide structures. At high optical intensities, nonlinear absorption processes get increased significantly, this effect must therefore be examined for every nonlinear optical design.

Multi-photon absorption is an effect directly related to the odd-numbered nonlinearities where two or more photons with a sum of energy equaling the energy gap between the electronic bands of the semiconductor can excite an electron from the from the valence band to the conduction band. By accounting for the third and fifth-order nonlinearity, the total absorption coefficient can be expressed as

$$\alpha = \alpha_0 + \alpha_2 I + \alpha_3 I^2, \tag{2.16}$$

where α_0 is the linear absorption coefficient, α_2 is the third-order nonlinear absorption coefficient related to two-photon absorption (2PA) and α_3 is the fifth-order nonlinear absorption coefficient related to three-photon absorption (3PA). 2PA is the strongest at photon energies close to half of the band-gap energy of the semiconductor material and 3PA is the strongest at the energies close to one-third of the band-gap energy of the semiconductor material.

2.4.4 Absorption experimental setup

The schematic of the experimental setup used for the non-linear absorption experiment is shown in Fig. 2.12. In this setup, Coherent optical parametric oscillator (OPO) was used as the FWM pump source. This OPO is pumped by a Ti:Sapphire laser (model Mira, from Coherenc inc.), operating at 800 nm, with an output power up to 600 mW at a wavelength range between 1000 nm and 1600 nm. The optical pulses originating from the OPO had 3-ps FWHM temporal duration and followed at the repetition rate 76.6 MHz.

The polarization of the beam was set by a polarizing beam splitter (PBS) and a half-wave plate (HWP), placed in the corresponding arm. The beam is now coupled into the integrated optical devices placed into a micro-positioning coupling stage. This micro-positioning coupling state had two objectives lenses of 6.24 mm focal length which were used for coupling the light into and out from a particular waveguide on the chip.

The power at the input was measured with the photodetector in the sample position (without the sample) and was confirmed to be approximately the same of the reference photodetector (labelled as "P_{ref}" in Fig. 2.6). When the sample was on the stage, the reference power was used to monitor and control the input power. The total output power (integrated in wavelength) was measured by the photodetector labelled as "P_{out}". The input power was controlled manually by rotating the half-wave plate (HWP). The output spectra from the waveguides were measured using an optical spectrum analyzer (OSA) model AQ6315E from Ando Inc.

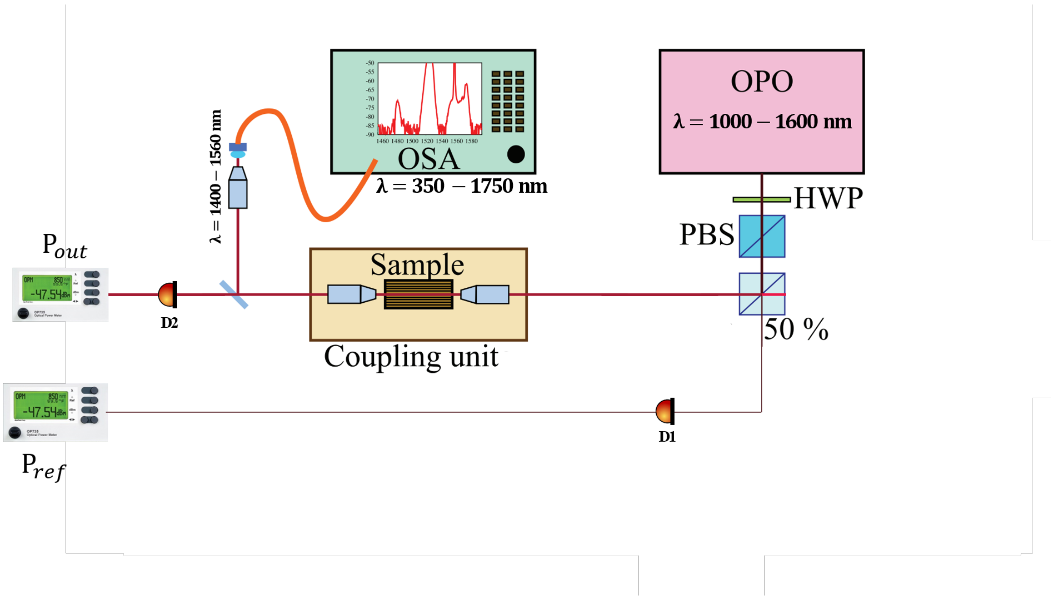

FIGURE 2.12: Schematic diagram for 2PA experimental setup

2.4.5 Two-photon Absorption

Two-photon absorption occurs when the intensities of the light propagating through the semiconductor material is high enough to induce a nonlinear optical interaction and the combined energy of the photons is large enough, such that the electron in the valence band absorbs two photons thereby acquiring enough energy to traverse the energy gap to the conduction band. Two-photon absorption only occurs for photon energies above the half-band-gap level (or less than or twice the wavelength of interacting light of the semiconductor) for both the TE and TM polarization. However, band tail states with lover energies than the band-gap can cause a significant effect in the two-photon absorption below half the band-gap. two-photon absorption causes an increase in the absorption which is directly proportional to the intensity of the optical field. Using eq. 2.16, the rate of change in the loss coefficient is given by

$$\Delta\alpha = \alpha_2 I, \tag{2.17}$$

where α_2 is the 2PA coefficient and I is the intensity of the electric field.

Preliminary result for the absorption coefficient shows that we have higher losses due to 2PA at wavelengths below 1500 nm as seen in Fig. 2.13.

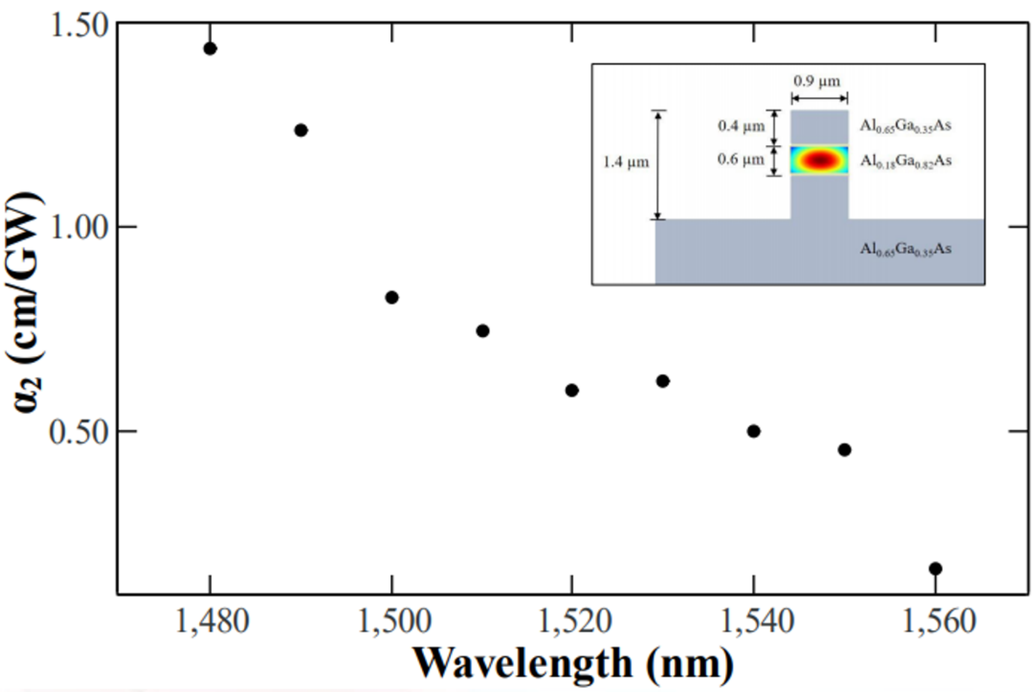

FIGURE 2.13: two-photon absorption for the Nanowire waveguide

2.5 Conclusions

From the results presented in Table 2.1, it can be seen that in terms of propagation losses, the strip-loaded waveguide is the least lossy geometry followed by the nanowire and then the half-core, which present similar losses with the nanowire.

In terms of coupling loss, the losses increase going from the strip-loaded to the Half-Core and to the Nanowires. With the tapers, the losses in the Half-Core results are the lowest, followed by the strip-loaded and then the nanowires being the highest with significantly higher losses.

The results obtained for the nanosections do not really follow the trend we could have expected: low losses for strip-loaded waveguides, high losses for the nanowires with half-core in-between the both. Instead, the values appear to fluctuate with higher values for the nanowire with no predictable trend. Fig. 2.14 shows the summarised results for the FWM in all the devices. The conversion efficiency of the FWM in all the devices decrease below 1500 nm. This decrease is most prominent in the nanowire. One possible reason for this decrease is 2PA, which is expected to occur below 1500 nm. The nanowire waveguide, experiences the strongest two-photon absorption owing to the fact that this geometry has the smallest modal area which results in

Geometry	Conversion Range	Overall Best Efficiency	
		η	<η>
Half-core	161 nm (1560 nm → 1399 nm)	-6.2 dB λs =1550nm, λp=1535nm	-42.7 dB λs =1550nm, λp=1535nm
Nanowire	152 nm (1560 nm → 1408 nm)	-6.3 dB λs =1550nm, λp=1530nm	-42.6 dB λs =1550nm, λp=1530nm
Strip-loaded	161 nm (1560 nm → 1399 nm)	-6.3 dB λs =1550nm, λp=1530nm	-42.7 dB λs =1550nm, λp=1530nm

FIGURE 2.14: Summary of the best efficiencies and conversion ranges device for nanowire, strip-loaded and the half-core waveguides

a stronger light confinement in the device. As a result of this strong confinement, the intensity of the propagating light is much higher, which results in very strong multi-photon absorption as compared to the other waveguides with slightly less modal confinement.

It is a well known fact that the coefficients α_2 and α_3 are material parameters independent of the waveguide geometry. It was, however, observed in our studies that the cumulative effect of the nonlinear absorption depends on the waveguide geometry and is stronger for the waveguides with stronger mode confinement. An additional remark should be made regarding the extracted values of the nonlinear absorption coefficients α_2 and α_3. While they represent material parameters, there is an uncertainty about the material compositions for which these values are obtained. This comes from the fact that only a fraction of the optical field is concentrated in the waveguide core. A significant fraction of the modal area covers the surrounding regions which are the claddings with the material compositions and band-gap energies different from those of the core. It is still true that the most of the optical field is concentrated in the guiding layer. That is why, the values of the measured nonlinear absorption coefficients are primarily dictated by the core's material. Nevertheless, this factor needs to be kept in mind if one needs to perform a more careful study of the nonlinear absorption.

Table 2.14 shows that we are able to achieve with our devices a long conversion range of about 161 nm. The conversion range is defined as the maximum difference between the signal wavelength and the generated idler wavelength, which mathematically can be represented as

$$\lambda_{\text{conv}} = \max(\lambda_s - \lambda_i). \tag{2.18}$$

The peak efficiency of the FWM around the wavelength of interest (1550 nm) is seen to be – 6.2 dB for the half-core waveguide and – 6.3 dB for both the nanowire and the strip-loaded waveguides. Intuitively, without trying to single out the "best" geometry as they are all with negligibly close efficiencies, one could choose the best geometry suitable for the intended application. For instance, designing a device that is more sensitive to 2PA at the operation wavelength range, one could choose the nanowire. Likewise, if the application is less sensitive to 2PA, then half-core shows better results with a longer conversion range of 161 nm, thereby trading off the 2PA sensitivity for the conversion range.

Overall, we achieved an efficient and tuneable FWM at different wavelength ranges with three different geometries, with trade-offs unique to each geometry that could be advantageous in different applications. These studies have demonstrated the highest efficiency and longest conversion range compared to the previously reported values [29].

Chapter 3

Generalized model for Refractive index of III-V Semiconductors

3.1 Introduction

III-V semiconductors is a large family of compounds with the band-gap energies and transparency windows ranging from ultraviolet to the infrared spectral slots of the electromagnetic spectrum. As such, several applications could benefit from this group of materials. Though the necessary studies of the linear and nonlinear optical responses of some of these materials have been performed, these studies are far from being exhaustive. In particular, only very few III-V compounds have been studied for their optical properties, while there are many more materials that remain yet unexplored. Specifically, there is lack of information about basic optical characteristics such as the refractive index.

Some rudimentary attempts to quantify these properties have been performed in recent times, one of it being the prediction of the refractive index as a function of its band-gap energy [30]–[32], or electronic polarizability [33] of the material. These studies have been performed for binary semiconductor compounds. Nevertheless, the existing experimental data represent isolated measurements of some values of this parameter.

The refractive index of a material is an important intrinsic and physical parameter of the material. It is directly related to the electronic polarizability of ions and the local field inside a given material and plays an important role in the characterization of the material.

Both the knowledge of the index of refraction and the band-gap energy help in the performance assessment of a material, and also in band-gap engineering of structures for the specific application. As expected, knowledge of this index allows one to predict the behaviour of electromagnetic waves in a given material.

Studies of this material parameter in most of the ternary and quaternary III-V semiconductor compounds have not yet been reported. This piece of missing information is very crucial, and because the refractive index is the key parameter in the design of integrated optical devices (waveguides, photonic crystals, solar cells, filters, modulators, switches, LEDs, photodetectors *etc.*), this gap of knowledge is of utmost importance. Evaluating the refractive index of materials still poses a challenge because of the difficulty of evaluating these properties with an acceptable error margin. This could be seen by the epitaxial growth conditions and the design complexity of semiconductor material.

From an experimental point of view, the band-gap energies and refractive indices of a wide range of elemental and binary III-V semiconductor materials are readily available and accessible in literature, but not all of the material properties are available. Since refractive index is one of those properties that is widely missing for a number of materials, it is therefore important to formulate a theoretical and near empirical relationship between these two fundamental properties.

3.2 Refractive index as function

Experimentally, refractive indices of materials could be determined generally by using any of the following methods: deviation [34], reflection [35], interference [34], [35] and transmission [34], [35].

In recent past, several attempts have been made to estimate these refractive indices without directly measuring the experimentally. These attempts rely on the direct relationship between the refractive index and some other fundamental physical properties of the material.

Refractive index could be seen as a function of three unique parameters,

$$n(\lambda, E_g, T), \tag{3.1}$$

where λ is the wavelength of the light interacting with the material, E_g is the band-gap energy and T is the temperature. These three parameters determine to a large extent, the accessible refractive index of a material. By changing the wavelength of the interacting light, one could observe a variation of the index of refraction, conventionally referred to as dispersion. A concise overview of the most prominent approaches will be highlighted in the following subsections .

3.2.1 Refractive Index as a function of density of a material

The theoretical basis of the relationship between the reflective index and mass density lies in the state equation of polarization. This state equation relates macroscopic optical and electrical properties (dielectric constant and refractive index) of the material to its corresponding microscopic molecular properties (*e.g.*, molecular polarizability). This theory was established between mid 18th and early 20th century, and constitutes the basis of most content in electrostatics and molecular optics (*e.g.*, Aspnes - 1982 [36], Lorentz - 1916 [37] and Debye - 1929 [38]).

Gladstone–Dale Relationship

The Gladstone–Dale relation gives the index of refraction of light through a material as a sum of the optical properties of its oxide components [39]:

$$\frac{n-1}{\rho} = p_1 k_1 + p_2 k_2 + ... = \sum_{i=1}^{N} p_i k_i = C_{GD}. \tag{3.2}$$

The summation is for the addition of various oxide components (each oxide as a single entity), p_i is the weight of the i-th fraction of the oxide in the compound and k_i is the coefficient of refraction representing the polarizability of the single i-th oxide. The C_{GD} is usually referred to as the Gladstone-Dale coefficient. This equation performs and fits nicely if the solution is dilute or the refractive indices of the solute and the solvent are close to each other or the elements would have anion of oxygen and mean molecular weight close to 21 [26], [39].

3.2.2 Refractive index as a function of Wavelength of light

Light travels as waves, with the wavefronts perpendicular to the direction of motion. For example, as light moves from air into a medium, it not only reduces the speed, but also changes its wavelength without a change in the frequency. With the relationship between the speed of the wave, its frequency and its wavelength ($v = \lambda f$), and the definition of refractive index $n = c/v$, we find a relationship between the wavelength of light in a medium ($\lambda = v/f$) and the wavelength of light in vacuum ($\lambda_0 = c/f$),

$$\frac{\lambda_0}{\lambda} = \frac{c/v}{c/f} = \frac{fc}{fv} = \frac{c}{v} = n. \tag{3.3}$$

The next subsections summarizes some of the prominent models that rely on this analogy.

Cauchy Dispersion Equation

The Cauchy Dispersion equation provides a relationship between the refractive index n, and the wavelength of light λ in the following form,

$$n = A + \frac{B}{\lambda^2} + \frac{C}{\lambda^4}, \tag{3.4}$$

where A, B, and C are unique material-dependent constants.

This equation is typically used in the visible spectral regime. It is mostly applied to normal dispersion for various optical glasses exhibiting very low or no optical absorption in the far ultraviolet region. The Cauchy dispersion works best when the material has no optical absorption in the visible spectral range, and is generally characterized by a monotonous decrease in the refractive index with the increase in wavelength.

However, this formulation cannot be easily applied to metals and semiconductors. This is partly because the parameters used in the equation do not have a physical meaning, which essentially means they are not Kramers-Kronig consistent [40], hence, refractive index cannot be calculated over the entire spectral range because the extinction coefficient is not known over the spectral range.

In more recent years, the Cauchy relationship has been largely replaced by the Sellmeier equation.

Sellmeier Dispersion Equation

The Sellmeier equation is similar to the Cauchy equation. Here, the refractive index reflects the polarization of molecules by the electromagnetic field of light,

$$n = \sqrt{\sum_j \frac{A_j \lambda^2}{\lambda^2 - B_j}}, \tag{3.5}$$

where λ is the wavelength of light in vacuum, A_j and $_j$ are called the Sellmeier coefficients, typically obtained from measured data with some least-square fitting algorithm [41].
The Sellmeier data is very useful in evaluating chromatic dispersion of a material, and also used in phase-matching configurations for nonlinear frequency conversion over a wide wavelength range. This equation is applicable only to the wavelength region where the absorption is negligible.

Each of these aforementioned relations take into consideration a great deal of experimental coefficient and values. In quest for a better estimation of the refractive index without relying on tedious experiment for each material, several researchers have tried to relate the refractive index with other physical and optical properties of the material. For example, Duffy *et al.* [42], introduced the concept of optical electronegativity as it relates to energy-gap, and its application to approximating many physical material parameters. An emphasis here will be made on the relationship between the energy-gap and the refractive index of the material in the following subsections, as it forms the basis of our model.

3.2.3 Refractive index as a function of band-gap energy

The Moss Model

The first successful method of systemizing experimental data on energy gap and refractive index was done by T. Moss in 1950 [31], [43], [44]. He proposed an empirical relationship between the energy gap and the refractive index of the materials under study. The concept of this proposition was that, all energy levels in a solid are scaled by a factor of $1/\epsilon_{\text{opt}}^2$ or $\epsilon_{\text{opt}} = n^2$, where n is the refractive index and ϵ_{opt} is the optical dielectric constant of the material which is equal to the square root of the refractive index. This proposition was based on the theory of photoconductivity. He found that the absorption of an optical quantum essentially raises an electron to an excited state instead of freeing the electron. This raised state is followed by the movement of the electron to the conduction band by thermal energy from the lattice. This effect is only observed at certain points of imperfection within the lattice, therefore making the electron to behave as if it were an isolated atom with a dielectric of a bulk material. The scaling factor is proportional to the energy required to raise an electron in a lattice to an excited state in a Bohr atom.

Hence he proposed the energy gap-refractive index relationship [31],

$$n = \sqrt[4]{\frac{K}{E_g}} \qquad K = 95, \tag{3.6}$$

otherwise written as

$$n^4 E_g = 95 \text{ eV} \qquad K = 95, \tag{3.7}$$

where n is the refractive index and E_g is the energy gap.

Ravindra Model

Ravindra, *et al.* [45], proposed a relation based on the Moss' model, connecting energy gap to the refractive index in a photo-conducting material. This model is based on the feature that, in the band structure of all semiconductor materials, the valence and the conduction band are more or less parallel to each other at least along the symmetry directions [32], [45], [46]. From this, he came up with the equation,

$$n = 4.048 - \beta E_g \qquad \beta = -0.62 \text{ eV}^{-1} \tag{3.8}$$

The Ravindra relation is seen as an approximation of the Penn Model [47].

Herve and Vandamme Model

Herve and Vandamme [48] separated semiconductor materials into two main groups, the covalently bonded group and the ionically bonded group. For the covalently bonded group, the dielectric function is represented as a function of the valence electron density, the mass of the electron at rest and the UV resonant frequency. This describes materials like Si and Ge, but for materials like NaCl and GaAs, it would have to be represented as an ionic bonded group, which is a function of plasma frequency infrared resonance frequency of the ions. The Herve and Vandamme model is described as

$$n = \sqrt{1 + \frac{A^2}{(E_g + B)^2}} \qquad A = 13.6 \text{ eV}, \ B = 3.47 \text{ eV}, \tag{3.9}$$

where A is the hydrogen ionization energy, and B is a constant, taken to be the difference between UV resonance energy and the band-gap energy.
This equation is based mainly on the oscillatory theory, with the assumption that the UV resonance energy has a constant difference with the band gap energy. In conducting the study leading to this relationship, Herve and Vandamme found that there is a dependency between energy gap and temperature (T), which is inversely proportional to each other for most semiconductors, *i.e.,* as T increases, the energy gap decreases, and consequently, the refractive index increases.

Reddy, *et al.* Model

Reddy, *et al.* [49], proposed a correlation between the refractive index of a material and Plasmon energy, and then calculated the values of various other physical properties like atomic force constant and lattice energy for both II-VI and III-V semiconductor materials. Reddy extended this study to include refractive index as a function the energy gap using the following relation [49]–[51],

$$n = \sqrt{\frac{12.417}{E_g - 0.365}}, \tag{3.10}$$

which could also be written as

$$n^4 \left(E_g - 0.365\right) = 154. \tag{3.11}$$

This model is a direct modification of Moss' equation with an additional arbitrary constant (0.365) to improve the obtained results.

Kumar and Singh Model

Kumar and Singh model [32] is a result of software simulation. Based on experimental values of band-gap and refractive index, he obtained the relation

$$n = KE_g^c, \tag{3.12}$$

where $K = 3.3668,\ C = -0.32234$

Tripathy Model

Tripathy [52], fitted an exponential empirical relation to the experimental values of the refractive index and energy gap using some binary and elemental semiconductor materials over a very wide range of energy gap values ranging from 0.1 eV to 8.5 eV. The resulting equation is

$$n = n_0 \left[1 + \alpha e^{-\beta E_g}\right], \tag{3.13}$$

with $n_0 = 1.73,\ \alpha = 1.9017,\ \beta = 0.539\text{eV}^{-1}$.

Other Fitted Models

Other theoretical models have been proposed based on fitting the same experimental values takes from well-known materials, and an evaluation is made to obtain the refractive indices of other materials whose data is not available. They are an optimization of some of the previously developed models, with the emphasis on the strengths of these models. The proposed results were relatively close to the experimental values with a relatively low error margin.

Anani *et al.* Model [30]:

$$n = 1 + \frac{A}{\left(E_g^2\right)^4} \qquad A = 40.8 \text{ eV}. \tag{3.14}$$

Ahmad and Haq Model [33]:

$$n = \sqrt[3]{\frac{44}{E_g}}. \tag{3.15}$$

3.2.4 Analysis of examined models

Table 3.1 summarises the various studied models, their equations and their various range of validity. Looking at this table, the Ravindra relation (Eq. 3.8) predicts impractical results for some energy gaps. From its prediction, the refractive index of a the material will be zero when the energy gap is at about 6.5 eV. For semiconductor materials, this is impractical to have zero refractive index. On the other hand, Moss's relation [Eqs.(3.6) - (3.7)] estimates the energy gap to be infinite to yield the same result.

With Moss's model, to yield a refractive index of 1, the energy gap has to be 5 eV. This seems quite achievable but there are some semiconductor materials with larger energy gaps, such as AlN (E_g = 6.2 eV), and their refractive indices are much greater than 1. This posses a limitation on using Moss' model with wide band-gap materials. In the same way, Ravindra's relation requires that the energy gap be greater than 100 eV to obtain the refractive index of 1. 100 eV is much larger than the band-gap energy of any known semiconductor material.

Moss's relation is valid for the band-gap energies between 0.17 eV $\leq E_g \leq$ 3.68 eV, while Ravindra's model is valid for band-gap energy $E_g < 6.587$ eV. Calculations made using Ravindra's relationship shows more accuracy in estimating band-gap values less than 1.43 eV.

The Reddy, *et al.* model [(Eq. 3.10), is a modified form of Moss's equation, but with an additional arbitrary constant 0.365. The most outstanding drawback of this equation is that the refractive index of a material becomes zero with the energy gap lower than 0.365eV. This relation is valid for values of the band-gap energy between 1.1 eV $\leq E_g \leq$ 6.2 eV.

Kumar and Singh's model [(Eq. 3.12)] experiences great offsets where it under predicts the indices for high values of energy gap and over predicts for medium energy gap range. This relation, however, succeeds in predicting the refractive index in the range 2 eV $\leq E_g \leq$ 4 eV. It also predicts very high refractive index values with fair deviations in the range of the band-gap energies 6.2 eV $\leq E_g \leq$ 8.5 eV.

One common trend in all these energy gap-refractive index relations is that, they are in agreement with the experimental values in the medium energy gap region (2 eV $\leq E_g \leq$ 4 eV). Having seen the shortcomings and the strong points in these models, We take these efforts further by presenting a model capable of developing the refractive index of ternary and quaternary III-V semiconductor materials from their band-gap energy, with an improved error margin. The next subsection provides the description of this proposed model.

3.2.5 Proposed Model

In this section, the proposed model is presented. As my entire research was done as part of a team effort, I would like to mention there that the model proposed here is solely my initiative and my effort, unless otherwise mentioned.

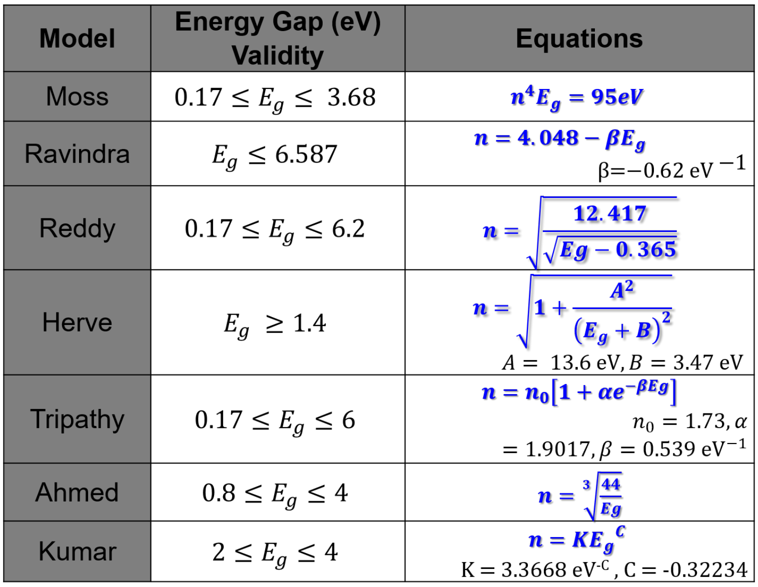

Model	Energy Gap (eV) Validity	Equations
Moss	$0.17 \leq E_g \leq 3.68$	$n^4 E_g = 95eV$
Ravindra	$E_g \leq 6.587$	$n = 4.048 - \beta E_g$ β=−0.62 eV $^{-1}$
Reddy	$0.17 \leq E_g \leq 6.2$	$n = \sqrt{\frac{12.417}{\sqrt{Eg - 0.365}}}$
Herve	$E_g \geq 1.4$	$n = \sqrt{1 + \frac{A^2}{(E_g + B)^2}}$ $A = 13.6$ eV, $B = 3.47$ eV
Tripathy	$0.17 \leq E_g \leq 6$	$n = n_0[1 + \alpha e^{-\beta Eg}]$ $n_0 = 1.73, \alpha = 1.9017, \beta = 0.539$ eV^{-1}
Ahmed	$0.8 \leq E_g \leq 4$	$n = \sqrt[3]{\frac{44}{Eg}}$
Kumar	$2 \leq E_g \leq 4$	$n = KE_g{}^C$ K = 3.3668 eV^{-C}, C = -0.32234

FIGURE 3.1: Table showing validity of tested models

This model was developed based on the available experimental data of the band-gap energy of refractive indices of various semiconductor materials. The resulting model is capable of evaluating the refractive indices of various semiconductors, oxides, insulators and halides for the entire range of known energy gap (E_g = 0.1 – 8.5 eV).

The flow process for the proposed model is graphically presented in Fig. 3.2.

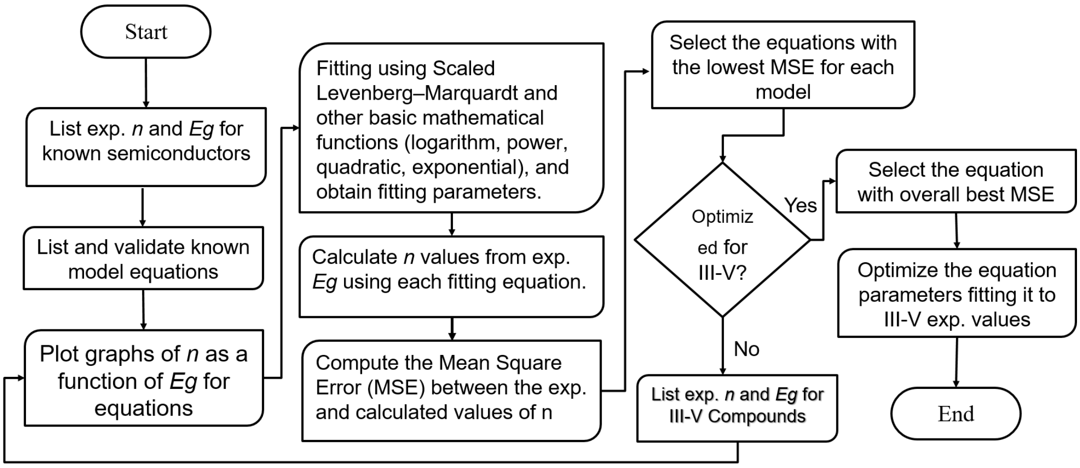

FIGURE 3.2: Flowchart of proposed model developed for estimating the refractive index of III-V semiconductors

Fig. 3.2 can be described in detail with the following steps,

1. Parameter acquisition: gather all semiconductor compounds, their energy gap and their corresponding experimental refractive index values from the literature.
2. List and validate all known refractive index-energy gap models. Each model is tested to validate the correctness of the published data and the model's function before being adopted. This is to allow reproducibility of the published model for correct representation of data.
3. Plot a graph of refractive index against the band-gap energy for each listed model in step 2.
4. Perform curve fitting using Scaled Levenberg–Marquardt and other mathematical functions (Power, Exponential, Polynomial, and Logarithm) for each of these graphs in step 3 above. Each fitting function would have a separate equation output and a separate graph for each of the model. This was done as crude approach to optimise these models.
5. Extract the curve equation from each fitted graph of each fitting function.
6. Calculate the refractive indices from the experimental energy gap values using equations from each fitted graphs.
7. Compute the Mean Square Error (MSE) between the experimental refractive index values and the calculated values in step 6.
8. Select the equation with the lowest MSE for each of the models.
9. Re-list the compounds for III-V semiconductor materials only, tabulating their experimental energy gap and their corresponding refractive indices.
10. Repeat steps 3 – 7.
11. Select the equation with the overall best Mean Square Error.
12. Optimize the parameters of the obtained equation for III-V Semiconductors.

    The parameters of the equation are varied iteratively and compared with the known experimental data to find the best value. Here we used well-studied data from binary III-V semiconductor materials to adjust the fitting parametesr.
13. Represent the final equation.

14. Plot a graph of predicted n as a function of experimental E_g using the final optimized equation from step 13, as well as the experimental values of the experimental n and E_g to evaluate the results.
    These results are presented in Tables 3.1 – 3.3, and in appendix A.

Each resulting equation from each stage of the iteration is compared against the known experimental value; the deviation from the experimental value as predicted by the equation is recorded. Then the same equation is simulated against its best fit value (value with the best minimal error in deviation) of each material. The average deviation is computed from the tabulated deviations of these materials. These deviations now provide information about the error margin for each iterative stage. The process is repeated until the lowest error is obtained.

The result of the simulation presents a model best fit for computing the relationship between the refractive index n and the energy gap (in eV) of binary, ternary and quaternary III-V semiconductor materials. This model is given as

$$\begin{gathered} n = Ae^{-0.116E_g} \\ A = 3.893. \end{gathered} \tag{3.16}$$

where A = 3.893. A is a numerically generated constant, also considered as a fitting parameter, fixed specifically for III-V semiconductor materials, while E_g is the band-gap energy of the material.

TABLE 3.1: Table showing Energy gap and refractive indices of some known binary III-V semiconductors with computed values from studied models.

Material	$^{\star}E_g$ **(eV)**	**Refractive index (n)**								
		***Exp. (*n*)**	**Moss**	**Ravindra**	**Reddy**	**Herve**	**Kumar**	**Ahmad**	**Tripathy**	**Proposed Model**
InSb	0.18	3.95	4.7931	3.9724	Impossible	3.8579	5.8525	6.2526	4.6885	3.8126
InAs	0.36	3.50	4.0305	3.8608	Impossible	3.6890	4.6804	4.9627	4.4140	3.7338
InN	0.70	2.90	3.4132	3.6500	4.6318	3.4113	3.7771	3.976	3.9629	3.5894
GaSb	0.81	3.79	3.2909	3.5818	4.3144	3.3312	3.6035	3.7872	3.8338	3.5439
$^{\diamond}$GaAs	1.42	3.30	2.8579	3.2011	3.4736	2.9534	3.0041	3.138	3.2382	3.3002
AlSb	1.80	3.19	2.6953	2.9680	3.2196	2.7676	2.7855	2.9022	2.9597	3.1594
AlAs	2.16	3.00	2.5752	2.7448	3.0443	2.6144	2.6265	2.7311	2.7411	3.0302
GaP	2.24	2.90	2.5519	2.6952	3.0113	2.5832	2.5959	2.6982	2.6980	3.0022
AlP	3.00	2.75	2.3722	2.2240	2.7658	2.3278	2.3625	2.4478	2.3693	2.7488
$^{\diamond}$GaN	3.50	2.40	2.2825	1.9140	2.6482	2.1925	2.2480	2.3252	2.2159	2.5939
†AlN	6.20	2.16	1.9785	0.2400	2.2672	1.7257	1.8695	1.9217	1.8357	1.8964
Error			-3.73%	-11.14%	11.22%	-7.55%	2.61%	7.47%	1.95%	1.81%
MSE			0.0202	0.0878	0.0437	0.0162	0.0484	0.0637	0.0276	0.0081
χ^2			0.0692	0.4290	0.1351	0.0644	0.1571	0.2015	0.1004	0.0323

$^{\diamond}$ taken from [53]

$\star$ taken from [54]

† taken from [55].

The table provides generic statistical computations of Mean Square Error (MSE) and a chi-square test value. The the chi-square value (χ^2) shows the result of any statistical hypothetical test for assessing the goodness of a fit parameter as seen by comparing the observed values with those expected theoretically, or in our case, experimentally. The error, MSE and χ^2 as seen in Table 3.1 are defined as follows,

$$\text{Error} = \frac{1}{d}\sum_{i=1}^{d}\frac{\left(n_i^{\mathrm{m}} - n_i^{\mathrm{e}}\right)}{n_i^{\mathrm{e}}}, \tag{3.17}$$

$$\text{MSE} = \frac{1}{d}\sum_{i=1}^{d}\frac{\left(n_i^{\mathrm{m}} - n_i^{\mathrm{e}}\right)^2}{n_i^{\mathrm{e}}}, \tag{3.18}$$

and

$$\tilde{\chi}^2 = \sum_{i=1}^{d}\frac{\left(n_i^{\mathrm{m}} - n_i^{\mathrm{e}}\right)^2}{n_i^{\mathrm{e}}}, \tag{3.19}$$

where n_i^{m} is the refractive index computed from the proposed model, n_i^{e} is the known experimental refractive index, i is the iteration, and d is the number of samples/materials.

Using this model, the refractive indices for materials listed in the last column of Table 3.1 is obtained.
Our model was tested against over 120 materials as detailed in appendix A, and was found to be in fairly good agreement with the experimental data.
The general form of the model is presented with a fitting parameter A, with a single idea in mind which is, a single equation cannot, with an acceptable level of accuracy, predict the refractive indices of all the materials for the entire range of energy-gaps of semiconductors. Therefore, the parameter A could be varied to best fit a certain group of semiconductor material of interest to provide an acceptable margin of deviation using appropriate curve fitting algorithms. The fitting parameter works for a particular group of materials for reason being that, each of these groups have similar opto-electrical, mechanical and physical properties and are expected to likely have similar responses to electromagnetic waves.

From Table 3.1, the refractive index of GaAs, which is one of the most studied III-V semiconductor compound is predicted with an error margin of 0.0002, *e.g.*, experimental value of GaAs is known to be 3.3000 and the model predicts an index of 3.3002, also for AlP with the experimental refractive index value of 2.7500, our model predicts 2.7488 which has -0.0012 error. Looking

at material the like AlAs with experimental refractive index of 3.0000, our model predicts the index to be 3.0302 with the error of 0.00302.
Overall, our model predicts values very close to the experimental value for III-V semiconductor materials, well above other existing models.

On examining this model, we found that the model performs best with energy-gaps between 0.17 eV and 6.2 eV.
The trade-off in this proposition is, if we crudely consider the entire range of semiconductor materials using a single function, one would have to choose between the tolerance levels in accuracy and the percentage deviation from the expected experimental value. The proposed model [(Eq. 3.16)] presents the lowest Mean Square Error (MSE) of 0.0081 and χ^2 of 0.0323 with the error margin between -0.3443 and +0.6894. Next to it is Herve's model, with MSE of 0.0162 and χ^2 of 0.0644 having an error margin between -0.6795 and +0.5113.
The margin of error is calculated by subtracting the predicted value from the experimental value, the highest and the lowest deviation becomes what is referred here as an error margin.

TABLE 3.2: Refractive Indices of $Al_xGa_{1-x}As$ against Al Composition of Gehrsitz model [25], compared with studied models and the proposed model.

x	E_g **(eV)**	**Refractive Index (*n*)**								
		Exp. (*n*)	**Moss**	**Ravindra**	**Reddy**	**Herve**	**Kumar**	**Ahmad**	**Tripathy**	**Proposed Model**
0	1.4241	3.3000	2.8579	3.2011	3.4736	2.9533	3.0041	3.1379	3.2381	3.3002
0.1	1.5556	3.2498	2.7955	3.1195	3.3734	2.8850	2.9197	3.0469	3.1343	3.2502
0.2	1.6843	3.1985	2.7405	3.0397	3.2879	2.8217	2.8459	2.9672	3.0395	3.2021
0.3	1.8102	3.1524	2.6915	2.9617	3.2139	2.7630	2.7805	2.8967	2.9529	3.1557
0.4	1.9333	3.1081	2.6476	2.8854	3.1488	2.7084	2.7221	2.8339	2.8738	3.1109
0.5	2.0880	3.0629	2.5972	2.7894	3.0757	2.6434	2.6554	2.7621	2.7815	3.0556
0.6	2.2198	3.0165	2.5577	2.7077	3.0195	2.5910	2.6035	2.7063	2.7086	3.0092
0.7	2.3701	2.9716	2.5162	2.6145	2.9612	2.5344	2.5491	2.6479	2.6317	2.9572
0.8	2.5466	2.9284	2.4714	2.5051	2.8994	2.4717	2.4907	2.5852	2.5490	2.8973
0.9	2.7573	2.8858	2.4228	2.3745	2.8334	2.4020	2.4277	2.5176	2.4600	2.8273
1	3.0100	2.8470	2.3702	2.2178	2.7631	2.3248	2.3600	2.4451	2.3658	2.7457
Error			-15.02%	-10.06%	0.87%	-13.81%	-13.05%	-9.54%	-9.07%	-0.66%
MSE			0.0227	0.0134	0.0006	0.0196	0.0176	0.0098	0.0103	0.0002
χ^2			0.0819	0.0505	0.0022	0.0716	0.0642	0.0361	0.0383	0.0006

Next, we test our model against ternary III-V semiconductors, with AlGaAs as the benchmark. Here, AlGaAs is in a unique position to be used a benchmark because the information about its refractive indices and energy gap is available for all its compositions. From the Table 3.2, it is evident that the proposed model out-performs the existing models in predicting the refractive index as a function of the band-gap energy for AlGaAs, using the well-known Gehrsitz model [25] to interpolate the material properties. This comparison yielded coefficient of determination of 0.9954, which shows that the calculated values are 99.54% close to the experimental value. The MSE and χ^2 were computed to be 0.0002 and 0.0006 respectively. It is also seen that the proposed model presents better agreement with the known experimental values of ternary III-V semiconductor materials than the existing models.

So far, the model has demonstrated good a accuracy level and proves better that other existing models, but this only happens under specific conditions. As mentioned earlier, refractive index is a function of a number of parameters. As our model does not account for material dispersion yet, it achieved its accuracy by fixing the temperature to room temperature (297K), and then varying the concentrations to give an interpolated bang-gap for ternary and quaternary compounds. A crucial part of the evaluation was in the fixing of the wavelength of the interacting light to wavelength in mid or near-IR regime and also to wavelengths below the band-gap. By changing the wavelength of light, we have access to a different refractive index of the material. For materials like AlGaAs that is very widely studied, fixing the wavelength below the band-gap and trying to correlate this wavelength with a known band-gap energy was easy by using Gehrsitz model [25], thereby reducing a three-parameter space (E_g, λ, T), to just one parameter, the energy gap, allowing for easy computation. This approach did well for ternary compounds because it has just one degree of freedom, as seen with AlGaAs in Table 3.2. However, this approach yielded a widely dispersed values with the quaternary compounds mostly because of their complexity, having two degrees of freedom that are independently varied to interpolate the energy gap.

It was observed that when we fix the wavelength of the interacting light to 94% of the band-gap equivalent wavelength ($0.94E_g$), the proposed model achieved predictions very close to the reported experimental values, as seen with InGaAsP in Table 3.3. This value was however tailored for specific material, in this case, InGaAsP.

TABLE 3.3: Table showing refractive index of $In_{1-x}Ga_xAs_yP_{1-y}$ compared against As Composition using Adachi's model [56] vs proposed model at λ = 0.95E$_g$ and T = 297K.

As Comp (y)	**As Comp (x)**	E_g **(eV)**	**Refractive Index (*n*)**								
			Adachi Model	**Moss**	**Ravindra**	**Reddy**	**Herve**	**Kumar**	**Ahmad**	**Tripathy**	**Proposed Model**
0	0.00	1.3500	3.1380	2.8963	3.2470	3.5371	2.9935	3.0563	3.1943	3.3000	3.3287
0.1	0.05	1.2792	3.1780	2.9356	3.2909	3.6037	3.0332	3.1098	3.2522	3.3615	3.3561
0.2	0.09	1.2108	3.2140	2.9762	3.3333	3.6744	3.0728	3.1654	3.3123	3.4231	3.3829
0.3	0.14	1.1448	3.2500	3.0182	3.3742	3.7498	3.1121	3.2232	3.3747	3.4848	3.4089
0.4	0.18	1.0812	3.2890	3.0616	3.4137	3.8304	3.1511	3.2831	3.4397	3.5463	3.4341
0.5	0.23	1.0200	3.3200	3.1066	3.4516	3.9169	3.1898	3.3454	3.5071	3.6076	3.4586
0.6	0.28	0.9612	3.3520	3.1530	3.4881	4.0101	3.2279	3.4100	3.5772	3.6684	3.4823
0.7	0.32	0.9048	3.3890	3.2011	3.5230	4.1110	3.2656	3.4772	3.6501	3.7285	3.5051
0.8	0.37	0.8508	3.4250	3.2507	3.5565	4.2208	3.3026	3.5469	3.7257	3.7878	3.5271
0.9	0.42	0.7992	3.4680	3.3019	3.5885	4.3410	3.3389	3.6191	3.8042	3.8461	3.5483
1	0.47	0.7500	3.5630	3.3548	3.6190	4.4735	3.3743	3.6940	3.8857	3.9033	3.5686
Error				9.78%	-0.20%	14.43%	-7.65%	-2.76%	1.96%	4.43%	0.12%
MSE				0.0103	0.0004	0.0252	0.0063	0.0026	0.0026	0.0035	0.0001
χ^2				0.0332	0.0011	0.0794	0.0201	0.0084	0.0081	0.0109	0.0002

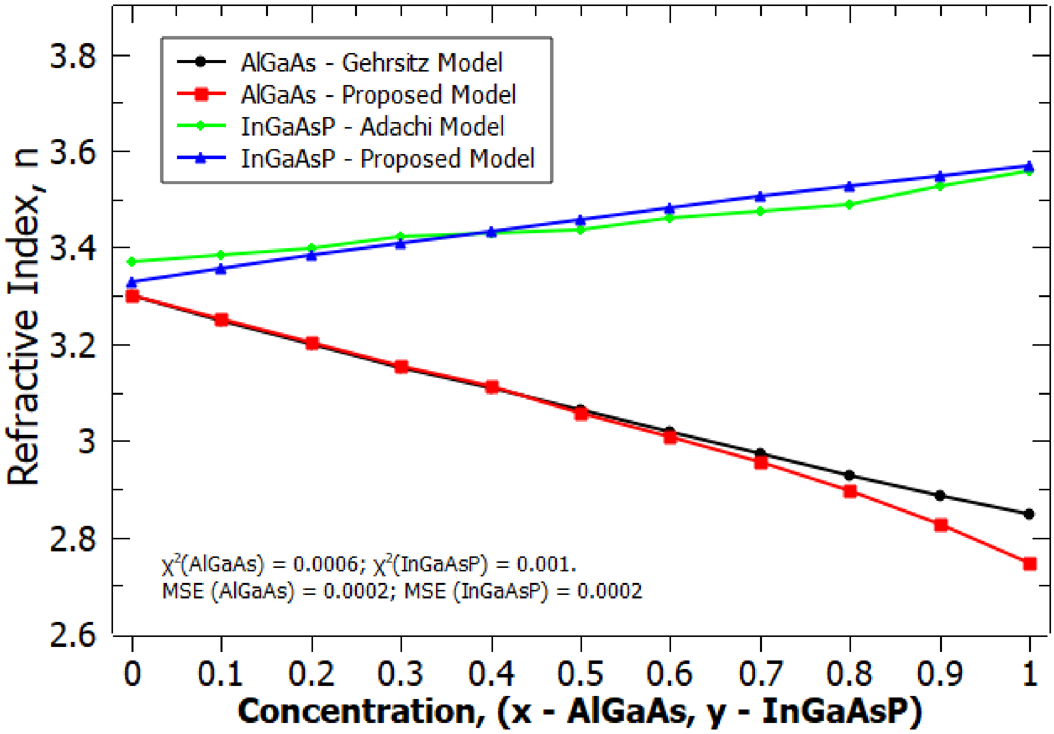

FIGURE 3.3: Refractive index as a function of As composition in $In_{1-x}Ga_xAs_yP_{1-y}$ at $\lambda = 1850$ nm, T = 297K using Adachi's model [56], and refractive index as a function of Al composition in $Al_xGa_{1-x}As$ using Gehrsitz model [25].

Values of the proposed model for AlGaAs and InGaAsP from Tables 3.2 and 3.3 are represented graphically in Fig. 3.3. Testing the model against quaternary III-V semiconductor materials, it is seen from the Table 3.3, that the proposed model still performs better than the existing models in predicting the refractive index as a function of the band-gap energy for InGaAsP, using Adachi's model [56] to interpolate the material properties. This comparison yielded coefficient of determination of 0.9872, which shows that the calculated values are 98.72% close to the experimental values. The MSE and χ^2 was computed to be 0.0001 and 0.0002, respectively.

3.3 Conclusion

We have demonstrated the uniqueness of our model in predicting the most accurate refractive index value from the energy-gap of binary, ternary and quaternary III-V semiconductors. As a basis of comparison with other existing models, basic statistical computations were done. Fractional error (Error), mean-square error (MSE) and chi-square test values (χ^2) were used as the figure of merit. This therefore demonstrates the soundness and accuracy of our model. This model provides a timely solution for obtaining the missing refractive index values for the design of integrated optical devices using ternary and quaternary III-V semiconductor materials as a suitable material platform. However, since our model does not account for dispersion at the moment, as has not been addressed either by previous researchers, it should therefore be used intelligently to avoid complications and bogus material parameters. Also, we are yet to develop a physical explanation to support our model. These two areas would be the future endeavour of this project.

Chapter 4

Nonlinear Photonic Integration: Quest for new materials

4.1 Introduction

As mentioned earlier in this thesis, integrated photonics holds great potentials to be exploited in several applications. Among these applications are, nonlinear wavelength conversion, which is necessary to extend the operation range of the current integrated laser sources, and all-optical signal processing which would solve the fundamental bottleneck of electronic signal processing.

In the quest for and efficient material candidate, several material platforms have been considered, and the group of III-V semiconductors stand out to be a unique group of materials with promising properties. However, in this group, only materials like AlGaAs [11], [22]–[24], [29] have been extensively studied for its potential application in integrated photonics. More recently, AlGaAsSb [57]–[59] and has been explored for their application in integrated optics. There still exist quite a number of III-V semiconductor compounds that have not been well studied for their optical properties and their potential application in nonlinear photonics on-a-chip. Therefore, exploring new materials and structures for the development of ultra-compact integrated photonic systems is of great technological and scientific interest for optical and photonic applications. We take this step forward, exploring other III-V material candidates for their potentials to serve as an efficient material platform for nonlinear photonics.

Waveguides are the basic building blocks in integrated photonic circuit and devices [60]. For this reason, in order to explore the potential of a compound for integrated photonics, waveguides are designed based on this material.

4.2 Material Selection Criteria

As mentioned earlier, a waveguide is an optical structure that guides light. It consists of a region or layer that is made from a higher refractive index material known as the core, embedded in a layer made from a lower refractive index medium called the cladding. The principle of light guidance in photonic waveguides is such that, as the light enters the medium with higher refractive index at an angle, greater than or equal to the critical angle, this higher refractive index material acts as a "trap" for the light by guiding it through multiple total internal reflections at the boundaries between the core and the cladding, as shown in Fig. 1.26.

In this chapter, we will go into details about the specific requirements and criteria for designing a nonlinear optical waveguide using ternary and quaternary III-V semiconductor compounds.

4.2.1 Material composition selection

The first step in designing an optical waveguide with ternary and quaternary III-V semiconductor material is to select the appropriate material for the specific application of interest. Ternary and quaternary III-V semiconductor materials are superpositions of elemental and binary compounds as described in section 1.5.1. These elemental and binary semiconductor compounds are combined in such a manner that one can have some control over the characteristics of the resulting ternary or quaternary III-V semiconductor within a given parameter space. The ternary compounds can be schematically represented as $A_xB_{1-x}C$, where A, B, and C are individual constituent element of the compound. The parameter x is the mole fraction of the element A, which can range from 0 to 1. By varying x, the properties of this material can be modified. A quaternary semiconductor compound can be represented in a similar fashion as $A_xB_{1-x}C_yD_{1-y}$, where A and B, by convention, represent elements from the column III, while C and D are elements from the column V of the Periodic Table. A quaternary compound typically has two degrees of freedom as the mole fractions x and y can now be adjusted independently. The adjustment of the concentration not only changes the refractive index and the energy gap, but also changes the lattice constant of the material, with an exception in the case of AlGaAs. With AlGaAs, the composition adjustment does not affect the lattice constant, this is because the layers are lattice-matched for the entire composition of Aluminium. Material selection is primarily determined by the specific application of interest, where one would have to first consider the operation wavelength of the intended application, as described in section 1.5.4. Material selection is also determined by the lattice matching of the involved material compositions. Since the development of these waveguides require the growth or integration of different layers of highly ordered functional heterostructures, crystal lattice of the materials have to be matched in order to grow them on top of each other in a defect-free manner.

4.2.2 Lattice Matching

The waveguides we are developing are based on hetero-structures, where layers of the material with different compositions are epitaxially grown on top of each other. These material compositions are chosen such that there is a match in their lattice constants in order to reduce the stress on the film. If one tries to grow layers of unmatched lattice parameter, it causes strained or relaxed growth in the film and this leads to an inter-facial tension between the film and the substrate. As a result of this strain, the optical quality of the film is compromised. Although it is impossible in practice to match perfectly, the lattices of the layers, it is possible to match the lattices almost perfectly, such that the defects are minimized as much as possible, which makes the undesired effects negligible. Fig. 4.1 is a schematic representation of a well lattice-matched, strained and relaxed structure.

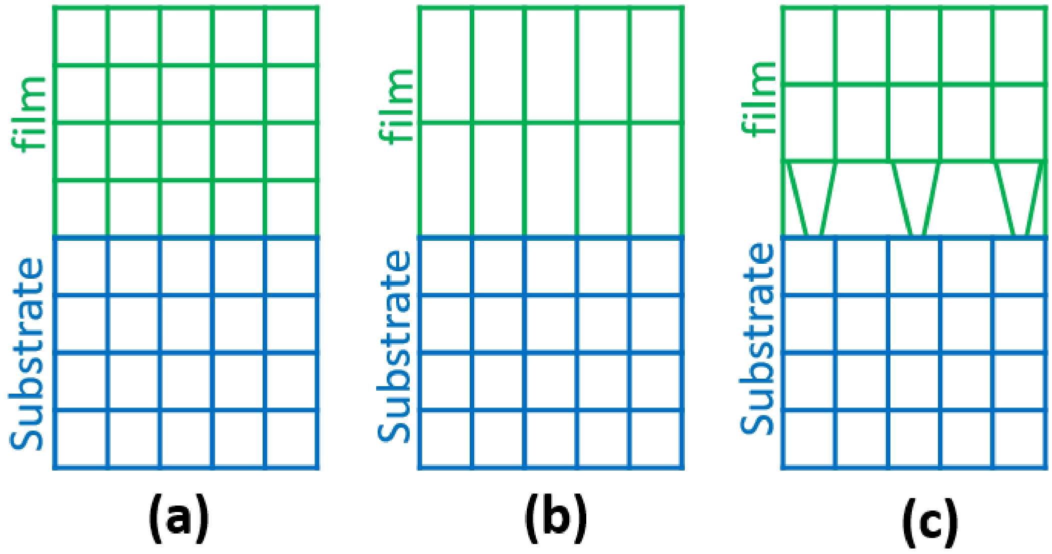

FIGURE 4.1: Schematic representation of film growth on top of a substrate while it is epitaxially (a) lattice-matched, (b) strained and (c) relaxed.

The parameter describing the lattice mismatch is defined as: $\Delta a/a$, where a is the lattice constant of the substrate, and Δa is the difference between the lattice constant of the film and the lattice constant of the substrate. If the lattice mismatch is large, then the film will be strained in order to accommodate the structure on the substrate, as seen in Fig. 4.1 (b). However, if the film thickness exceeds a critical value, it creates dislocation defects at the interface. This will form a relaxed epitaxy which will make the film layer to return to its initial lattice structure above the interface, as seen in Fig. 4.1 (c) [61]. This lattice mismatch ultimately results in poor-quality epitaxial growth of the material, and consequently, the grown material exhibits low optical properties.

4.2.3 Epitaxial Growth: MOCVD and MBE

In growing heterostructures, one would have to first define the vertical layered structure which is called the *wafer*. There are two main technologies/processes for growing heterostructures with III-V semiconductor compounds, namely: Metal Organic Chemical Vapour Deposition (MOCVD) and Molecular Beam Epitaxy (MBE).

MOCVD is used to grow multi-layers crystalline structures by depositing thin layers of atoms on a semiconductor material substrate. In MOCVD, atoms are added to the crystal by combining it with organic reactant gas molecules at an elevated temperature in a reactor to cause a chemical reaction where the heat splits the molecules, and then these atoms are deposited on the substrate surface [62]. Most common organometallic reagents for III-V material growth are Trimethylgallium (TMGa), Trimethylindium (TMIn), Monoethyl arsine (MEAs), Phosphine(PH3), and Tertiarybutyl phosphine (TBP).

MBE is an epitaxial method of depositing thin-films on crystals. This process takes place usually in a very high or ultra-high vacuum ($10^{-8} - 10^{-12}$ Torr) and high temperatures. The Ultra-High vacuum chamber ensures material purity in a complete dust-free environment. The deposition process starts with heating the substrate to high temperatures up to hundreds of degrees, and then molecular beams are fired onto the substrate. These fired molecules on the surface of the substrate then condense and gradually build up thin layers, eventually forming the desired crystal. The choice of growth method is largely determined by the application of interest as both perform well. However, MOCVD is less complicated, less expensive and less precise compared to MBE. It also has a much faster growth rate, which is why it is mainly used for large-scale production. MBE is more complicated, yet very precise in controlling the thickness of the layers, but with slower growth rate. It is mainly used in the laboratory for process optimization [63].

4.2.4 Refractive index contrast

As mentioned earlier in section 1.5.1, the refractive index of a ternary and quaternary III-V semiconductor compound depends on the mole fractions x and y of the chemical elements in its composition. To achieve a maximum modal confinement in the waveguide, one needs the refractive index contrast between the guiding layer (core) and claddings such that $\Delta n = n_{\text{core}} - n_{\text{cladding}}$ is at maximum achievable value. The higher the index contrast, the more confined the mode is, and consequently, there is better light guidance in the core of the waveguide. However, if the refractive index contrast is very small, then the mode will not be well confined, it would leak, penetrating into the surrounding media (cladding and air), thereby making the waveguide very lossy. Having listed the fundamental requirement for a promising material candidate, the next subsections details these materials and their known properties.

4.3 Potential Material Candidates

As described above, in the design of integrated optical devices using ternary and quaternary III-V semiconductors, the composition of the individual compounds or element is adjusted to yield a band-gap equivalent wavelength that is less than two times the wavelength of the interacting light. This is done to shift away from the absorption edge of the material while still maintaining a large refractive index contrast between the core and the cladding. This material is also selected with the ability to be lattice-matched with a III-V material substrate with relatively small lattice mismatch and commercially available epitaxial growth recipe. Based on these, the following material candidates are of interest.

4.3.1 Indium Gallium Phosphide Nitride

Indium Gallium Phosphide Nitride, $In_xGa_{1-x}P_yN_{1-y}$, is a quaternary III-V compound of InGaP and InGaN. This compound has gained much attention in the past decade for its excellent optical properties in the design of transistors and light emitting diodes due to its strong photoluminescence and electroluminescence which comes as a result of Nitrogen incorporation. With semiconductor heterojuctions, the discontinuity caused by the difference in the energy bands of the two materials when they align with each other close to the interface, is reduced to zero or almost zero as a result of the Nitrogen incorporation. This alignment in the energy bands of the semiconductor heterojunction is referred to as *Band offset*.

Common Use

In recent past, $Ga_{0.52}In_{0.48}P$, lattice-matched to GaAs, has received a lot of attention due to its applications in electronic and opto-electronic devices. These devices include heterojunction bipolar transistors (HBTs) [64], lasers [65], and high efficiency tandem solar cells [66]. It has significant advantage over materials like AlGaAs/GaAs due to its larger valence-band discontinuity (for use in HBT applications), better etch selectivity, and less oxidation effect [67]. By incorporating a small percentage of Nitrogen into $Ga_{0.52}In_{0.48}P$, it provides a better system for high-brightness RGB LEDs for use in outdoor displays, traffic signals and automatic lighting [68]. So far, $In_xGa_{1-x}P_yN_{1-y}$ is mostly used in solid-state lighting.

Substrates

$In_xGa_{1-x}P_yN_{1-y}$ could be grown on GaAs (100) semi-insulating substrate by gas-source molecular beam epitaxy (GS-MBE) [69] with thermally cracked arsine (AH_3), elemental gallium (Ga) and indium (In), phosphine (PH_3) and an RF plasma nitrogen radical beam source. The surface oxide of GaAs substrate is removed at a high temperature of about 600 °C under As_2 flux, then a 100 nm thick GaAs buffer is grown. The growth of the buffer layer is followed by nitrogen plasma ignition at a lowered substrate temperature between 380 and 480 °C [67].

$In_xGa_{1-x}P_yN_{1-y}$ can also be grown on GaP (100) substrate using solid-source molecular beam epitaxy (SS-MBE) with RF-plasma source for the active Nitrogen flux [70]. To grow this material, a 20-nm-thin buffer layer was grown on the GaP substrate at a temperature of about 590 °C, followed by a 500-nm-thick InGaPN grown on the substrate at a reduced temperature of about 460 °C and a final 50-nm GaP capping layer [71]. The growth rate of 1 μm/h was used, and the grown samples showed mirror-like surfaces.

Lattice Matching

Bulk $In_xGa_{1-x}P_yN_{1-y}$ can be lattice-matched to GaAs(100) [67] when

$$(x - 0.48) = 2.8y. \tag{4.1}$$

$In_xGa_{1-x}P_yN_{1-y}$ growth on GaP was performed with the lattice-matching condition [70]

$$x \approx 2.4y. \tag{4.2}$$

Lattice mismatch for $In_xGa_{1-x}P_yN_{1-y}$/GaP was reported to be less than 0.1% [71], while $In_{0.54}Ga_{0.46}P_yN_{1-y}$/GaAs exhibited about 0.42% of mismatch with 1% and 2% of Nitrogen. However, the $In_{0.54}Ga_{0.46}P_yN_{1-y}$/GaAs mismatch was seen to decrease with an increase in the concentration of Nitrogen, but with the side effect of adverse epitaxial quality of the samples [69].

Energy gap

$In_xGa_{1-x}P_yN_{1-y}$/GaAs is known to have a reduced band-gap due to the incorporation of Nitrogen into $In_xGa_{1-x}P$, resulting in a larger band-gap bowing by reducing the conduction band [67].
This Nitrogen incorporation $Ga_xIn_{1-x}P$ was studied by T. Imanishi, *et al.* [71] with 3.5% of Nitrogen, and he came up with the following energy gap dependence on Nitrogen composition as [71]:

$$E_0 = 0.20 \times 10^{-2} y^2 - 0.22y + 2.74. \tag{4.3}$$

This study also showed that with an increase in Nitrogen composition, the band-gap energy decreases. This behaviour is typical for materials like InP, GaP and GaAs, and can be represented by a quadratic function

$$\Delta E_g(x) = bx(x - 1), \tag{4.4}$$

with b as the bowing coefficient. Eq. (4.4) is represented diagrammatically in Fig. 4.2. There is, however very, isolated data in the literature about the energy gap and band structure of $In_xGa_{1-x}P_yN_{1-y}$/GaAs/GaP.

Refractive Index/Dispersion

There is an isolated study of the refractive index of $In_xGa_{1-x}P_yN_{1-y}$.
T. Imanishi *et al.* [71] examined the refractive index of $In_xGa_{1-x}P_yN_{1-y}$/GaP

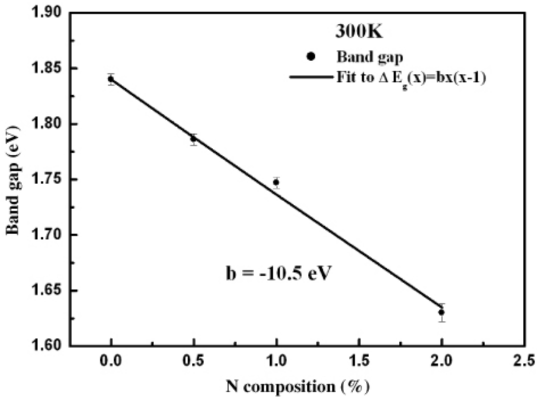

FIGURE 4.2: Band-gap of $In_xGa_{1-x}P_yN_{1-y}$/GaAs as a function of Nitrogen composition, reproduced from Y. K. Su *et al.* [69].

and displayed the results in a graphical form as seen in Fig. 4.3.

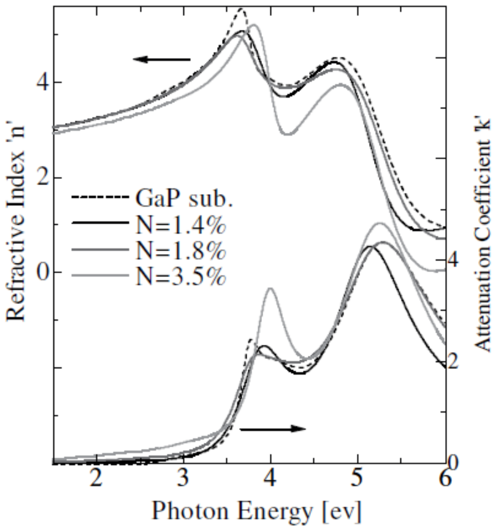

FIGURE 4.3: Refractive index of $In_xGa_{1-x}P_yN_{1-y}$/GaP as a function of Nitrogen composition, adapted from T. Imanishi *et al.* [71].

$In_xGa_{1-x}P_yN_{1-y}$ Summary

$In_xGa_{1-x}P_yN_{1-y}$ can be grown on GaP (100) and GaAs (100) using SS-MBE and GS-MBE, respectively. So far, the main application of $In_xGa_{1-x}P_yN_{1-y}$ has been in semiconductor transistors, laser and solid state lighting.

Y. Hong, *et al.* [67], studied the electron concentration and electron transport properties of $In_{0.52}Ga_{0.48}P_{1-y}N_y$/GaAs with varied Nitrogen compositions together with the temperature dependence of the direct band-gap of and described it using Varshni equation,

$$\begin{gathered} E_g(T) = E_0 - \alpha T^2/(\beta + T) \\ E_0 = 1.866\text{ eV},\ \alpha = 1\text{ meV/K},\ \beta = 1475\text{ K}, \end{gathered} \tag{4.5}$$

where E_0 is the band-gap at $T = 0$ K, the α and β are the Varshni coefficients.

T. Imanishi *et al.* [71], studied the optical properties of $\mathrm{In}_x\mathrm{Ga}_{1-x}\mathrm{P}_y\mathrm{N}_{1-y}/\mathrm{GaP}$ with varied Nitrogen concentrations between $1.4 - 9.6\%$ using photoluminescence and spectroscopic ellipsometry. Based on the peak transition energy, he found the direct-to-indirect crossover point of the band structure to be around 5% of Nitrogen concentration. Hence, $\mathrm{In}_x\mathrm{Ga}_{1-x}\mathrm{P}_y\mathrm{N}_{1-y}/\mathrm{GaP}$ has a direct band-gap structure for compositions of Nitrogen less than 5%.

$\mathrm{In}_x\mathrm{Ga}_{1-x}\mathrm{P}_y\mathrm{N}_{1-y}$ has proven to be an interesting potential material platform for opto-electrical applications, but there are several challenges associated with this envdeavour. First, direct-indirect band transition as a function of the composition of $\mathrm{In}_x\mathrm{Ga}_{1-x}\mathrm{P}_y\mathrm{N}_{1-y}$, is not well known. This could pose a limitation in the in choosing appropriate composition for different applications. Also, at this moment, it is difficult to obtain III-V-N layers because of the large difference in the length of the covalent bonds between Nitrogen and other components of the compound [71], [72]. Incorporating Nitrogen into the $\mathrm{Ga}_x\mathrm{In}_{1-x}\mathrm{P}$ compound results in improved optical properties, but also increases the fabrication defects of the material [69].

4.3.2 Aluminium Gallium Indium Phosphide

Aluminium Gallium Indium Phosphide, $\mathrm{Al}_x\mathrm{Ga}_y\mathrm{In}_{1-x-y}\mathrm{P}$, is a quaternary III-V semiconductor alloy of InGaP and InAlP with a unique property. It has the widest direct band-gap structure among the III-V materials lattice matched to a commonly available, high quality III-V substrate, GaAs [73]. With x = 0.3 and y = 0.2, the band-gap is direct with $E_g = 2.3$ eV (0.54 μm) with the lattice constant equal to that of GaAs [74]. It has a large room temperature band-gap between 1.9 eV (InGaP) and 2.5 eV (InAlP) corresponding to the band-gap equivalent wavelength of 0.65 μm (InGaP) and 0.50 μm (InAlP).

Common Use

$\mathrm{Al}_x\mathrm{Ga}_y\mathrm{In}_{1-x-y}\mathrm{P}$ has gained considerable attention in the development of high temperature and high power semiconductor devices. Its most common applications include, light emitting diode and lasers in the visible spectrum for optical storage of information [75], material absorber/optical window in solar cells [76], quantum wells [77], confinement layers and distributed Bragg reflectors (DBR) mirror stacks [78].

Substrates

$Al_xGa_yIn_{1-x-y}P$ can be grown on GaAs (100) substrate by gas-source MBE (GS-MBE) [79], metal organic vapour-phase epitaxy
(MOVPE) [80], [81], solid-source MBE (SS-MBE) [82], MOCVD [83] and MBE [74].

For material growth using MBE, InGa alloy, In, and Al were used as metallic sources. The $Al_xGa_yIn_{1-x-y}P$ layer was grown on Cr-doped semi-insulating GaAs (100) substrate, preheated to temperatures of about 600 °C under arsenic vapour pressure for 5 min, then the temperature was reduced to 550 - 580 °C for the growth on the substrate at a rate of 1 μm/h under a controlled phosphorus vapour pressure of about 1.3×10^{-6} Torr [74].

Lattice Matching

Yuan, *et al.* [73], studied the lattice matching of $Al_xGa_yIn_{1-x-y}P$ grown on GaAs substrate and found the lattice-matching compositions to satisfy the relationship

$$x + y = 0.51. \tag{4.6}$$

Adachi, *et al.* [26], later expressed the lattice matching condition for
$Al_xGa_yIn_{1-x-y}P/GaAs$ as

$$\begin{aligned} y &= 0.5158 - 0.9696x \\ &\qquad \text{for } 0 \leq x \leq 0.53. \end{aligned} \tag{4.7}$$

Surface morphology at various values of x using interference contrast microscopy shows that for $x < 0.04$, the material showed no deformation, roughness or cracks at the studied temperatures, but at higher values of x above 0.15, there was slight fine-scaled roughness in the morphology.
$Al_xGa_yIn_{1-x-y}P$ grown on GaAs showed micro-cracks at lattice mismatch around $a_e - a_s/a_s < 2 \times 10^{-3}$ [74], where a_e is the lattice constant of the film (AlGaInP) and a_s is the lattice constant of the substrate (GaAs).

Energy gap

$Al_xGa_{0.52x}In_{0.5}P$ band structure was studied extensively by Prins, *et al.* [84]. He gave the following equations for the composition dependence of the direct Γ and indirect X band-gaps:

$$E_g(\Gamma) = (1.985 + 1.22x)\ \text{eV}, \tag{4.8}$$

and

$$E_g(X) = (2.282 + 0.17x)\ \text{eV}. \tag{4.9}$$

In his study, he came up with the conclusion that the direct-indirect band-gap crossover occurs at $x \approx 0.28$. Also, for $x \geq 0.28$, the indirect conduction band minima (X) is lower than the direct conduction band minima (Γ). However, Adachi *et al.* [85] found this transition to be around $x \approx 0.63$.

Cao, *et al.*, Adachi, *et al.* [85] and Asami, *et al.* [86] also studied the band-gap structure of $(Al_xGa_{1-x})_{0.53}In_{0.47}P/GaAs$ at 300K and came up with the direct energy gap expression,

$$E_0 = 1.90 + 0.57x + 0.10x^2\ \text{eV}, \tag{4.10}$$

and indirect energy gap expression as

$$E_g^{\text{x}} = 2.25 + 0.09x - 0.01x^2\ \text{eV}. \tag{4.11}$$

Refractive Index/Dispersion

Hofenmann, *et al.* [87], studied the properties of $(Al_xGa_{1-x})_{0.53}In_{0.48}P/GaAs$ using far-infrared ellipsometry and Raman scattering. The data obtained was fitted using first-order Sellmeier equation by Adachi, *et al.* [88], resulting in a set of dispersion parameters in the transparent region, written as

$$A(x) = 5.38 + 2.16x, \tag{4.12}$$

$$B(x) = 4.01 + 3.01x, \tag{4.13}$$

$$C(x)^2 = 0.184 - 0.019x + 0.024x^2. \tag{4.14}$$

As $\lambda \rightarrow \infty$ in the first-order sellmeier equation, $n(\lambda \rightarrow \infty)^2 = \epsilon_\infty = A + B$ is obtained. Here, the unit of the parameter C is in μm, and ϵ_∞ is the high-frequency dielectric constant.

From eqs. (4.12) – (4.14), Fig. 4.4 is obtained.

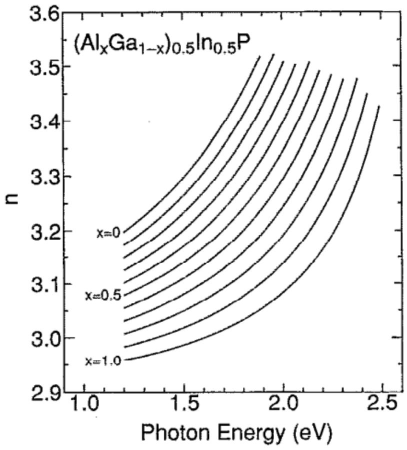

FIGURE 4.4: Refractive index of $(Al_xGa_{1-x})_{0.5}In_{0.5}P/GaAs$ as a function of aluminium composition, reproduced from Adachi, *et al.* [88]

$Al_xGa_yIn_{1-x-y}P$ Summary

$Al_xGa_yIn_{1-x-y}P$ is a unique III-V quaternary compound having the largest known direct band-gap structure, lattice-matched to GaAs amongst the III-V group of semiconductors.
It could be grown on GaAs (100) substrate using MOCVD, SS-MBE, GS-MBE, MOVPE and MBE.
So far, $Al_xGa_yIn_{1-x-y}P$ with its large band structure, would be used as an efficient light source, since it is primary use has been as a light source in the visible regime.
For the quaternary $(Al_xGa_{1-x})_{0.52}In_{0.48}P$ with $x = 0$, the ternary $Ga_{0.52}In_{0.48}P$ has a direct band-gap while for $(x-1) = 0$, $Ga_{0.52}In_{0.48}P$ has an indirect band-gap structure [82]. It exhibits a direct band-gap structure up to 2.5 eV (λ_g = 0.50 μm) and, as such, it is a good candidate for many opto-electronic applications that require shorter wavelengths. Optical, electrical and structural properties of $(Al_xGa_{1-x})_{0.52}In_{0.48}P$ have been studied extensively by Mowbray, *et al.* [82], Cheong, *et al.* [89] and Toivone, *et al.*[90].

$Al_xGa_yIn_{1-x-y}P$ is a promising material candidate with all its unique characteristics, but there are a few drawbacks to the applicability of this material. It is well known that the AlP crystal surface easily deteriorates at room temperatures due to hydrolysis [91]. However, matching the alloys of AlP with GaAs, as in the case of $Al_{0.47}Ga_{0.42}In_{0.11}P$, showed no degradation in the surface that depicts the possibility of hydrolysis [74]. This study however did not account for the oxidation of $Al_xGa_yIn_{1-x-y}P$, since Al is known to oxidize at high concentrations [25]. Also, the dependence of the electronic band structure of $Al_xGa_yIn_{1-x-y}P$ on the material composition is still not fully understood. Most recent direct-indirect transition is reported to occur at $x \approx 0.63$, when the composition of Indium (y) was fixed at 0.48, *i.e.*, $(Al_xGa_{1-x})_{0.52}In_{0.48}P$, the direct-indirect transition was observed at $x \approx 0.5$ [82]. This makes full functionality and applicability of this material limited to very few known compositions as the transition between the direct to indirect band is not fully known.

4.3.3 Aluminium Gallium Nitride

Aluminium Gallium Nitride, $Al_xGa_{1-x}N$, is a ternary alloy of GaN and AlN. It has a similar structure as both its constituent alloys, the wurtzite (WZ) structure, the zinc blende (ZB) structure and a rock-salt structure, with the WZ structure being the most stable at room temperature and pressure.

$Al_xGa_{1-x}N$ also inherits its direct band-gap structure from both alloys, as GaN and AlN are both direct band-gap materials. A variety of III-Nitrides materials have been studied for applications from visible to infrared spectra. Numerous applications stand to benefit from its very wide band-gap (from 3.44 eV for GaN to ≈ 6.28 eV for AlN, corresponding to equivalent wavelengths from 361.5 nm to 200 nm).

Common Use

GaN, AlN, and their alloys gained a lot of interest in the development of high power, high temperature and surface acoustic wave applications, water sterilization [92], bio-agent detection and analysis [93], solid-state lighting [94], short-range communications, and lithography. These material and their alloys are also of interest in the design of opto-electronic devices in blue and ultraviolet spectral regions, because of the possibility of controlling their band gap. The III-nitrides alloys have proven to be a robust set of materials in development of blue/green LEDs and violet lasers. Among these alloys is $Al_xGa_{1-x}N$, which holds great promise in the development of ultraviolet photodetectors [95] with its wide band gap suitable to minimize the dark, current thereby increasing the sensitivity of the detectors [96]. Cubic $Al_xGa_{1-x}N$ alloys can form heterostructures with the cubic GaN, which makes them most suitable as materials for cladding layers in optical devices [97] and building block for quantum dot fabrication [98]. Based on the non-centrosymmetric crystal structure of WZ $Al_xGa_{1-x}N$, passive nonlinear optical devices such as optical limiters, ultra-fast nonlinear auto-correlation systems and all-optical switching hold bright prospects.

Substrates

The cubic $Al_xGa_{1-x}N$ alloy films can be grown on GaAs (001) or 3C-SiC (001) by molecular beam epitaxy (MBE) using metallic III-group element sources (Al and Ga, and a RF-N_2 plasma). The structure consisted of a buffer layer grown at 500 °C, a cubic GaN or AlN layer grown at 800 – 900 °C, and a cubic $Al_xGa_{1-x}N$ layer grown at 800 – 1000 °C. The growth rate was around 500 nm/h, and the thickness of the epitaxial layer was around 800 – 1000 nm [97].

Epitaxial films of $Al_xGa_{1-x}N$ can also be grown on c-plane sapphire (0001) substrate by MOCVD, with low temperature AlN buffer layers [99] or by plasma-assisted molecular beam epitaxy (PAMBE) with Al molar fraction x varied in approximate equidistant steps between $0 < x < 1$ using Al and Ga effusion cells and a rf-plasma source. The films were nominally undoped and grown without a buffer layer at temperatures around 800 – 1000 °C. The thickness of the film was $\approx 1\ \mu$m with the growth rate around 0.5 - 0.6 μm/hr with root mean square (rms) surface roughness between 5 and 15 nm obtained by atomic force microscopy [100].

$Al_xGa_{1-x}N$ nanowires can be grown on GaN by catalyst-free, PA-MBE on Si(111) substrate under a N-rich environment with no AlN thin buffer layer grown, resulting in a thin wire density of about 500 - 700 μm^{-2}.
The $Al_xGa_{1-x}N$ sections were 200 - 300 nm in length and single nominal Al composition (x_{Al}) grown on top of the GaN [98].

Lattice Matching

Zhang *et al.* [101] evaluated the lattice constant of $Al_xGa_{1-x}N$ using three sets of samples. These samples were only different in their buffer configurations. The samples were, $Al_{0.2}Ga_{0.8}N$/AIN superlattice (to reduce the strain on the substrate), a 25-nm-thick, low temperature AIN buffer before the $Al_{0.2}Ga_{0.8}N$ deposition, and a 40-nm-thick, high temperature AIN buffer before $Al_{0.2}Ga_{0.8}N$ deposition. All layers grown on basal plane sapphire substrate using low-pressure MOCVD were deposited and grown. Results showed an average lattice constant, $a = 3.1482$ for the superlattice structure, $c = 5.1362$ for low temperature sample, and $a = 3.1736$ for high-temperature sample. Strain engineering and temperature effect on the structure was also studied by Zhang *et al.* [101], [102].

Sohi *et al.* [102], also studied the lattice mismatch of as a function of GaN layer thickness. Fig. 4.5 shows the lattice-mismatch percentages as a function

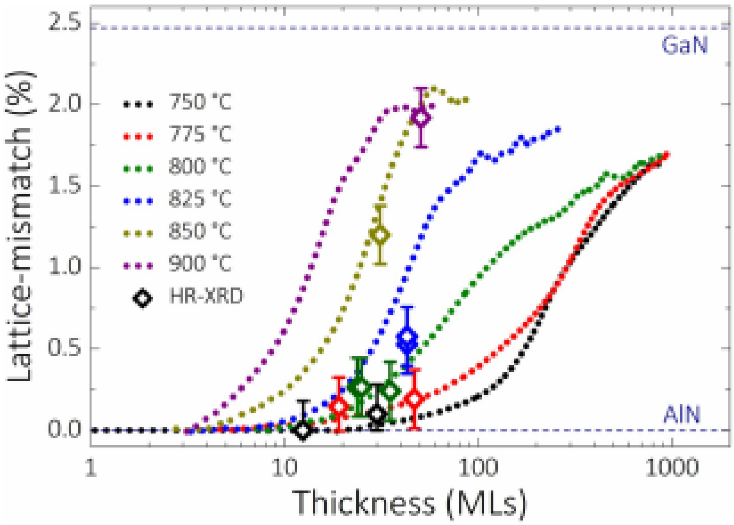

FIGURE 4.5: Lattice mismatch as a function of GaN layer thickness, adapted from Sohi *et al.* [103].

of GaN layer thickness. It could be seen that, as the thickness of GaN buffer layer is increased, the lattice mismatch increases with a negligible residual compressive strain of -0.04% [102]. However, Khan *et al.* [104], found the lattice-mismatch of the AlN buffer layer and the GaN later to be 3%.

Energy gap

The alloy energy gap can be estimated using the following relation [98]:

$$\begin{gathered} E_g(\mathrm{Al}_x\mathrm{Ga}_{1-x}\mathrm{N}) = xE_g(\mathrm{AlN} + (1-x)E_g(\mathrm{GaN}) + bx(1-x), \\ \text{where } b = 1\mathrm{eV}, E_{\mathrm{DX(AlN)}} = 6.03\mathrm{eV}, E_{\mathrm{DX(GaN)}} = 3.473\mathrm{eV}. \end{gathered} \tag{4.15}$$

Here E_g is the band-gap energy, x is the molar concentration of Aluminium, E_{DX} is the direct band-gap energy and b is the bowing parameter.

Fig.4.6 shows the band-gap energy and equivalent wavelength (right hand scale), plotted against the lattice constant of $\mathrm{Al}_x\mathrm{Ga}_{1-x}\mathrm{N}$ and $\mathrm{Al}_x\mathrm{In}_{1-x}\mathrm{N}$, and their constituent alloys. The lines are a representation of the bounds of the parameter space for the both ternary compounds.As mentioned earlier, lattice matched compounds lie on vertical line of this plot. By selecting the composition of AlN (Ga = 0) or GaN (Al = 0), one would select the appropriate

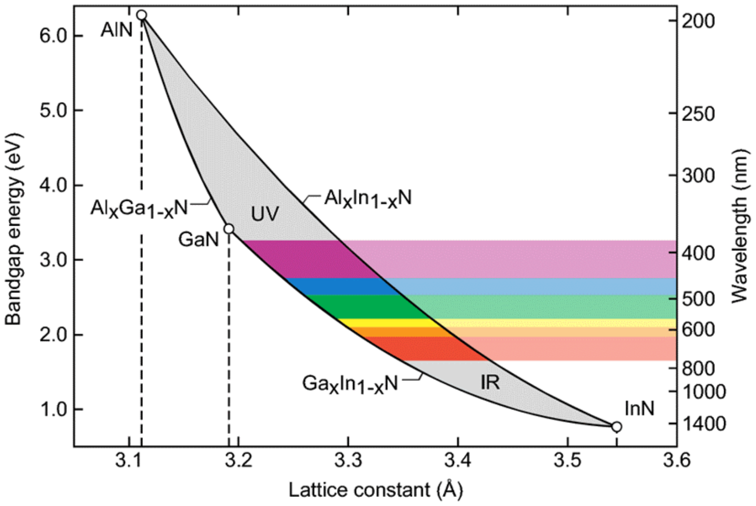

FIGURE 4.6: Band-gap energy and equivalent wavelength against lattice constant of AlGaN and its alloys [103]

operation wavelength as well as the lattice constant of $Al_xGa_{1-x}N$, matched with the appropriate substrate. GaN or AlN can be used as substrate, with preference to a cladding layer made with a material with refractive index closer to that of GaN to layer made with AlN.

Refractive Index/Dispersion

The refractive index of cubic $Al_xGa_{1-x}N$ grown on GaAs (001) by MBE was found to decrease with increasing Al content, as expected from the empirical observation that the refractive index decreases with increasing direct band-gap energy.
The refractive indices of $Al_xGa_{1-x}N$ at 400 nm can be expressed as a function of Al content [97] as

$$n(x) = 2.61 - 0.88x + 0.364x^2. \tag{4.16}$$

At 1550 nm, the refractive index of $Al_xGa_{1-x}N$ can also be expressed as [105]

$$n(x) = 2.335 - 0.735x + 0.431x^2. \tag{4.17}$$

Fig. 4.7 (a) shows the refractive index of $Al_xGa_{1-x}N$ as a function of photon energy at room temperature with different aluminium concentrations. Here, at higher concentration, the refractive index is seen to decrease exponentially with decreasing photon energy. For cubic $Al_xGa_{1-x}N$, the refractive index with lower Al contents are somewhat larger than those of hexagonal

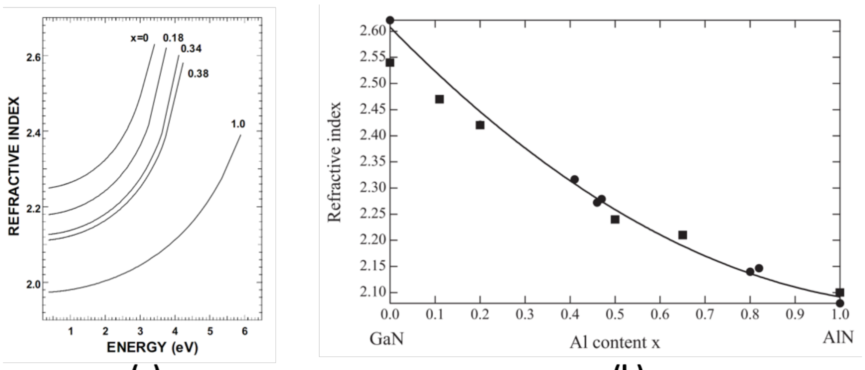

(a) (b)

FIGURE 4.7: Refractive index of $Al_xGa_{1-x}N$ below band-gap plotted against (a) Photon energy at room temperature, adapted from J. F. Muth *et al.* [103], (b) Aluminium concentration for cubic (circle dots) and hexagonal (square dots) $Al_xGa_{1-x}N$ structures in the visible wavelength regime, adapted from Takanobu Suzuki *et al.* [97].

$Al_xGa_{1-x}N$ resulting in the cubic $Al_xGa_{1-x}N$ having a smaller direct band-gap energy. However, with the increase in Al content, the refractive index of cubic $Al_xGa_{1-x}N$ is almost equal to those of the hexagonal $Al_xGa_{1-x}N$, [see Fig.4.7 (b)].

$Al_xGa_{1-x}N$ Summary

$Al_xGa_{1-x}N$ could be grown on GaAs (001) by MBE using metallic sources (Al, Ga, and a RF-N_2 plasma), on *c*-plane Sapphire (0001) by MOCVD with low temperature AlN buffer layers, GaN by catalyst-free PA-MBE with N-rich environment.

The wide band-gap of $Al_xGa_{1-x}N$ makes it ideal for high temperature operation devices. So far, the most popular application of $Al_xGa_{1-x}N$ is light emission in UV/blue wavelength regions. Its application for optical emission in infrared have been investigated by exploring the effect of inter-subband transitions in $Al_xGa_{1-x}N$/GaN multiple quantum well structures, nanowires and even planar optical waveguides [98].
Optical emission in the $Al_xGa_{1-x}N$/GaN waveguide has been demonstrated in UV wavelength regions by carrier injection [105].
However, in infrared, which is far from the material band-gap (λ_g = 361.5 nm - 200 nm), both optical gain and absorption in $Al_xGa_{1-x}N$/GaN waveguide are expected to be negligible, making the material essentially transparent in the optical communication wavelength range around 1550 nm. Because of the sub-nanosecond carrier lifetime in GaN and $Al_xGa_{1-x}N$, optical packet

switching in AWGs could be made possible [105].
The optical properties of $Al_xGa_{1-x}N$ alloy are studied extensively by Takeuchi, *et al.* [106], P. Wisniewski, *et al.* [107] and K. Nam, *et al.* [107]. Dielectric functions, Phonon and coupled modes are studied extensively by Hu G., *et al.* [108]. Second-order nonlinear optical processes including second-harmonic generation, optical rectification, and difference-frequency generation associated with inter-subband transitions in wurtzite $Al_xGa_{1-x}N$/GaN quantum wells were investigated theoretically by Angsheng Liu, *et al.* [109]. Submicron waveguides based on $Al_xGa_{1-x}N$/GaN multiple quantum wells (MQW) grown by MOCVD were investigated by S. Keller, *et al.*. [110]. Different waveguide configurations (single mode, straight and 2 × 2 couplers) with GaN core and $Al_xGa_{1-x}N$ cladding grown on sapphire are studied extensively by T. Order *et al.*. [111].
Hui *et al*, [105], reported that $Al_xGa_{1-x}N$/GaN showed birefringence in a single-mode optical waveguide operating at 1550 nm. The refractive index $Al_xGa_{1-x}N$/GaN not only showed dependence on the polarization of the signal (perpendicular or parallel to the *c*-plane), but also depended on the direction of the optical propagation in the *a*-*b* plane. Fig. 4.8 (b) shows the cross section of the single-mode (at $\lambda > 1.1$ μm), optical waveguide with GaN as the core layer, $Al_xGa_{1-x}N$ as the cladding and sapphire as the substrate.

$Al_xGa_{1-x}N$ demonstrates potential in achieving a functional optical waveguide device in the in telecommunication wavelength region, however, some challenges exist. When using GaN as a guiding layer [111], the refractive index contrast Δn is very large: $\Delta n \approx 0.6$ with sapphire and $\Delta n \approx 1.4$ with air at visible wavelengths. This index contrasts give high confinements but they are also known to cause high propagation losses, as a result of the propagating light scattering at the interfaces, which is one of the main contributions to the optical losses in waveguides. The use of cladding layers with a refractive index closer to that of GaN would be preferred in order to minimize the losses. AlN, or more preferably, the alloy $Al_xGa_{1-x}N$ in which the refractive index can be adjusted by varying the Al concentration x, should be considered instead of using GaN or AlN as the guiding layer [111], [see Fig.4.7 (b)].

At present, it is also difficult to grow the thick $Al_xGa_{1-x}N$ cladding layers required for optical confinement due to the formation of cracks. The stress introduced in the $Al_xGa_{1-x}N$ cladding layers due to the lattice mismatch, and the difference in thermal expansion coefficients of the $Al_xGa_{1-x}N$ cladding

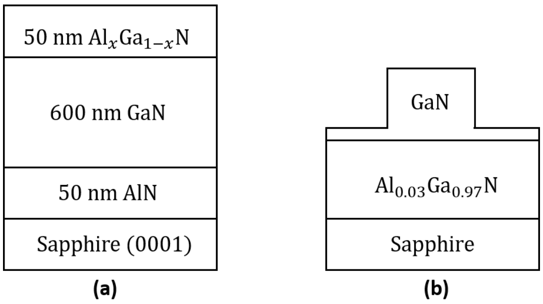

FIGURE 4.8: (a) $Al_xGa_{1-x}N$-GaN heterostructure, reproduced from Khan *et al.* [104], (b) Cross section of GaN-$Al_xGa_{1-x}N$/Sapphire waveguide, reproduced from Hui *et al.* [105].

layers and GaN results in poor-quality materials. Thick $Al_xGa_{1-x}N$ layers can be grown over GaN buffers, but this buffer layer drastically decreases efficient light extraction in deep-UV emitters resulting from strong absorption [112]. Due to the complication in the growth of this material, thin buffer layer of AlN and a thick GaN layer is grown in-between the sapphire substrate and the $Al_xGa_{1-x}N$ layer, [see Fig. 4.8 (a)]. This was done to control the dislocation density and lattice-mismatch between the $Al_xGa_{1-x}N$ and the sapphire substrate.

Structurally, with $Al_xGa_{1-x}N$ lattice matched to GaN, the layer quality decreases with an increase in the Al content, leading to surface imperfections, roughness and cracks. This degradation in the crystalline quality becomes even stronger for $x \geq 0.5$, which in part explains why there isn't any data in literature on $Al_xGa_{1-x}N$ with more than 50% of Al. These surface imperfections are due to the differences in surface mobility of the reactants, optimized growth temperature for GaN, but not for AlN, and also the lattice mismatch between $Al_xGa_{1-x}N$ and GaN base layer for $Al_xGa_{1-x}N$/GaN heterostructure [95].

4.4 Conclusions

This chapter began by detailing the required material properties for selecting a potentially efficient material candidate for nonlinear integrated photonics-on-a-chip. Various properties of these materials have been reported in a concise manner, detailing the current applications, substrates for growth, the growth process, and some of their optical and electronic properties. Also, challenges associated with the growths were briefly discussed.

$In_xGa_{1-x}P_yN_{1-y}$ has gained much attention in the past decade as an excellent material for transistors and light emitting diodes due to its strong photoluminescence as electroluminescence, which is as a result of Nitrogen incorporation. So far, its primary application is in solid-state lighting. In integrated optics, $In_xGa_{1-x}P_yN_{1-y}$ would be used an an efficient light source, but it has not yet been explored for potential applications in integrated optics. Only very isolated studies of the properties of this material has been performed. However, at this moment, not much is known about this material in terms of its integrated optical applications. This is because, studies related to the direct-to-indirect band-gap transition as a function of the material compositions, has been inclusive, with studies showing different cross-over points for similar or the same material composition. This in essence, poses another difficulty in the growing defect-free III-V-N layers as a result of the large difference in the length of the covalent bonds between Nitrogen and the other composition of the compound.

$Al_xGa_yIn_{1-x-y}P$ has the widest direct band-gap structure (1.9 eV to 2.5 eV), known to be lattice-matched with a high quality, commonly available III-V substrate, GaAs. It is mostly used in the development of high power and high temperature semiconductor devices such as, LEDs and lasers in the visible spectrum, with primary application in optical storage of information. This material, though not yet explored for potential applications in integrated optics, would also be used as an efficient light source. Its GaAs substrate makes it a very interesting candidate as it has a very small lattice-mismatch. Optical properties of $Al_xGa_yIn_{1-x-y}P$ has been studied extensively. However, just like $In_xGa_{1-x}P_yN_{1-y}$, the direct-to-indirect band-gap cross-over point as a function of material composition, is not fully understood. These studies show that $Al_xGa_yIn_{1-x-y}P$ is not subject to deterioration due to hydrolysis, as it is with its constituent alloy, AlP. This studies does not however, account for the material degradation from oxidation as a function of Al composition, since Al is known to oxidize at high concentrations.

$Al_xGa_{1-x}N$, with its wide band-gap (3.44 eV to 6.28 eV), makes it ideal for light emission in the UV/blue wavelength region. It is also suitable for devices requiring high temperature operation. In integrated optics, it would be used as an efficient light source. Several structures based on this material have been studied. The optical and electronic properties of $Al_xGa_{1-x}N$ including but not limited to, second-order nonlinear processes (SHG) in QW, and sub-micron waveguides, birefringence and nonlinear absorption, have

TABLE 4.1: Table showing potential III-V material candidates, their substrate, energy gap and their refractive indices.

Material	**Substrate**	x	y	**Band-gap Type**	E_g **(eV)**	λ(μ**m)**	$n_{\min}$	$n_{\max}$	**Ref**
$In_xGa_{1-x}P_yN_{1-y}$	GaAs	0	0	I	2.20	0.56	3.00	3.13	[113]
		1	0	I			2.36	3.12	
	GaP	0.51	1	D	1.85	0.67	3.61		[26]
$Al_xGa_yIn_{1-x-y}P$	GaAs	0	0.51	D	1.90	0.65	3.13	3.78	[26]
		0.53	0	I	2.33	0.53	2.92	3.75	
$Al_xGa_{1-x}N$	Sapphire	0	-	D	3.23	0.38	2.35	2.77	[26]
		1	-	D	5.20	0.24	2.04	2.27	
	GaAs	0	-	D	3.42	0.36			[26]
		1	-	D	6.20	0.20			
	GaN								
$Ga_xIn_{1-x}P$	GaAs	0	-	D	1.35	0.92			[26]
		1	-	D	2.76	0.45	3.05	4.54	

D - Direct band-gap, I - Indirect band-gap,
E_g – energy gap,
$n_{\min}$ and $n_{\max}$ are minimum and maximum refractive indices respectively, as found in literature.

been performed. $Al_xGa_{1-x}N$ shows great potential in for use in integrated optics, but this endeavour is faced with multiple challenges. First, it is difficult to grow thick layers of $l_xGa_{1-x}N$ without using the buffer layers. This is due to the large lattice-mismatch and the difference in the thermal expansion coefficient of $Al_xGa_{1-x}N$ and its constituent alloys. These buffer layers drastically reduces the light extraction as a result of strong absorption.
Secondly, when using GaN as the guiding layer, there is a very large refractive index contrast between substrate-air interface and the core-substrate interface. Though this index contrast is needed for high confinements, but it is also associated with high propagation losses as a result of the propagating light scattering at the interfaces.
With the more attention to the lattice-mismatch, choosing sapphire instead of GaAs or GaN as the cladding, one would have to choose the composition of Al such that, the guiding layer has a refractive index closer to that of GaN instead of AlN.

Table 4.1 shows the summary of these identified promising materials, specifying their energy gaps and their corresponding band-gap equivalent wavelengths for a given material composition to which the material can have either a direct (D) or indirect (I) band structure. With this table, one can have a broad overview of all the materials considered in this thesis.

Chapter 5

Conclusion

5.1 Conclusion

This masters thesis was motivated by the importance of the applications of integrated optics in providing viable solutions to filling several technological gaps in the fields of optics and electronics. Being able to monolithically integrate both active and passive devices on the same chip could be of benefit to several applications and processes. Applications like nonlinear wavelength conversion is necessary to extend the operation range of the current integrated laser sources, and for all-optical signal processing which would solve the fundamental bottleneck of electronic signal processing. Hence, exploring the optical nonlinearity in III-V semiconductors is of great importance in quest of finding a suitable and efficient material platform for this monolithic integration.

Presented in this thesis, is a detailed result on the exploit of ternary and quaternary III-V semiconductor materials for potential applications in integrated optics.
As a starting point, optical characterization of Aluminium Gallium Arsenide (AlGaAs) waveguides with enhanced nonlinear interactions was carried out. We have demonstrated experimentally, an efficient and tuneable four-wave mixing at different wavelength ranges with three different waveguide geometries. There are trade-offs unique to each geometry that could be advantageous in different applications. These studies show a higher four-wave mixing conversion efficiency, with increased conversion range for strip-loaded, nanowire and the half-core geometries than previously reported studies, as detailed in Chapter 2. Both linear and nonlinear loss measurements are also presented for all three geometries that were studied. As a complementary

effort, we have included a concise review of the AlGaAs waveguide design parameterization as was performed by K. Awan [28].

AlGaAs is one of the most widely studied materials in the III-V group of semiconductors, but there exist a large number of unexplored materials in the same group with promising properties. Waveguides are the building blocks of integrated photonic devices, and the exploration of potential material candidates can be performed by building waveguides with ternary and quaternary III-V semiconductor materials, and assessing their performance. To succeed in this endeavour, several material properties would have to be readily available. Intrinsic material properties like energy gap and refractive index of these ternary and quaternary III-V materials are only available for few binary compounds in very isolated spectral window. Hence, there is need for a precise inter-relationship between these intrinsic properties. By interpolation, the properties of these ternary and quaternary III-V materials could be obtained from the individual elemental and binary compositions. Several propositions have been made to predict different material properties from other intrinsic properties, as detailed in Section 3.2. To take this effort further, we have developed a model capable of interrelating the refractive indices of binary, ternary and quaternary III-V semiconductor materials to their band-gap energies. We have compared this model with existing experimental data and other known models and found that our model is in good agreement with the known experimental values, and also presents the lowest margin of error amongst the existing models. This tool is uniquely important as it tries to bridge the gap between the available data in the literature with respect to the design of integrated optical devices with ternary and quaternary III-V semiconductor compounds.

As a final step, we have identified other potential III-V material candidates for integrated optics at different wavelength ranges. These candidates were chosen based on several criteria as detailed in Section 4.2. The properties of each of these materials are provided in a concise manner. This includes their advantages and potential strongholds in the adoption of each candidate as a potential material platform for integrated photonics.

5.2 Future Work

In this thesis, we have investigated the optical interactions in AlGaAs waveguides of three different geometries. It was observed that the cumulative effect of the nonlinear absorption depends on the waveguide geometry, and this absorption is stronger for the waveguides with tighter mode confinement. While the nonlinear absorption coefficients α_2 and α_3 represent material parameters, there is an uncertainty about the material compositions for which these values are obtained. Due to the limited time frame of this program, this material composition relationship of the nonlinear absorption coefficients α_2 and α_3 could not be performed. As this is a very important material parameter, the next step would be to perform a detailed study of this relationship for each waveguide geometry in order to fully characterize this material. The concepts and approaches presented in this thesis have made a clear path into this study.

Although our model relating the refractive index of ternary and quaternary III-V materials to their band-gap energies, presents excellent results when compared with other existing results, it is still missing a fundamental physical explanation for this exponential dependence on the energy-gap of the material. Also, since refractive index is a material property that is a function of several other quantities, our model does not account for the variation in wavelength of the interacting light. Incorporating dispersion into our model would ultimately make our model a very powerful tool for predicting material properties in the design of integrated waveguide structures. The next step in this endeavour would be to find a physical explanation for this exponential dependence and incorporate dispersion into the model. One idea comes to mind, exploring the Lorentz oscillator (with one resonance) and Wemple-DiDomenico models would present refractive index dispersion for photon energies below the band-gap (no absorption). This dispersion is quantified as a measure of the strength of the inter-band optical transitions in the material.

This master's thesis presents a repeatable and reliable exploration of the optical nonlinearities in III-V semiconductor materials with both practical and analytical approaches.

Appendix A

Appendix A

TABLE A.1: Table showing experimental energy gaps and refractive indices of some known semiconductor materials, with their values from different models.

Material	$^{\star,\dagger}E_g$ **(eV)**	**Refractive Index (n)**								
		$^{\diamond,\star,\dagger}$**Exp.**	**Moss**	**Ravindra**	**Reddy**	**Herve**	**Kumar**	**Ahmad**	**Tripathy**	**Proposed Model**
Si	1.10	3.46	3.0485	3.4020	3.8057	3.1395	3.2649	3.4200	3.5279	3.4266
Ge	0.67	4.00	3.4507	3.6686	4.7417	3.4339	3.8309	4.0345	3.9995	3.6019
ZnO	3.70	1.92	2.2510	1.7900	2.6076	2.1443	2.2081	2.2825	2.1652	2.5345
ZnS	3.54	2.27	2.2760	1.8892	2.6398	2.1826	2.2398	2.3164	2.2053	2.5819
ZnSe	2.58	2.43	2.4633	2.4844	2.8885	2.4603	2.4803	2.5740	2.5342	2.8861
ZnTe	2.26	2.70	2.5463	2.6828	3.0034	2.5755	2.5885	2.6902	2.6875	2.9952
CdO	2.50	2.32	2.4828	2.5340	2.9151	2.4879	2.5056	2.6012	2.5701	2.9130
CdS	2.40	2.38	2.5083	2.5960	2.9503	2.5235	2.5388	2.6368	2.6172	2.9470
CdSe	1.70	2.49	2.7341	3.0300	3.2782	2.8142	2.8374	2.9580	3.0284	3.1963
CdTe	1.44	2.70	2.8500	3.1912	3.4606	2.9448	2.9933	3.1263	3.2252	3.2941
HgSe	2.12	2.72	2.5873	2.7696	3.0615	2.6304	2.6424	2.7481	2.7633	3.0443
Cud	3.31	2.19	2.3146	2.0318	2.6899	2.2413	2.2888	2.3689	2.2694	2.6518
CuBr	2.91	2.12	2.3903	2.2798	2.7899	2.3546	2.3859	2.4728	2.4015	2.7777
Cul	2.95	2.346	2.3822	2.2550	2.7790	2.3425	2.3754	2.4616	2.3870	2.7648
Agl	2.22	2.22	2.5577	2.7076	3.0194	2.5909	2.6034	2.7062	2.7086	3.0092
BN	4.60	2.10	2.1318	1.2320	2.4564	1.9596	2.0584	2.1227	1.9941	2.2832

Table A.1 continued from previous page

Material	$^\star E_g$ (eV)	Refractive Index (n)								
		*Exp.	**Moss**	**Ravindra**	**Reddy**	**Herve**	**Kumar**	**Ahmad**	**Tripathy**	**Proposed Model**
AIN	3.80	2.16	2.2361	1.7280	2.5884	2.1212	2.1892	2.2623	2.1418	2.5052
AIP	3.00	2.75	2.3722	2.2240	2.7658	2.3278	2.3625	2.4478	2.3693	2.7488
AlAs	2.16	3.00	2.5752	2.7448	3.0443	2.6144	2.6265	2.7311	2.7411	3.0302
AISb	1.60	3.19	2.7759	3.0920	3.3427	2.8628	2.8934	3.0184	3.1008	3.2335
GaN	3.25	2.40	2.3252	2.0690	2.7038	2.2574	2.3023	2.3834	2.2874	2.6703
GaP	2.24	2.90	2.5519	2.6952	3.0113	2.5832	2.5959	2.6982	2.6980	3.0022
GaAs	1.35	3.30	2.8963	3.2470	3.5371	2.9935	3.0563	3.1943	3.3000	3.3287
GaSb	0.81	3.79	3.2909	3.5818	4.3144	3.3312	3.6035	3.7872	3.8338	3.5439
InP	1.27	3.10	2.9409	3.2966	3.6128	3.0385	3.1171	3.2600	3.3696	3.3597
InAs	0.36	3.50	4.0305	3.8608	NA	3.6890	4.6804	4.9627	4.4140	3.7338
InSb	0.18	3.95	4.7931	3.9724	NA	3.8579	5.8525	6.2526	4.6885	3.8126
SiC	3.10	2.59	2.3528	2.1620	2.7401	2.2989	2.3377	2.4212	2.3352	2.7171
PbSe	0.29	4.69	4.2543	3.9042	NA	3.7527	5.0183	5.3336	4.5176	3.7642
PbTe	0.32	5.73	4.1509	3.8856	NA	3.7251	4.8615	5.1614	4.4727	3.7511
$CuAIS_2$	3.50	2.40	2.2825	1.9140	2.6482	2.1925	2.2480	2.3252	2.2159	2.5939
$CuAISe_2$	2.70	2.60	2.4355	2.4100	2.8506	2.4204	2.4442	2.5353	2.4832	2.8462
$CuAITe_2$	2.06	3.30	2.6059	2.8068	3.0883	2.6548	2.6670	2.7746	2.7976	3.0655
$CuGaS_2$	2.40	2.67	2.5083	2.5960	2.9503	2.5235	2.5388	2.6368	2.6172	2.9470

Table A.1 continued from previous page

Material	$^\star E_g$ (eV)	Refractive Index (n)								
		*Exp.	**Moss**	**Ravindra**	**Reddy**	**Herve**	**Kumar**	**Ahmad**	**Tripathy**	**Proposed Model**
CuGaSe$_2$	1.70	2.80	2.7341	3.0300	3.2782	2.8142	2.8374	2.9580	3.0284	3.1963
CuGaTe$_2$	1.00	3.30	3.1220	3.4640	3.9474	3.2026	3.3668	3.5303	3.6280	3.4666
CuInS$_2$	1.50	2.60	2.8210	3.1540	3.4140	2.9134	2.9542	3.0840	3.1773	3.2713
CuInSe$_2$	1.04	2.90	3.0915	3.4392	3.8876	3.1770	3.3245	3.4845	3.5873	3.4506
CuInTe$_2$	0.95	3.40	3.1623	3.4950	4.0292	3.2353	3.4229	3.5912	3.6802	3.4868
AgAIS$_2$	3.13	-	2.3472	2.1434	2.7327	2.2904	2.3304	2.4134	2.3253	2.7077
AgAISe$_2$	2.55	-	2.4706	2.5030	2.8983	2.4706	2.4896	2.5841	2.5475	2.8961
AgAITe$_2$	2.27	-	2.5435	2.6766	2.9994	2.5717	2.5848	2.6862	2.6823	2.9918
AgGaS$_2$	2.70	2.40	2.4355	2.4100	2.8506	2.4204	2.4442	2.5353	2.4832	2.8462
AgGaSe$_2$	1.80	2.80	2.6953	2.9680	3.2196	2.7676	2.7855	2.9022	2.9597	3.1594
AgGaTe$_2$	1.10	3.30	3.0485	3.4020	3.8057	3.1395	3.2649	3.4200	3.5279	3.4266
AgInS$_2$	2.00	2.50	2.6253	2.8440	3.1162	2.6799	2.6925	2.8020	2.8330	3.0869
AgInSe$_2$	1.24	-	2.9585	3.3152	3.6434	3.0557	3.1412	3.2861	3.3965	3.3714
AgInTe$_2$	1.00	3.40	3.1220	3.4640	3.9474	3.2026	3.3668	3.5303	3.6280	3.4666
ZnSiP$_2$	2.10	3.10	2.5934	2.7820	3.0703	2.6385	2.6505	2.7568	2.7746	3.0513
ZnSiAI$_2$	1.70	3.10	2.7341	3.0300	3.2782	2.8142	2.8374	2.9580	3.0284	3.1963
ZnGeP$_2$	1.99	3.10	2.6286	2.8502	3.1210	2.6841	2.6969	2.8067	2.8390	3.0905
ZnGeAs$_2$	1.15	3.50	3.0148	3.3710	3.7436	3.1089	3.2184	3.3697	3.4798	3.4068

Table A.1 continued from previous page

Material	${}^{\star}E_g$ **(eV)**	**Refractive Index (n)**								
		***Exp.**	**Moss**	**Ravindra**	**Reddy**	**Herve**	**Kumar**	**Ahmad**	**Tripathy**	**Proposed Model**
$ZnSnP_2$	1.66	2.90	2.7505	3.0548	3.3032	2.8334	2.8592	2.9816	3.0569	3.2111
$CdSiAs_2$	1.55	3.50	2.7980	3.1230	3.3774	2.8878	2.9231	3.0505	3.1385	3.2524
$CdSiP_2$	2.45	3.10	2.4954	2.5650	2.9325	2.5055	2.5220	2.6188	2.5933	2.9299
$CdGeP_2$	1.72	3.30	2.7261	3.0176	3.2661	2.8047	2.8267	2.9465	3.0143	3.1888
$CdSnAs_2$	0.26	3.70	4.3721	3.9228	NA	3.7808	5.1981	5.5313	4.5632	3.7773
$CdSnP_2$	1.17	3.10	3.0018	3.3586	3.7201	3.0969	3.2006	3.3503	3.4610	3.3989
$CulnSnSe_4$	0.71	-	3.4011	3.6438	4.5978	3.4038	3.7599	3.9573	3.9508	3.5852
$AgInSnSe_4$	0.94	-	3.1707	3.5012	4.0466	3.2420	3.4346	3.6039	3.6907	3.4908
$CuInGeSe_4$	1.26	-	2.9467	3.3028	3.6229	3.0442	3.1250	3.2686	3.3785	3.3636
$CuGaSnSe_4$	1.42	-	2.8600	3.2036	3.4769	2.9555	3.0069	3.1409	3.2415	3.3018
$AgInSeSe_4$	1.58	-	2.7846	3.1044	3.3563	2.8727	2.9051	3.0311	3.1158	3.2411
$AgGaSnSe_4$	1.70	-	2.7341	3.0300	3.2782	2.8142	2.8374	2.9580	3.0284	3.1963
$AgGaGeSe_4$	1.85	-	2.6769	2.9370	3.1921	2.7450	2.7610	2.8758	2.9267	3.1411
$AgAISnSe_4$	1.85	-	2.6769	2.9370	3.1921	2.7450	2.7610	2.8758	2.9267	3.1411
$CuGaGeSe_4$	1.87	-	2.6697	2.9246	3.1814	2.7361	2.7515	2.8655	2.9138	3.1338
$CuAlSnSe_4$	1.90	-	2.6591	2.9060	3.1658	2.7229	2.7374	2.8504	2.8947	3.1230
$AgAlGeSe_4$	2.02	-	2.6187	2.8316	3.1068	2.6715	2.6839	2.7928	2.8211	3.0798
$CuAlGeSe_4$	2.25	-	2.5491	2.6890	3.0073	2.5794	2.5922	2.6942	2.6927	2.9987

Table A.1 continued from previous page

Material	$^\star E_g$ **(eV)**	**Refractive Index (n)**								
		***Exp.**	**Moss**	**Ravindra**	**Reddy**	**Herve**	**Kumar**	**Ahmad**	**Tripathy**	**Proposed Model**
$Pb_xSn_{1-x}Te$	0.32	5.73	4.1509	3.8856	NA	3.7251	4.8615	5.1614	4.4727	3.7511
PbTe										
$Pb_{0.8}Sn_{0.2}Te$	0.12	6.58	5.3044	4.0096	NA	3.9181	6.6699	7.1574	4.7861	3.8392
$Pb_{0.94}Sn_{0.06}Te$	0.16	6.23	4.9363	3.9848	NA	3.8777	6.0790	6.5030	4.7207	3.8214
SnTe	0.18	6.70	4.7931	3.9724	NA	3.8579	5.8525	6.2526	4.6885	3.8126
$Pb_xSn_{1-x}Se$ (PbSe)	0.29	4.69	4.2543	3.9042	NA	3.7527	5.0183	5.3336	4.5176	3.7642
$Pb_{0.9}Sn_{0.1}Se$	0.18	5.52	4.7931	3.9724	NA	3.8579	5.8525	6.2526	4.6885	3.8126
$Pb_{0.88}Sn_{0.12S}e$	0.16	5.74	4.9363	3.9848	NA	3.8777	6.0790	6.5030	4.7207	3.8214
$Ga_xAl_{1-x}As$	2.585	2.97	2.4622	2.4813	2.8868	2.4586	2.4787	2.5724	2.5320	2.8844
$Ga_{0.2}Al_{0.8}As$										
$Ga_{0.6}Al_{0.4}As$	1.945	3.12	2.6436	2.8781	3.1430	2.7033	2.7168	2.8282	2.8665	3.1067
GaAs	1.424	3.30	2.8579	3.2011	3.4736	2.9534	3.0041	3.1380	3.2382	3.3002
$CdGe(P_x\ As_{1-x})_2$	0.80	3.46	3.3011	3.5880	4.3390	3.3383	3.6180	3.8030	3.8452	3.5480
$CdGe(P_{0.2}\ As_{0.8})_2$										
$CdGe(P_{0.6}\ As_{0.4})_2$	1.26	3.32	2.9467	3.3028	3.6229	3.0442	3.1250	3.2686	3.3785	3.3636
$CdSeP_2$	1.72	3.16	2.7261	3.0176	3.2661	2.8047	2.8267	2.9465	3.0143	3.1888
GeTe	0.10	6.00	5.5518	4.0220	NA	3.9386	7.0737	7.6059	4.8193	3.8481
Te	0.335	5.30	4.1036	3.8763	NA	3.7115	4.7902	5.0832	4.4506	3.7446

Table A.1 continued from previous page

Material	$^\star E_g$ **(eV)**	**Refractive Index (n)**								
		***Exp.**	**Moss**	**Ravindra**	**Reddy**	**Herve**	**Kumar**	**Ahmad**	**Tripathy**	**Proposed Model**
As	1.20	3.35	2.9829	3.3400	3.6863	3.0791	3.1746	3.3222	3.4330	3.3871
Se	2.30	2.45	2.5351	2.6580	2.9877	2.5604	2.5739	2.6745	2.6668	2.9814
S	3.82	2.04	2.2331	1.7156	2.5846	2.1167	2.1855	2.2584	2.1373	2.4994
C	5.40	2.35	2.0480	0.7360	2.3524	1.8305	1.9547	2.0123	1.8981	2.0809
Csl	6.30	1.82	1.9706	0.1780	2.2576	1.7140	1.8599	1.9115	1.8296	1.8746
CsBr	7.50	1.67	1.8865	-0.5660	2.1561	1.5928	1.7582	1.8036	1.7774	1.6310
CsCI	8.00	1.61	1.8563	-0.8760	2.1199	1.5511	1.7220	1.7652	1.7639	1.5391
NaCI	8.60	1.540	1.8231	-1.2480	2.0801	1.5065	1.6823	1.7231	1.7517	1.4356
NaBr	7.70	1.641	1.8742	-0.6900	2.1412	1.5756	1.7434	1.7878	1.7715	1.5936
KCl	8.50	1.490	1.8284	-1.1860	2.0865	1.5136	1.6887	1.7299	1.7535	1.4523
KBr	7.80	1.559	1.8681	-0.7520	2.1340	1.5672	1.7361	1.7801	1.7688	1.5752
RbCI	8.20	1.493	1.8449	-1.0000	2.1062	1.5356	1.7083	1.7507	1.7594	1.5038
RbBr	7.70	1.553	1.8742	-0.6900	2.1412	1.5756	1.7434	1.7878	1.7715	1.5936
NiF_2	9.00	1.56	1.8025	-1.4960	2.0556	1.4797	1.6578	1.6972	1.7456	1.3705
P_2O_3	10.08	1.599	1.7521	-2.1656	1.9959	1.4168	1.5983	1.6343	1.7343	1.2091
B_2O_3	8.45	1.458	1.8311	-1.1550	2.0897	1.5171	1.6919	1.7333	1.7544	1.4608
SiO_2	9.24	1.544	1.7907	-1.6448	2.0416	1.4646	1.6438	1.6824	1.7425	1.3329
Al_2O_3	6.96	1.696	1.9221	-0.2312	2.1989	1.6432	1.8011	1.8490	1.7968	1.7364

Table A.1 continued from previous page

Material	$^{\star}E_g$ **(eV)**	**Refractive Index (n)**								
		*Exp.	**Moss**	**Ravindra**	**Reddy**	**Herve**	**Kumar**	**Ahmad**	**Tripathy**	**Proposed Model**
MgO	7.20	1.737	1.9059	-0.3800	2.1793	1.6201	1.7815	1.8283	1.7875	1.6887
CaO	6.26	1.837	1.9737	0.2028	2.2615	1.7186	1.8637	1.9155	1.8320	1.8833
SrO	6.50	1.870	1.9553	0.0540	2.2390	1.6914	1.8412	1.8917	1.8184	1.8316
BaO	5.20	1.980	2.0674	0.8600	2.3763	1.8603	1.9786	2.0377	1.9183	2.1297
MnO	4.00	2.160	2.2076	1.6040	2.5520	2.0772	2.1533	2.2240	2.0987	2.4478
FeO	3.20	2.320	2.3342	2.1000	2.7156	2.2710	2.3139	2.3957	2.3029	2.6858
ZnO	4.80	2.020	2.1092	1.1080	2.4282	1.9247	2.0303	2.0928	1.9661	2.2308
GeO_2	5.00	2.000	2.0878	0.9840	2.4016	1.8916	2.0038	2.0646	1.9409	2.1797
Sb_2O_3	3.36	2.305	2.3059	2.0008	2.6786	2.2282	2.2778	2.3571	2.2547	2.6364
HgO	2.58	2.516	2.4633	2.4844	2.8885	2.4603	2.4803	2.5740	2.5342	2.8861
Bi_2O_3	2.58	2.516	2.4633	2.4844	2.8885	2.4603	2.4803	2.5740	2.5342	2.8861
PbO	2.04	2.715	2.6123	2.8192	3.0975	2.6631	2.6754	2.7836	2.8093	3.0726
SnO_2	4.80	2.030	2.1092	1.1080	2.4282	1.9247	2.0303	2.0928	1.9661	2.2308
Ga_2O_3	5.40	1.941	2.0480	0.7360	2.3524	1.8305	1.9547	2.0123	1.8981	2.0809
CdO	2.72	2.471	2.4310	2.3976	2.8445	2.4140	2.4384	2.5291	2.4750	2.8396
Se_2O_3	5.00	2.00	2.0878	0.9840	2.4016	1.8916	2.0038	2.0646	1.9409	2.1797
CeO_2	3.36	2.305	2.3059	2.0008	2.6786	2.2282	2.2778	2.3571	2.2547	2.6364
TiO_2	2.04	2.715	2.6123	2.8192	3.0975	2.6631	2.6754	2.7836	2.8093	3.0726

Table A.1 continued from previous page

Material	${}^\star E_g$ **(eV)**	**Refractive Index (n)**								
		***Exp.**	**Moss**	**Ravindra**	**Reddy**	**Herve**	**Kumar**	**Ahmad**	**Tripathy**	**Proposed Model**
Cr_2O_3	2.58	2.516	2.4633	2.4844	2.8885	2.4603	2.4803	2.5740	2.5342	2.8861
Fe_2O_3	1.40	2.951	2.8701	3.2160	3.4936	2.9663	3.0207	3.1558	3.2580	3.3094
CoO	3.20	2.345	2.3342	2.1000	2.7156	2.2710	2.3139	2.3957	2.3029	2.6858
NiO	3.86	2.195	2.2273	1.6908	2.5772	2.1077	2.1781	2.2505	2.1284	2.4879
Cu_2O	2.04	2.715	2.6123	2.8192	3.0975	2.6631	2.6754	2.7836	2.8093	3.0726
MoO_3	2.74	2.471	2.4266	2.3852	2.8385	2.4075	2.4326	2.5229	2.4669	2.8330
Error			-1.7%	-31.4%	17.6%	6.8%	0.6%	4.8%	1.1%	3.3%
MSE			0.0129	0.3551	0.0363	0.0147	0.0099	0.0132	0.0112	0.0225
χ^2			0.0057	0.2542	0.0219	0.0042	0.0039	0.0053	0.0045	0.0085

$\star$ taken from [54]

Bibliography

[1] N. Galov, “What Percentage of Internet Traffic Is Mobile in 2019?”, *Hosting Tribunal*, 2019. [Online]. Available: `https://hostingtribunal.com/blog/mobile-percentage-of-traffic/#gref`.

[2] C. V. N. Index, “Cisco visual networking index: Global mobile data traffic forecast update, 2015-2020 white paper”, *Accessed date*, 2016.

[3] B. Saleh and M. Teich, *Fundamentals of Photonics*. Wiley, 1991.

[4] E. Sauter, *Nonlinear optics*. John Wiley & Sons, 1996, vol. 44.

[5] G. Boyd and D. Kleinman, “Parametric interaction of focused gaussian light beams”, *Journal of Applied Physics*, vol. 39, no. 8, pp. 3597–3639, 1968.

[6] L. Yan, A. E. Willner, X. Wu, A. Yi, A. Bogoni, Z.-Y. Chen, and H.-Y. Jiang, “All-optical signal processing for ultrahigh speed optical systems and networks”, *Journal of Lightwave Technology*, vol. 30, no. 24, pp. 3760–3770, 2012.

[7] M. Bajcsy, S. Hofferberth, V. Balic, T. Peyronel, M. Hafezi, A. S. Zibrov, V. Vuletic, and M. D. Lukin, “Efficient all-optical switching using slow light within a hollow fiber”, *Physical review letters*, vol. 102, no. 20, p. 203 902, 2009.

[8] A. Bogoni, X. Wu, I. Fazal, and A. E. Willner, “160 gb/s time-domain channel extraction/insertion and all-optical logic operations exploiting a single ppln waveguide”, *Journal of Lightwave Technology*, vol. 27, no. 19, pp. 4221–4227, 2009.

[9] R. Salem, M. A. Foster, A. C. Turner, D. F. Geraghty, M. Lipson, and A. L. Gaeta, “Signal regeneration using low-power four-wave mixing on silicon chip”, *Nature photonics*, vol. 2, no. 1, p. 35, 2008.

[10] V. G. Ta’eed, M. Shokooh-Saremi, L. Fu, I. C. Littler, D. J. Moss, M. Rochette, B. J. Eggleton, Y. Ruan, and B. Luther-Davies, “Self-phase modulation-based integrated optical regeneration in chalcogenide waveguides”, *IEEE Journal of Selected Topics in Quantum Electronics*, vol. 12, no. 3, pp. 360–370, 2006.

[11] K. Dolgaleva, W. C. Ng, L. Qian, and J. S. Aitchison, "Compact highly-nonlinear algaas waveguides for efficient wavelength conversion", *Optics express*, vol. 19, no. 13, pp. 12 440–12 455, 2011.

[12] R. Salem, M. A. Foster, A. C. Turner, D. F. Geraghty, M. Lipson, and A. L. Gaeta, "Signal regeneration using low-power four-wave mixing on silicon chip", *Nature photonics*, vol. 2, no. 1, p. 35, 2008.

[13] S. F. Preble, Q. Xu, B. S. Schmidt, and M. Lipson, "Ultrafast all-optical modulation on a silicon chip", *Optics letters*, vol. 30, no. 21, pp. 2891–2893, 2005.

[14] G. Lifante, *Integrated photonics: fundamentals*. John Wiley & Sons, 2003.

[15] S. Bogdanov, M. Shalaginov, A. Boltasseva, and V. M. Shalaev, "Material platforms for integrated quantum photonics", *Optical Materials Express*, vol. 7, no. 1, pp. 111–132, 2017.

[16] G. Stegeman, A Villeneuve, J Kang, J. Aitchison, C. Ironside, K Al-Hemyari, C. Yang, C.-H. Lin, H.-H. Lin, G. Kennedy, *et al.*, "Algaas below half bandgap: The silicon of nonlinear optical materials", *International Journal of Nonlinear Optical Physics*, vol. 3, no. 03, pp. 347–371, 1994.

[17] G. A. Siviloglou, S. Suntsov, R. El-Ganainy, R. Iwanow, G. I. Stegeman, D. N. Christodoulides, R. Morandotti, D. Modotto, A. Locatelli, C. De Angelis, *et al.*, "Enhanced third-order nonlinear effects in optical algaas nanowires", *Optics Express*, vol. 14, no. 20, pp. 9377–9384, 2006.

[18] A. R. Denton and N. W. Ashcroft, "Vegard's law", *Physical review A*, vol. 43, no. 6, p. 3161, 1991.

[19] H. Ibach and H. Lüth, *Solid-State Physics: An Introduction to Theory and Experiment*. Springer-Verlag, 1995.

[20] G. Stegeman, E. Wright, N Finlayson, R Zanoni, and C. Seaton, "Third order nonlinear integrated optics", *Journal of lightwave technology*, vol. 6, no. 6, pp. 953–970, 1988.

[21] A Gaggero, S. J. Nejad, F Marsili, F Mattioli, R Leoni, D Bitauld, D Sahin, G. Hamhuis, R Nötzel, R Sanjines, *et al.*, "Nanowire superconducting single-photon detectors on gaas for integrated quantum photonic applications", *Applied Physics Letters*, vol. 97, no. 15, p. 151 108, 2010.

[22] J. S. Aitchison, D. C. Hutchings, J. U. Kang, G. I. Stegeman, and A. Villeneuve, "The nonlinear optical properties of AlGaAs at the half

band gap", *IEEE J. Quantum Electron.*, vol. 33, no. 3, pp. 341–348, 1997, ISSN: 0018-9197. DOI: 10.1109/3.556002.

[23] P. Apiratikul, J. J. Wathen, G. A. Porkolab, B. Wang, L. He, T. E. Murphy, and C. J. K. Richardson, "Enhanced continuous-wave four-wave mixing efficiency in nonlinear AlGaAs waveguides", *Opt. Express*, vol. 22, no. 22, pp. 26 814–26 824, 2014, ISSN: 1094-4087. DOI: 10.1364/OE.22.026814.

[24] L. Ottaviano, M. Pu, E. Semenova, and K. Yvind, "Low-loss high-confinement waveguides and microring resonators in AlGaAs-on-insulator", *Opt. Lett.*, vol. 41, no. 17, pp. 3996–3999, 2016, ISSN: 1539-4794. DOI: 10.1364/OL.41.003996.

[25] S Gehrsitz, F. Reinhart, C Gourgon, N Herres, A Vonlanthen, and H Sigg, "The refractive index of al x ga 1- x as below the band gap: Accurate determination and empirical modeling", *Journal of Applied Physics*, vol. 87, no. 11, pp. 7825–7837, 2000.

[26] S. Kasap and P. Capper, *Springer handbook of electronic and photonic materials*. Springer, 2017.

[27] J. Ihm and J. D. Joannopoulos, "Ground-state properties of GaAs and AlAs", *Phys. Rev. B*, vol. 24, no. 8, pp. 4191–4197, 1981, ISSN: 2469-9969. DOI: 10.1103/PhysRevB.24.4191.

[28] K. Awan, "Fabrication of iii-v integrated photonic devices", PhD thesis, Université d'Ottawa/University of Ottawa, 2018.

[29] K. Dolgaleva, P. Sarrafi, P. Kultavewuti, K. M. Awan, N. Feher, J. S. Aitchison, L. Qian, M. Volatier, R. Arès, and V. Aimez, "Tuneable four-wave mixing in algaas nanowires", *Optics express*, vol. 23, no. 17, pp. 22 477–22 493, 2015.

[30] M Anani, C Mathieu, S Lebid, Y Amar, Z Chama, and H Abid, "Model for calculating the refractive index of a iii–v semiconductor", *Computational Materials Science*, vol. 41, no. 4, pp. 570–575, 2008.

[31] T. S. Moss, "Relations between the Refractive Index and Energy Gap of Semiconductors", *Phys. Status solidi B*, vol. 131, no. 2, pp. 415–427, 1985, ISSN: 0370-1972. DOI: 10.1002/pssb.2221310202.

[32] V Kumar and J. Singh, "Model for calculating the refractive index of different materials", 2010.

[33] S. Ahmad, M. M.-u. Haq, *et al.*, "A study of energy gap, refractive index and electronic polarizability of ternary chalcopyrite semiconductors", *Iranian Journal of Physics Research*, vol. 14, no. 3, pp. 89–93, 2014.

[34] W. Wolfe, J. Jenney, W. Levengood, T Limperis, and D. Szeles, “Optical constants of germanium”, MICHIGAN UNIV ANN ARBOR INST OF SCIENCE and TECHNOLOGY, Tech. Rep., 1964.

[35] D. G. Avery, “An improved method for measurements of optical constants by reflection”, *Proceedings of the Physical Society. Section B*, vol. 65, no. 6, pp. 425–428, 1952. DOI: 10.1088/0370-1301/65/6/305. [Online]. Available: https://doi.org/10.1088%2F0370-1301%2F65%2F6%2F305.

[36] D. Aspnes, “Local-field effects and effective-medium theory: A microscopic perspective”, *American Journal of Physics*, vol. 50, no. 8, pp. 704–709, 1982.

[37] H. A. Lorentz, *The Theory of Electrons and Its Applications to the Phenomena of Light and Radiant Heart: A Course of Lectures Delivered in Columbia University, New York in March and April, 1906*. Teubner, 1916, vol. 29.

[38] P. J. W. Debye, *Polar molecules*. Chemical Catalog Company, Incorporated, 1929.

[39] O. L. Anderson and E. Schreiber, “The relation between refractive index and density of minerals related to the Earth’s mantle”, *J. Geophys. Res.*, vol. 70, no. 6, pp. 1463–1471, 1965, ISSN: 0148-0227. DOI: 10.1029/JZ070i006p01463.

[40] [Online; accessed 20. May 2019], 2014. [Online]. Available: http://www.horiba.com/fileadmin/uploads/Scientific/Downloads/OpticalSchool_CN/TN/ellipsometer/Cauchy_and_related_empirical_dispersion_Formulae_for_Transparent_Materials.pdf.

[41] Sellmeier, “Zur Erklärung der abnormen Farbenfolge im Spectrum einiger Substanzen”, *Ann. Phys.*, vol. 219, no. 6, pp. 272–282, 1871, ISSN: 0003-3804. DOI: 10.1002/andp.18712190612.

[42] J. A. Duffy, “Trends in energy gaps of binary compounds: an approach based upon electron transfer parameters from optical spectroscopy”, *J. Phys. C: Solid State Phys.*, vol. 13, no. 16, pp. 2979–2989, 1980, ISSN: 0022-3719. DOI: 10.1088/0022-3719/13/16/008.

[43] T. S. Moss, “A Relationship between the Refractive Index and the Infra-Red Threshold of Sensitivity for Photoconductors”, *Proc. Phys. Soc. London, Sect. B*, vol. 63, no. 3, pp. 167–176, 1950, ISSN: 0370-1301. DOI: 10.1088/0370-1301/63/3/302.

[44] ——, “Photoconductivity in the Elements”, *Proc. Phys. Soc. London, Sect. A*, vol. 64, no. 6, pp. 590–591, 1951, ISSN: 0370-1298. DOI: 10.1088/0370-1298/64/6/113.

[45] N. M. Ravindra, S. Auluck, and V. K. Srivastava, "On the Penn Gap in Semiconductors", *Phys. Status solidi B*, vol. 93, no. 2, K155–K160, 1979, ISSN: 0370-1972. DOI: `10.1002/pssb.2220930257`.

[46] V. P. Gupta and N. M. Ravindra, "Comments on the Moss Formula", *Phys. Status solidi B*, vol. 100, no. 2, pp. 715–719, 1980, ISSN: 0370-1972. DOI: `10.1002/pssb.2221000240`.

[47] D. R. Penn, "Wave-Number-Dependent Dielectric Function of Semiconductors", *Phys. Rev.*, vol. 128, no. 5, pp. 2093–2097, 1962, ISSN: 1536-6065. DOI: `10.1103/PhysRev.128.2093`.

[48] P. Hervé and L. K. J. Vandamme, "General relation between refractive index and energy gap in semiconductors", *Infrared Physics & Technology*, vol. 35, no. 4, pp. 609–615, 1994, ISSN: 1350-4495. DOI: `10.1016/1350-4495(94)90026-4`.

[49] R. Reddy, Y. N. Aharnmed, P. A. Azeem, K. R. Gopal, B. S. Devi, and T. Rao, "Dependence of physical parameters of compound semiconductors on refractive index", *Defence Science Journal*, vol. 53, no. 3, pp. 239–248, 2003.

[50] R. Reddy, K. R. Gopal, K Narasimhulu, L. S. S. Reddy, K. R. Kumar, C. K. Reddy, and S. N. Ahmed, "Correlation between optical electronegativity and refractive index of ternary chalcopyrites, semiconductors, insulators, oxides and alkali halides", *Optical Materials*, vol. 31, no. 2, pp. 209–212, 2008.

[51] R. Reddy, K. R. Gopal, K Narasimhulu, L. S. S. Reddy, K. R. Kumar, G Balakrishnaiah, and M. R. Kumar, "Interrelationship between structural, optical, electronic and elastic properties of materials", *Journal of Alloys and Compounds*, vol. 473, no. 1-2, pp. 28–35, 2009.

[52] S. K. Tripathy, "Refractive indices of semiconductors from energy gaps", *Opt. Mater.*, vol. 46, pp. 240–246, 2015, ISSN: 0925-3467. DOI: `10.1016/j.optmat.2015.04.026`.

[53] M. J. Weber, *Handbook of Optical Materials*. Taylor & Francis, 2018, ISBN: 978-131521961-5. DOI: `10.1201/9781315219615`.

[54] R. R. Reddy, Y. Nazeer Ahammed, K. Rama Gopal, and D. V. Raghuram, "Optical electronegativity and refractive index of materials", *Opt. Mater.*, vol. 10, no. 2, pp. 95–100, 1998, ISSN: 0925-3467. DOI: `10.1016/S0925-3467(97)00171-7`.

[55] R. R. Reddy and Y. Nazeer Ahammed, "A study on the Moss relation", *Infrared Physics & Technology*, vol. 36, no. 5, pp. 825–830, 1995, ISSN: 1350-4495. DOI: `10.1016/1350-4495(95)00008-M`.

[56] S. Adachi, "Optical properties of $\mathrm{In}_{1-x}\mathrm{Ga}_x\mathrm{As}_y\mathrm{P}_{1-y} alloys$", *Phys. Rev. B*, vol. 39, no. 17, pp. 12 612–12 621, 1989, ISSN: 2469-9969. DOI: `10.1103/PhysRevB.39.12612`.

[57] S. Saeidi, K. M. Awan, L. Sirbu, and K. Dolgaleva, "Nonlinear photonics on-a-chip in III-V semiconductors: quest for promising material candidates", *Appl. Opt.*, vol. 56, no. 19, pp. 5532–5541, 2017, ISSN: 2155-3165. DOI: `10.1364/AO.56.005532`.

[58] N. An, L. Ma, G. Wen, Z. Liang, H. Zhang, T. Gao, and C. Fan, "Structure Design and Analysis of 2 μm InGaAsSb / AlGaAsSb Muti-Quantum Well Laser Diode with Carrier Blocking Layer", *Appl. Sci.*, vol. 9, no. 1, p. 162, 2019, ISSN: 2076-3417. DOI: `10.3390/app9010162`.

[59] T. Mozume, T. Simoyama, and H. Ishikawa, "Indices of refraction of AlGaAsSb by an optical waveguide technique", *J. Appl. Phys.*, vol. 102, no. 11, p. 113 111, 2007, ISSN: 0021-8979. DOI: `10.1063/1.2818101`.

[60] J. L. A.W. Snyder, *Optical Waveguide Theory (Science Paperbacks, 190)*, 1st ed. Springer, 1983, ISBN: 0412099500,9780412099502. [Online]. Available: `http://gen.lib.rus.ec/book/index.php?md5=4B486957AE16383F06D69F6D0A640B5`

[61] W. D. Callister, D. G. Rethwisch, *et al.*, *Materials science and engineering: an introduction*. John Wiley & Sons New York, 2007, vol. 7.

[62] K. Seshan, *Handbook of Thin Film Deposition Techniques Principles, Methods, Equipment and Applications, Second Edition*. CRC Press, 2002. [Online]. Available: `https://www.crcpress.com/Handbook-of-Thin-Film-Deposition-Techniques-Principles-Methods-Equipment/Seshan/p/book/9780815514428`.

[63] R. Pelzel, "A comparison of movpe and mbe growth technologies for iii-v epitaxial structures", in *CS MANTECH Conference*, Citeseer, 2013, pp. 105–108.

[64] D. A. Ahmari, G. Raghavan, Q. J. Hartmann, M. L. Hattendorf, M. Feng, and G. E. Stillman, "Temperature dependence of InGaP / GaAs heterojunction bipolar transistor DC and small-signal behavior", *IEEE Trans. Electron Devices*, vol. 46, no. 4, pp. 634–640, 1999, ISSN: 0018-9383. DOI: `10.1109/16.753694`.

[65] Z. L. Liau, S. C. Palmateer, S. H. Groves, J. N. Walpole, and L. J. Missaggia, "Low-threshold InGaAs strained-layer quantum-well lasers (λ=0.98 μm) with GaInP cladding layers and mass-transported buried heterostructure", *Appl. Phys. Lett.*, vol. 60, no. 1, pp. 6–8, 1992, ISSN: 0003-6951. DOI: `10.1063/1.107377`.

[66] K. A. Bertness, S. R. Kurtz, D. J. Friedman, A. E. Kibbler, C. Kramer, and J. M. Olson, "29.5%-efficient GaInP/GaAs tandem solar cells", *Appl. Phys. Lett.*, vol. 65, no. 8, pp. 989–991, 1994, ISSN: 0003-6951. DOI: `10.1063/1.112171`.

[67] Y. G. Hong, A. Nishikawa, and C. W. Tu, "Effect of nitrogen on the optical and transport properties of Ga0.48In0.52NyP1-y grown on GaAs(001) substrates", *Appl. Phys. Lett.*, vol. 83, no. 26, pp. 5446–5448, 2003, ISSN: 0003-6951. DOI: `10.1063/1.1637148`.

[68] M. G. Craford, "Visible LEDs: the trend toward high-power emitters and remaining challenges for solid state lighting", *Solid State Lighting II*, vol. 4776, pp. 1–8, 2002. DOI: `10.1117/12.457111`.

[69] Y. K. Su, C. H. Wu, Y. S. Huang, H. P. Hsu, W. C. Chen, S. H. Hsu, and S. J. Chang, "Piezoreflectance and contactless electroreflectance spectra of an optoelectronic material: GaInNP grown on GaAs substrates", *J. Cryst. Growth*, vol. 264, no. 1, pp. 357–362, 2004, ISSN: 0022-0248. DOI: `10.1016/j.jcrysgro.2004.01.024`.

[70] V. A. Odnoblyudov and C. W. Tu, "Gas-source molecular-beam epitaxial growth of Ga(In)NP on GaP(100) substrates for yellow-amber light-emitting devices", *Journal of Vacuum Science & Technology B: Microelectronics and Nanometer Structures Processing, Measurement, and Phenomena*, vol. 23, no. 3, p. 1317, 2005, ISSN: 1071-1023. DOI: `10.1116/1.1878996`.

[71] T. Imanishi, A. Wakahara, S. M. Kim, H. Yonezu, and Y. Furukawa, "Optical properties of lattice matched InxGa1–xP1–yNy heteroepitaxial layers on GaP", *Phys. Status solidi A*, vol. 202, no. 5, pp. 854–858, 2005, ISSN: 1862-6300. DOI: `10.1002/pssa.200461434`.

[72] Y. Furukawa, H. Yonezu, K. Ojima, K. Samonji, Y. Fujimoto, K. Momose, and K. Aiki, "Control of N Content of GaPN Grown by Molecular Beam Epitaxy and Growth of GaPN Lattice Matched to Si(100) Substrate", *Jpn. J. Appl. Phys.*, vol. 41, no. Part 1, No. 2A, pp. 528–532, 2002, ISSN: 0021-4922. DOI: `10.1143/jjap.41.528`.

[73] J. S. Yuan, C. C. Hsu, R. M. Cohen, and G. B. Stringfellow, "Organometallic vapor phase epitaxial growth of AlGaInP", *J. Appl. Phys.*, vol. 57, no. 4, pp. 1380–1383, 1985, ISSN: 0021-8979. DOI: `10.1063/1.334491`.

[74] H. Asahi, Y. Kawamura, and H. Nagai, "Molecular beam epitaxial growth of InGaAlP on (100) GaAs", *J. Appl. Phys.*, vol. 53, no. 7, pp. 4928–4931, 1982, ISSN: 0021-8979. DOI: `10.1063/1.331326`.

[75] G. Stringfellow, "Vpe growth of iii/v semiconductors", *Annual Review of Materials Science*, vol. 8, no. 1, pp. 73–98, 1978.

[76] J. S. Cheong, A. N. A. P. Baharuddin, J. S. Ng, A. B. Krysa, and J. P. R. David, "Absorption coefficients in AlGaInP lattice-matched to GaAs", *Sol. Energy Mater. Sol. Cells*, vol. 164, pp. 28–31, 2017, ISSN: 0927-0248. DOI: `10.1016/j.solmat.2017.01.042`.

[77] E. Kapon and P. S. Zory, "Quantum well lasers", *Academic, London*, 1993.

[78] R. P. Schneider and J. A. Lott, "Cavity design for improved electrical injection in InAlGaP/AlGaAs visible (639–661 nm) vertical-cavity surface-emitting laser diodes", *Appl. Phys. Lett.*, vol. 63, no. 7, pp. 917–919, 1993, ISSN: 0003-6951. DOI: `10.1063/1.109844`.

[79] S. P. Najda, A. H. Kean, M. D. Dawson, and G. Duggan, "Optical measurements of electronic bandstructure in AlGaInP alloys grown by gas source molecular beam epitaxy", *J. Appl. Phys.*, vol. 77, no. 7, pp. 3412–3415, 1995, ISSN: 0021-8979. DOI: `10.1063/1.358631`.

[80] J. P. André, E. Dupont-Nivet, D. Moroni, J. N. Patillon, M. Erman, and T. Ngo, "GaInP-AlGaInP-GaAs heterostructures grown by MOVPE at atmospheric pressure", *J. Cryst. Growth*, vol. 77, no. 1, pp. 354–359, 1986, ISSN: 0022-0248. DOI: `10.1016/0022-0248(86)90323-4`.

[81] D. S. Cao, A. W. Kimball, and G. B. Stringfellow, "Atmospheric pressure organometallic vapor-phase epitaxial growth of (AlxGa1-x)0.51In0.49P (x from 0 to 1) using trimethylalkyls", *J. Appl. Phys.*, vol. 67, no. 2, pp. 739–744, 1990, ISSN: 0021-8979. DOI: `10.1063/1.346101`.

[82] D. J. Mowbray, O. P. Kowalski, M. Hopkinson, M. S. Skolnick, and J. P. R. David, "Electronic band structure of AlGaInP grown by solid-source molecular-beam epitaxy", *Appl. Phys. Lett.*, vol. 65, no. 2, pp. 213–215, 1994, ISSN: 0003-6951. DOI: `10.1063/1.112676`.

[83] M. O. Watanabe and Y. Ohba, "Interface properties for GaAs/InGaAlP heterojunctions by the capacitance-voltage profiling technique", *Appl. Phys. Lett.*, vol. 50, no. 14, pp. 906–908, 1987, ISSN: 0003-6951. DOI: `10.1063/1.98028`.

[84] A. T. M. D. J. D. E. P. O. A. D. Prins J. L. Sly and A. R. Adams, "Defects in Semiconductors", *Int. Conf. in Physics of Semiconductors*, vol. 22, 1994, ISSN: 978-981-4550-15-4. DOI: `10.1142/2532`.

[85] S. Adachi, S. Ozaki, M. Sato, and K. Ohtsuka, "Electroreflectance Study of (AlxGa1-x)0.5In0.5P Alloys", *Jpn. J. Appl. Phys.*, vol. 35, no. Part 1,

No. 2A, pp. 537–542, 1996, ISSN: 0021-4922. DOI: 10.1143/jjap.35.537.

[86] K. Asami, H. Asahi, S.-i. Gonda, Y. Kawamura, and H. Tanaka, "Electroreflectance study of AlxGa1-x-yInyP alloy", *Solid State Commun.*, vol. 70, no. 1, pp. 33–35, 1989, ISSN: 0038-1098. DOI: 10.1016/0038-1098(89)90462-6.

[87] T. Hofmann, G. Leibiger, V. Gottschalch, I. Pietzonka, and M. Schubert, "Infrared dielectric function and phonon modes of highly disordered $(\mathrm{Al}_x\mathrm{Ga}_{1-x})_{0.52}\mathrm{In}_{0.48}\mathrm{P}$", *Phys. Rev. B*, vol. 64, no. 15, p. 155 206, 2001, ISSN: 2469-9969. DOI: 10.1103/PhysRevB.64.155206.

[88] S. Adachi, H. Kato, A. Moki, and K. Ohtsuka, "Refractive index of (AlxGa1-x)0.5In0.5P quaternary alloys", *J. Appl. Phys.*, vol. 75, no. 1, pp. 478–480, 1994, ISSN: 0021-8979. DOI: 10.1063/1.355824.

[89] J. S. Cheong, J. S. Ng, A. B. Krysa, J. S. L. Ong, and J. P. R. David, "Determination of absorption coefficients in AlInP lattice matched to GaAs", *J. Phys. D: Appl. Phys.*, vol. 48, no. 40, p. 405 101, 2015, ISSN: 0022-3727. DOI: 10.1088/0022-3727/48/40/405101.

[90] M. Toivonen, A. Salokatve, K. Tappura, M. Jalonen, P. Savolainen, J. Nappi, M. Pessa, and H. Asonen, *Solid source MBE for phosphide-based devices*. IEEE, 1996, ISBN: 978-0-7803-3283-6. DOI: 10.1109/ICIPRM.1996.491939.

[91] H. G. Grimmeiss, W. Kischio, and A. Rabenau, "Über das AlP: Darstellung, elektrische und optische eigenschaften", *J. Phys. Chem. Solids*, vol. 16, no. 3, pp. 302–309, 1960, ISSN: 0022-3697. DOI: 10.1016/0022-3697(60)90160-8.

[92] M. Kneissl, T. Kolbe, C. Chua, V. Kueller, N. Lobo, J. Stellmach, A. Knauer, H. Rodriguez, S. Einfeldt, Z. Yang, N. M. Johnson, and M. Weyers, "Advances in group III-nitride-based deep UV light-emitting diode technology", *Semicond. Sci. Technol.*, vol. 26, no. 1, p. 014 036, 2010, ISSN: 0268-1242. DOI: 10.1088/0268-1242/26/1/014036.

[93] X. Hu, J. Deng, J. P. Zhang, A. Lunev, Y. Bilenko, T. Katona, M. S. Shur, R. Gaska, M. Shatalov, and A. Khan, "Deep ultraviolet light-emitting diodes", *Phys. Status solidi A*, vol. 203, no. 7, pp. 1815–1818, 2006, ISSN: 1862-6300. DOI: 10.1002/pssa.200565266.

[94] S.-C. Shei, J.-K. Sheu, C.-M. Tsai, W.-C. Lai, M.-L. Lee, and C.-H. Kuo, "Emission Mechanism of Mixed-Color InGaN/GaN Multi-Quantum-Well Light-Emitting Diodes", *Jpn. J. Appl. Phys.*, vol. 45, no. 4A, pp. 2463–2466, 2006, ISSN: 0021-4922. DOI: 10.1143/jjap.45.2463.

[95] S. Sakr, P. Crozat, D. Gacemi, Y. Kotsar, A. Pesach, P. Quach, N. Isac, M. Tchernycheva, L. Vivien, G. Bahir, E. Monroy, and F. H. Julien, “GaN/AlGaN waveguide quantum cascade photodetectors at $\lambda \approx 1.55$ μm with enhanced responsivity and ∼40 GHz frequency bandwidth”, *Appl. Phys. Lett.*, vol. 102, no. 1, p. 011 135, 2013, ISSN: 0003-6951. DOI: `10.1063/1.4775374`.

[96] S. N. Mohammad and H. Morkoç, “Progress and prospects of group-III nitride semiconductors”, *Prog. Quantum Electron.*, vol. 20, no. 5, pp. 361–525, 1996, ISSN: 0079-6727. DOI: `10.1016/S0079-6727(96)00002-X`.

[97] T. Suzuki, H. Yaguchi, H. Okumura, Y. Ishida, and S. Yoshida, “Optical Constants of Cubic GaN, AlN, and AlGaN Alloys”, *Jpn. J. Appl. Phys.*, vol. 39, no. Part 2, No. 6A, pp. L497–L499, 2000, ISSN: 0021-4922. DOI: `10.1143/jjap.39.l497`.

[98] A. Pierret, C. Bougerol, S. Murcia-Mascaros, A. Cros, H. Renevier, B. Gayral, and B. Daudin, “Growth, structural and optical properties of AlGaN nanowires in the whole composition range”, *Nanotechnology*, vol. 24, no. 11, p. 115 704, 2013, ISSN: 0957-4484. DOI: `10.1088/0957-4484/24/11/115704`.

[99] T. Takeuchi, H. Takeuchi, S. Sota, H. Sakai, H. Amano, and I. Akasaki, “Optical Properties of Strained AlGaN and GaInN on GaN”, *Jpn. J. Appl. Phys.*, vol. 36, no. Part 2, No. 2B, pp. L177–L179, 1997, ISSN: 0021-4922. DOI: `10.1143/jjap.36.l177`.

[100] D. Brunner, H. Angerer, E. Bustarret, F. Freudenberg, R. Höpler, R. Dimitrov, O. Ambacher, and M. Stutzmann, “Optical constants of epitaxial AlGaN films and their temperature dependence”, *J. Appl. Phys.*, vol. 82, no. 10, pp. 5090–5096, 1997, ISSN: 0021-8979. DOI: `10.1063/1.366309`.

[101] J. P. Zhang, M. A. Khan, W. H. Sun, H. M. Wang, C. Q. Chen, Q. Fareed, E. Kuokstis, and J. W. Yang, “Pulsed atomic-layer epitaxy of ultrahigh-quality AlxGa1-xN structures for deep ultraviolet emissions below 230 nm”, *Appl. Phys. Lett.*, vol. 81, no. 23, pp. 4392–4394, 2002, ISSN: 0003-6951. DOI: `10.1063/1.1528726`.

[102] P. Sohi, D. Martin, and N. Grandjean, “Critical thickness of GaN on AlN: impact of growth temperature and dislocation density”, *Semicond. Sci. Technol.*, vol. 32, no. 7, p. 075 010, 2017, ISSN: 0268-1242. DOI: `10.1088/1361-6641/aa7248`.

[103] J. F. Muth, J. D. Brown, M. A. L. Johnson, Z. Yu, R. M. Kolbas, J. W. Cook, and J. F. Schetzina, "Absorption Coefficient and Refractive Index of GaN, AIN and AlGaN Alloys", *MRS Online Proceedings Library Archive*, vol. 537, 1998, ISSN: 0272-9172. DOI: `10.1557/PROC-537-G5.2`.

[104] M. A. Khan, J. N. Kuznia, J. M. Van Hove, N. Pan, and J. Carter, "Observation of a two-dimensional electron gas in low pressure metalorganic chemical vapor deposited GaN-AlxGa1-xN heterojunctions", *Appl. Phys. Lett.*, vol. 60, no. 24, pp. 3027–3029, 1992, ISSN: 0003-6951. DOI: `10.1063/1.106798`.

[105] R. Hui, S. Taherion, Y. Wan, J. Li, S. X. Jin, J. Y. Lin, and H. X. Jiang, "GaN-based waveguide devices for long-wavelength optical communications", *Appl. Phys. Lett.*, vol. 82, no. 9, pp. 1326–1328, 2003, ISSN: 0003-6951. DOI: `10.1063/1.1557790`.

[106] K. Takeuchi, S. Adachi, and K. Ohtsuka, "Optical properties of AlxGa1-xN alloy", *J. Appl. Phys.*, vol. 107, no. 2, p. 023 306, 2010, ISSN: 0021-8979. DOI: `10.1063/1.3284956`.

[107] P. Wisniewski, W. Knap, J. P. Malzac, J. Camassel, M. D. Bremser, R. F. Davis, and T. Suski, "Investigation of optically active E1 transversal optic phonon modes in AlxGa1-xN layers deposited on 6H–SiC substrates using infrared reflectance", *Appl. Phys. Lett.*, vol. 73, no. 13, pp. 1760–1762, 1998, ISSN: 0003-6951. DOI: `10.1063/1.122273`.

[108] Z. G. Hu, M. B. M. Rinzan, S. G. Matsik, A. G. U. Perera, G. Von Winckel, A. Stintz, and S. Krishna, "Optical characterizations of heavily doped p-type AlxGa1-xAs and GaAs epitaxial films at terahertz frequencies", *J. Appl. Phys.*, vol. 97, no. 9, p. 093 529, 2005, ISSN: 0021-8979. DOI: `10.1063/1.1894581`.

[109] A. Liu, S.-L. Chuang, and C. Z. Ning, "Piezoelectric field-enhanced second-order nonlinear optical susceptibilities in wurtzite GaN/AlGaN quantum wells", *Appl. Phys. Lett.*, vol. 76, no. 3, pp. 333–335, 2000, ISSN: 0003-6951. DOI: `10.1063/1.125736`.

[110] S. Keller, G. Parish, P. T. Fini, S. Heikman, C.-H. Chen, N. Zhang, S. P. DenBaars, U. K. Mishra, and Y.-F. Wu, "Metalorganic chemical vapor deposition of high mobility AlGaN/GaN heterostructures", *J. Appl. Phys.*, vol. 86, no. 10, pp. 5850–5857, 1999, ISSN: 0021-8979. DOI: `10.1063/1.371602`.

[111] T. Oder, J. Lin, and H. Jiang, "Fabrication and optical characterization of iii-nitride sub-micron waveguides", *Appl. Phys. Lett*, vol. 79, pp. 12–14, 2001.

[112] J. P. Zhang, H. M. Wang, M. E. Gaevski, C. Q. Chen, Q. Fareed, J. W. Yang, G. Simin, and M. A. Khan, "Crack-free thick AlGaN grown on sapphire using AlN/AlGaN superlattices for strain management", *Appl. Phys. Lett.*, vol. 80, no. 19, pp. 3542–3544, 2002, ISSN: 0003-6951. DOI: `10.1063/1.1477620`.

[113] M. Schubert, V. Gottschalch, C. M. Herzinger, H. Yao, P. G. Snyder, and J. A. Woollam, "Optical constants of GaxIn1-xP lattice matched to GaAs", *J. Appl. Phys.*, vol. 77, no. 7, pp. 3416–3419, 1995, ISSN: 0021-8979. DOI: `10.1063/1.358632`.